

# POLITECNICO DI TORINO

Master's Degree in Physics of Complex Systems



**Politecnico  
di Torino**

Master's Degree Thesis

## Tuning and characterizing the superconducting phases of iron selenide telluride thin films induced via gate-driven hydrogen intercalation

Supervisors

Prof. Renato GONNELLI

Prof. Dario DAGHERO

Dr. Erik PIATTI

Candidate

Christian TOMASELLI

Academic year 2024/2025

## Abstract

The discovery of iron-based superconductors marks an important turning point in solid-state physics. The superconducting transition temperature ( $T_C$ ) of these compounds is among the highest known.  $FeSe$  is one of the simplest ones but nevertheless presents a rich phase diagram. Although stoichiometric  $FeSe$  is not superconducting, it can display superconductivity under pressure, strain, partial substitution of Se with isovalent elements like  $Te$  or aliovalent elements like  $S$ , and even under electron doping. In the latter case, it develops high- $T_C$  phases whose nature remains a subject of intense debate. My thesis work is positioned within this debate. It focuses on the study of thin films of  $FeSe_{0.5}Te_{0.5}$ , with a  $T_C = 16$  K, before and after electron doping (obtained through hydrogen intercalation).

Indeed,  $FeSe$  and  $Fe(Se, Te)$  are layered compounds that can be intercalated rather easily. Here, I used the so-called ionic liquid-gating technique to insert  $H^+$  ions in the lattice. The idea is to immerse the  $Fe(Se, Te)$  film and a metallic gate, in a suitable ionic liquid that acts as an electrolyte. When a bias  $V_G$  is applied, the ionic liquid releases  $H^+$  ions pushing them into the film by the strong electric field at the surface. This insertion allows changing the electronic properties of the material and tuning the superconducting phase, i.e. increasing  $T_C$ . The work starts by a characterization of the pristine  $FeSe_{0.5}Te_{0.5}$  thin films by means of electric transport measurements as a function of temperature, to study the normal-state resistivity and determine their  $T_C$ . The superconducting phase is further studied by point-contact Andreev-reflection spectroscopy (PCARS), which allows gathering direct information on the number, amplitude and symmetry of the superconducting energy gap(s) by analyzing the differential conductance  $dI/dV$  of a small contact between a normal metal (N) and the superconductor (S) as a function of the bias voltage  $V$ . The  $dI/dV$  vs  $V$  spectra contain information of the superconducting gap  $\Delta$  thanks to a quantum phenomenon called Andreev reflection: an electron injected from N into S with an energy smaller than  $\Delta$  is reflected as a hole, while a Cooper pair is created in S. By analyzing the PCARS spectra obtained in  $FeSeTe$  pristine films, I identify structures that can be associated with the superconducting gap.

A fitting of the spectra with a suitable model in literature gives  $\Delta \simeq 2.4k_B T_C$  for contacts along the  $c$  axis and  $\Delta \simeq 2.9k_B T_C$  for contacts along the  $ab$  plane. The spectra additionally show structures that allow extracting the characteristic energy of the boson that mediates the superconducting coupling ( $E_p \simeq 11$  meV). A closer inspection of the low-energy conductance also allows identifying a smaller gap  $\Delta \simeq 1.4k_B T_C$ . These two gaps, as well as the position of the electron-boson structure, agree very well with results reported in literature. Subsequently,

the  $Fe(Se,Te)$  films are intercalated with  $H^+$  by using the ionic liquid gating technique, to inducing a higher- $T_C$  phase. Despite the volatility of the  $H^+$  insertion, I demonstrate that applying a gate voltage  $2.4 \leq V_G \leq 2.7$  V leads to an increase in  $T_C$  from 16 K to 21.1 K.

Finally, I attempt to perform PCARS measurements in situ ( i.e. in the cell used for ionic liquid gating) on the intercalated sample, so as to overcome the volatility of  $H^+$  insertion. This approach could open new avenues for investigating the spectroscopic properties of protonated materials, which are expected to exhibit entirely new characteristics.

# Acknowledgements

First and foremost, I would like to express my heartfelt gratitude to Prof. Renato Gonnelli for his infinite patience and the love for knowledge that he has imparted to me during these months of work. A special thank you goes to Prof. Dario Daghero, whose exceptional and rare teaching ability made part of this journey clearer and more interesting. I am also deeply grateful to Dr. Erik Piatti, who has guided me step by step from my very first to my last scratch on the measurement samples! Finally, I want to thank Ms. Gaia Gavello, with whom I had the good fortune to share these months of work, lightening them with our little coffee breaks. As I reach the end of this journey, if I feel proud and happy about the choice I made six months ago, it is largely thanks to La.T.E.S.T 1 at DISAT.

I also want to thank the Politecnico di Torino, which, despite the challenges faced over the years, has allowed me to acquire new knowledge and strengthen my belief that learning is the greatest gift we have.

I am deeply grateful to my family, who, through many sacrifices, have enabled me to embark on and complete this journey. They have always stood by my side, supporting me, and for that, I can never be thankful enough. I love you all endlessly.

Lastly, I want to thank Marika, my perfect half, the only person who knows every string of my heart and soul. If there is anyone happier than me today, it is her. I love you.

Christian

*Ai miei nonni,  
che mi hanno insegnato  
il più caldo amore*



# Table of Contents

<b>List of Figures</b>	VII
<b>1 Introduction</b>	1
1.1 Motivation . . . . .	1
1.2 State of the art . . . . .	2
1.3 Thesis structure . . . . .	3
<b>2 Iron based superconductors</b>	6
2.1 Basic concepts of superconductivity . . . . .	6
2.2 BCS theory for conventional superconductors . . . . .	7
2.2.1 The role of electron-phonon interactions . . . . .	8
2.2.2 BCS approach . . . . .	8
2.3 Classification of superconductors . . . . .	10
2.3.1 Type I/II superconductors . . . . .	10
2.3.2 Conventional and unconventional superconductors . . . . .	12
2.3.3 High/Low $T_C$ superconductors . . . . .	13
2.3.4 Topological superconductors . . . . .	13
2.3.5 Majorana fermions and topological superconductivity . . . . .	15
2.3.6 Signature of Majorana Fermions in TSCs . . . . .	16
2.4 Fe-based superconductors . . . . .	17
2.4.1 General information about Fe-based superconductors . . . . .	17
2.4.2 Fe-compounds structure . . . . .	18
2.4.3 Unconventional superconducting coupling . . . . .	20
2.4.4 Fermi surface structure . . . . .	20
2.4.5 Multiband character of superconductors . . . . .	22
2.4.6 Nesting of Fermi surfaces . . . . .	22
2.4.7 Superconductive band coupling . . . . .	23
2.4.8 Analysis of structural parameters . . . . .	24

<b>3</b>	<b>Properties of the <math>Fe(Se, Te)</math> superconductors</b>	<b>25</b>
3.1	General features of $FeSe$ related superconductors . . . . .	25
3.1.1	Iron-selenide ( $FeSe$ ) . . . . .	26
3.1.2	Iron-telluride ( $FeTe$ ) . . . . .	28
3.2	Iron-selenide-telluride ( $Fe(Se, Te)$ ) . . . . .	29
3.2.1	Te-substitution effect on $FeSe$ compound . . . . .	30
3.2.2	Topological character of $FeSeTe$ . . . . .	32
3.3	Multi-band Eliashberg theory . . . . .	36
<b>4</b>	<b>Point-contact spectroscopy (PCS)</b>	<b>39</b>
4.1	Basics concepts of PCS . . . . .	39
4.1.1	Different spectroscopy regimes . . . . .	40
4.1.2	Soft-PC . . . . .	44
4.2	Andreev reflection . . . . .	44
4.3	Fitting models . . . . .	48
4.3.1	BTK 1D model . . . . .	48
4.3.2	2D BTK model . . . . .	51
4.3.3	BTK model for d-symmetry gap . . . . .	55
4.3.4	BTK multi-band model . . . . .	56
<b>5</b>	<b>Ionic gating and ion intercalation procedures</b>	<b>58</b>
5.1	Ionic gating . . . . .	58
5.2	Ion intercalation . . . . .	62
5.3	Protonation . . . . .	63
<b>6</b>	<b>Materials and methods</b>	<b>67</b>
6.1	$Fe(Se, Te)$ properties . . . . .	67
6.1.1	Sample growth . . . . .	67
6.2	Sample mounting . . . . .	68
6.2.1	Resistivity measurement . . . . .	68
6.2.2	Horizontal setup . . . . .	70
6.2.3	Vertical setup . . . . .	73
6.3	Cooling systems . . . . .	75
6.3.1	Pulse-tube cryocooler . . . . .	75
6.3.2	Wet cryostat . . . . .	76
<b>7</b>	<b>Experimental results</b>	<b>81</b>
7.1	Measurements in pristine $Fe_{1+\delta}(Se_{0.5}Te_{0.5})$ . . . . .	82
7.1.1	AFM Measurements . . . . .	82
7.1.2	Electron dispersive X-rays (EDX) . . . . .	85
7.1.3	Transport measurements . . . . .	86
7.1.4	Point contact Andreev reflection spectroscopy . . . . .	88

7.2	Protonated samples measurements . . . . .	101
7.2.1	AFM measurements . . . . .	101
7.2.2	Transport measurements . . . . .	102
7.2.3	Point contact Andreev reflection spectroscopy . . . . .	110
<b>8</b>	<b>Conclusions and future perspective</b>	<b>117</b>
	<b>Bibliography</b>	<b>120</b>

# List of Figures

2.1	<i>The two key features of the superconducting phase. On the left, a pictorial representation of the abrupt drop to zero resistivity (<math>\rho</math>); on the right the expulsion of the magnetic field. Reprinted from [15]. . . . .</i>	6
2.2	<i>Pictorial view of the formation of a Cooper pair. The first electron (on the right) passes through ions, exciting them and generating a surplus of positive charge, which attracts the second electron (left), thus forming the Cooper pair. Reprinted from [19]. . . . .</i>	9
2.3	<i>Illustrates the behavior of the superconducting gap, normalized to its value at <math>T = 0</math>. On the horizontal axis, the reduced temperature (<math>T/T_C</math>) is plotted. The graph compares theoretical results with experimental data from various conventional superconducting materials. Reprinted from [22]. . . . .</i>	11
2.4	<i>On the left we see the pictorial phase transition characterizing the type I superconductors in terms of external field and temperature; on the right the phase diagram related to the type II superconductors. Reprinted from [23]. . . . .</i>	11
2.5	<i>Diagrammatic representation of the vortices that appear in type II superconductors. Reprinted from [26]. . . . .</i>	12
2.6	<i>Classification of gapped topological phases of matter an the associated TSC classes. Reprinted from [28]. . . . .</i>	14
2.7	<i>A pictorial representation of how Majorana fermions emerge from the interaction of electrons and holes with Cooper pairs, rendering electrons and holes indistinguishable. Reprinted from [39]. . . . .</i>	16
2.8	<i>The image shows the behavior of the Majorana fermions involved in the heat conduction. Reprinted from [46]. . . . .</i>	17
2.9	<i>The bcc (body-centered cubic) atomic structure on the left, and the hcp (hexagonal close-packed) structure on the right. . . . .</i>	18
2.10	<i>Schematic representation of different Fe-based families, highlighting structural differences. Reprinted from [50]. . . . .</i>	19

2.11	<i>Simplified view of the spherical Fermi surface of monovalent metals. Reprinted from [54]. . . . .</i>	21
2.12	<i>3D reconstruction of the Fermi surface in LaFeASO. In the figure, the holonic Fermi surfaces near the corners are related to the <math>\Gamma</math>-point (associated with holes), while the central group corresponds to the M-point (associated with electrons). Reprinted from [56] . . . . .</i>	21
2.13	<i>The figure shows how the gaps, corresponding to different bands, behave with respect to the reduced temperature <math>T/T_C</math>, following the Shul and Matthias model. It can be observed that the gaps vanish at different critical temperatures, which depend on the strength of the intraband coupling. The case of weak interband coupling is represented by the red dashed line, while strong interband coupling is shown by the blue dashed line, exhibiting a tail as <math>T \rightarrow T_C</math>. Reprinted from [57] . . . . .</i>	23
3.1	<i>Fermi sheets in the folded Brillouin Zone, whose boundaries are the represented by solid blue line. Reprinted from [67]. . . . .</i>	26
3.2	<i>Phase diagram of <math>Fe_{1.01}Se</math> as function of pressure. Reprinted from [69]. . . . .</i>	27
3.3	<i>Temperature dependence of resistivity for FeSe. The upper inset shows the behavior of resistivity with respect to temperature under high magnetic fields. Reprinted from [68]. . . . .</i>	27
3.4	<i>Fermi surface of the bulk FeSe through calculations. Reprinted from [80].</i>	28
3.5	<i>(a) Fermi surface of <math>Fe_{1.06}Te</math> at <math>T = 135</math> K; (b) Spectral weight distribution around <math>E_F</math>; (c) Fermi surface of <math>Fe_{1.06}Te</math> at <math>T = 15</math> K. Reprinted from [86] . . . . .</i>	29
3.6	<i>The figure shows the resistivity as a function of temperature for different concentration of tellurium. Reprinted from [5]. . . . .</i>	31
3.7	<i>(a) Lattice expansion ratios of the tetragonal <math>FeSe_{1-x}Te_x</math> found through X-ray at room temperature, where <math>a_0</math> and <math>c_0</math> are referred to the lattice parameters of FeSe; (b) The picture shows the behavior of the <math>\gamma</math> angle as a function of <math>x</math>, together with the critical temperature value. Note that here the critical point is defined as the temperature at which the resistance reaches the 90% of the normal state value. Reprinted from [5]. . . . .</i>	32
3.8	<i>The plot shows the conductance spectra with different tunnel coupling values defined in <math>G_N</math>. The vertical axis is then given by <math>dI/dV(2e^2/h)</math> while the horizontal one measure energy in meV. Reprinted from [94].</i>	34

3.9	(A) A pictorial representation of topological superconductivity on the surface of $FeTe_{0.55}Se_{0.45}$ , highlighting the distinction between bulk and surface states. In the bulk, the electrons are not spin-polarized, and the $s$ -wave superconducting pairing is topologically trivial. (B) When a magnetic field is applied, it induces vortices in the system. These vortices act as boundaries for the topological superconductivity on the surface, where Majorana bound states are expected to emerge within the vortex cores. Reprinted from[89]. . . . .	35
4.1	Pictorial experimental setup for PCS measurement in the two configurations. (a) Metallic probe that contacts the surface of the material; (b) Soft-PC procedure that uses Ag-paint or IN-flake spot to stabilize the metallic wire. Reprinted from [105]. . . . .	40
4.2	The figure shows the three kind of scattering that can experience the electrons: (a) zero-order contribution(no scattering); (b)single collision and momentum inversion;(c)double scattering. Reprinted from [107]. . . . .	42
4.3	The panels illustrate the electron distribution at the center of a perfect contact across three distinct transport regimes: (a) Ballistic, (b) Intermediate,(c) Thermal. Reprinted from [55]. . . . .	43
4.4	Schematic view of how to build the soft-PC setup in the case of the current directed along $ab$ plane (top panel) and along the $c$ axis (bottom). Reprinted from [105]. . . . .	45
4.5	Schematic representation of PCARS in an ideal N-S junction at zero temperature, illustrating the cases in which the electron energy is larger or smaller than the superconducting energy gap. When the electron energy is larger than the gap, it generates a Cooper pair, and normal transmission occurs. When the electron energy is smaller than the gap, Andreev reflection takes place, where a hole is reflected back into the normal metal. Reprinted from[105]. . . . .	46
4.6	The picture proposes a comparison between the N-N/N-S junction through their I-V characteristic. The panel below shows the normalized conductance of the N-S junction at $T=0$ following the BTK model. Reprinted from [55]. . . . .	47
4.7	Pictorial representation of the probabilities of the cases A/C. Reprinted from [105]. . . . .	49
4.8	Schematic view of the probabilities associated to the possible reflection of cases B and D. Reprinted from [105]. . . . .	50

4.9	<i>The scheme shows the behavior of the normalized conductance at fixed <math>T</math> (left) and <math>Z</math>(right) letting free respectively <math>Z</math> and <math>T</math>. On the left panel we can observe that as <math>T</math> increases the conductance gets lowered passing from a two-picked shape to a single peak one set at zero bias. Reprinted from [105]. . . . .</i>	51
4.10	<i>Geometric representation of the electron crossing the N-S interface with an angle <math>\theta_N</math> with respect to the interface itself. Reprinted from [105]. . . . .</i>	52
4.11	<i>Example of fitting curve where the broadening parameter is present with different values with respect to the gap one. Reprinted from [105].</i>	54
4.12	<i>The picture shows on the left a schematic representation of an s-wave anisotropic gap, while on the right a d-wave one. Reprinted from [105].</i>	55
4.13	<i>The picture shows different curves in the <math>\alpha = 0</math> case in the case of anisotropic s-wave gaps (a) and a d-wave gap symmetry. Reprinted from [105]. . . . .</i>	56
4.14	<i>The figure shows the normalized conductance curve for two values of <math>Z</math> in a d-wave superconductor and the appearance of the ZBCP. Reprinted from [105]. . . . .</i>	57
5.1	<i>The picture show a schematic view of the the MIS structure before the gate bias application (a) and with gate voltage <math>V_G \neq 0</math> leading to the FET architecture. Reprinted from [114] . . . . .</i>	59
5.2	<i>Zoom on the interface between the ionic liquid and semiconductor in a general EDL-FET structure. Reprinted from [118]. . . . .</i>	61
5.3	<i>Pictorial scheme about the ion intercalation of <math>Li^+</math> and <math>Na^-</math> in a layered material such as <math>MoS_2</math>. Reprinted from [121]. . . . .</i>	62
5.4	<i>Schematic view of the two kind of applied voltage which leads to the oxygen (a) and hydrogen (b) intercalation. Reprinted from [122] . .</i>	63
5.5	<i>Schematic experimental setup used by Cui's group in [3] . . . . .</i>	64
5.6	<i>Resistance as a function of temperature of <math>FeSe_{0.93}S_{0.07}</math> compound post protonation technique. Reprinted from [3] . . . . .</i>	65
6.1	<i>Example of <math>Fe(Se,Te)</math> mounting. We can see the G.E. Varnish in the background, on top the sample with the Ag-spots. The black arrow define the flow of the drain-source current (<math>I_{DS}</math>), while the red arrow indicates the voltage drop between two electrodes . . . . .</i>	70
6.2	<i>The panel shows the theoretical configuration of the 4-wire technique. Reprinted from [130]. . . . .</i>	70
6.3	<i>Representation of a complete horizontal mounting of the sample. The system is now ready for cryogenic measurements. . . . .</i>	72

6.4	<i>Complete mounting of the sample on the cold finger of the pulse-tube cryocooler. . . . .</i>	73
6.5	<i>Sample chamber of the cryogenic insert used in the Oxford top-loading wet cryostat. Here, the sample was prepared for soft-point contact measurement, so the pool was not necessary. . . . .</i>	74
6.6	<i>On the left, we can see the fiberglass base with the four purpose-designed angles, where a copper layer is still present to ensure electrical conductivity. In the central panel, the four angles are welded with tin, on top of which indium can also be welded. The last panel shows the complete mounting of the sample on the support, ready to be glued to the descendant. . . . .</i>	75
6.7	<i>The figure shows the vertical setup, ready to be closed by the metal shield, which prevents thermal fluctuations during the measurement. At the bottom, we can see the thermometer, which is typically linked through G.E. Varnish behind the sample's copper support. . . . .</i>	77
6.8	<i>Vapour pressure of various cryoliquids. The horizontal axis measures temperature, while the vertical axis represents the vapour pressure. Reprinted from[132]. . . . .</i>	78
6.9	<i>The figure shows the LaTEST 1 cryocooler, integrated with the recondenser. Here, the descendant was inserted for point-contact measurements. . . . .</i>	79
6.10	<i>The image shows, on the left, the booster pump, responsible for maintaining low vacuum conditions, and on the right, the turbo pump, which is tasked with achieving high vacuum. . . . .</i>	80
7.1	<i>X-Rays spectrum and transport measurements performed by Professor Kazumasa on <math>Fe(Se_{0.5}Te_{0.5})</math>. . . . .</i>	81
7.2	<i>The left panel shows a two-dimensional AFM image that illustrates a region of the sample used for the analysis. The right panel exhibits the AFM image which highlights the grain boundaries of the film. . .</i>	82
7.3	<i>Innova Bruker atomic force microscope. . . . .</i>	83
7.4	<i>On the left, a height profile used to determine the sample thickness is shown. The presence of an intermediate plateau is due to the incomplete breaking of the film during the cutting process of the corresponding <math>Fe(Se,Te)</math> batch. The right panel displays the corresponding 3D region from which the height profile was extracted.</i>	83
7.5	<i>The left panel shows the distribution of the equivalent disk radius. The right image shows the distribution of the grain surface area. . .</i>	84
7.6	<i>EDX spectrum provided by the x-rays emitted by the atoms. . . . .</i>	85
7.7	<i>Resistance as a function of temperature up to 100 K. . . . .</i>	86

7.8	<i>Resistivity as a function of temperature related to the sample configuration shown in the inset. . . . .</i>	86
7.9	<i>The upmost figure shows the behavior of the normalized resistance as a function of the absolute temperature. The bottom panel shows the first derivative of the normalized resistance and the corresponding gaussian fit. . . . .</i>	88
7.10	<i>The figure shows the differential conductance curves on varying the temperature. The inset illustrates the resistivity measure as function of temperature. The blue dot represents the local critical temperature (<math>T_C^A</math>) and the red dot signal the <math>T^{50\%}</math> of the sample. . . . .</i>	89
7.11	<i>Here we show the theoretical curve (blue circles) and the normalized fit curve (red line) at the lowest temperature, i.e <math>T = 2.05</math> K. We also report the values of the superconducting gaps. . . . .</i>	91
7.12	<i>The panel shows the fitting (red solid line) of the normalized conductance curve (blue circles), focusing on the upper part. We show that, actually there exist two gaps in that energy range. The parameter are listed on the right together with the values of the order parameter. . . . .</i>	92
7.13	<i>The picture illustrates the temperature dependence of the normalized conductance curves for each selected value of temperature. . . . .</i>	93
7.14	<i>The upmost figure shows the temperature dependence of the superconducting gaps values (blue squares and green circles) along with the behavior of the gamma parameters (blue and green stars). In particular, we compare the temperature behavior of the superconducting gaps with the theoretical trend set by BCS theory (solid blue line). The bottom figure shows the temperature dependence of the barrier parameters. . . . .</i>	94
7.15	<i>The figure shows the behavior of the <math>-d^2I/dV^2</math> with respect to the bias voltage for different values of temperature (the same of the one listed in figure 7.13). Note how the energy peak actually decreases when temperature increases. The curves are shifted by a constant offset for clarity. . . . .</i>	95
7.16	<i>The panel shows the behavior of <math>E_P</math> and <math>\Omega_b</math> as a function of temperature. We compare the first to the behavior of <math>\Delta^*</math> and the second one to the right-hand side of equation (7.4). . . . .</i>	96
7.17	<i>The image shows the differential conductance curves for different values of temperature for a point-contact made along the c-axis of the sample. . . . .</i>	97
7.18	<i>The panel shows the normalized conductance curve and its theoretical curve for <math>T = 2.06</math> K. . . . .</i>	98

7.19	<i>The temperature dependence of the normalized conductance curve is plotted here, where the effect of the critical current becomes increasingly significant as the temperature rises.</i>	99
7.20	<i>The figure illustrates the behavior of the order parameters as a function of temperature.</i>	99
7.21	<i>The plot shows the trend followed by the barrier parameter as a function of temperature.</i>	100
7.22	<i>3D hight profile of <math>Fe(Se_{0.5},Te_{0.5})</math>, some peaks in the image coincides with impurities located on the surface if the sample.</i>	101
7.23	<i>2D representative AFM topography map of <math>Fe(Se_{0.5}Te_{0.5})</math> thin film. In the right corner there are some lighter regions which corresponds to some impurities.</i>	102
7.24	<i>Zoom on the surface of the sample highlighting the topology of <math>Fe(Se,Te)</math> after the protonation process.</i>	102
7.25	<i>Example of sample mounting used for the ions intercalation process.</i>	103
7.26	<i>The top three panels show the resistivity curve as a function of the gate voltage for three different values of <math>V_G</math>. The bottom images illustrates the gate current as a function of the bias gate voltage.</i>	104
7.27	<i>Normalized resistance (with <math>R(22\text{ K})</math>) plotted as a function of temperature for a sample under <math>V_G = 1.8\text{ V}</math>.</i>	105
7.28	<i>Normalized resistance as a function of temperature for the pristine and protonated case at <math>V_G = +2.4\text{ V}</math>. Both graphs are normalized with the resistance value at <math>T = 35\text{ K}</math>.</i>	106
7.29	<i>The panel shows the resistance curves for different values of gate voltage compared to the pristine sample plotted as a function of temperature. We note that all the samples were characterized by a similar geometry.</i>	107
7.30	<i>Comparison between the pristine normalized resistance and that of the protonated sample at <math>V_G = +2.7\text{ V}</math> as a function of temperature.</i>	108
7.31	<i>This image shows the experimental setup used for in situ PCARS measurement. Here the stycast pool is substituted by a fiberglass pool, which not only plays the same role of the stycast-pool, but overcomes some technical difficulties (for instance the height difference between gate electrode and sample).</i>	111
7.32	<i>Temperature dependence of differential conductance curves as a function of the bias voltage.</i>	112
7.33	<i>The panel shows the experimental curve (blue circles) along with the fitted one (red line).</i>	113
7.34	<i>Differential conductance curves as a function of bias voltage as the temperature increases.</i>	114

7.35 *The panel shows the experimental curve (blue circles) along with the fitted one (red line). . . . .* 115



# Chapter 1

## Introduction

### 1.1 Motivation

Superconductivity is an intrinsic property observed in certain metals, characterized by an abrupt drop to zero resistivity when cooled below a critical temperature ( $T_C$ ). The first discovered superconductors exhibited very low critical temperatures, which initially made the study of superconductivity challenging. However, years later, the discovery of Cu-based superconductors marked a significant turning point, as they were characterized by much higher critical temperatures. Therefore, this discovery made possible the first step towards the room temperature superconductivity, one of the most important goals in solid state physics. In 2008, the discovery of a new class of materials, the so-called iron-based superconductors, was crucial, even though they exhibit a lower critical temperature compared to cuprates. Therefore, the two families show notable differences, particularly in their atomic structure. In fact, Cu-based superconductors generally show higher anisotropy compared to their iron-based counterparts. The latter shows a different behavior with respect the 'conventional' superconductor, suggesting a different behavior related to the formation of the Cooper pairs; actually the hope was that, since the screened Coulomb interactions were weaker than the cuprates ones, they could be more theoretically treatable in order to provide more information despite their 'unconventional' behavior.

Another topic that was heavily investigated in the last two decades is topological superconductivity, which may also be hosted in Fe-based compounds. Topological superconductivity is a property that is characterized by a non trivial topology of the electronic structure. This means that the superconducting state comes with a topological invariant quantity. Indeed, the topological superconductors showed interesting and promising applications in the modern technology, for instance they find space in the relatively new field of quantum computing. Indeed, topological

superconductors can host Majorana bound states (known as Majorana zero modes) which can be used as a better qubits. In fact, theoretically speaking, the qubits generated through Majorana bound states, are more resistant to noise which lead to longer decoherence time.

The work starts by a characterization of the pristine  $FeSe_{0.5}Te_{0.5}$  thin films by means of electric transport measurements as a function of temperature, to study the normal-state resistivity and determine their  $T_C$ . The superconducting phase is further studied by point-contact Andreev-reflection spectroscopy (PCARS). The  $dI/dV$  vs  $V$  spectra contain information of the superconducting gap  $\Delta$  thanks to a quantum phenomenon called Andreev reflection. Therefore, by analyzing the PCARS spectra obtained in  $Fe(Se,Te)$  pristine films, we identify structures that can be associated with the superconducting gap.

Subsequently, the  $Fe(Se,Te)$  films are intercalated with  $H^+$  by using the ionic liquid gating technique, to inducing a higher- $T_C$  phase. Finally, I attempt to perform PCARS measurements in situ ( i.e. in the cell used for ionic liquid gating) on the intercalated sample, so as to overcome the volatility of  $H^+$  insertion.

## 1.2 State of the art

Ion hydrogen intercalation has emerged as a crucial technique in materials science, allowing for the tuning of electronic properties in metals. Over the past half-century, extensive research has focused on its potential applications in superconductivity. Among numerous examples, it has been observed that hydrogen ion intercalation in palladium (Pd) induces a superconducting phase, increasing the transition temperature to  $T_C = 9.4$  K; a similar effect occurs in thorium (Th) at  $T_C = 8.2$  K [1].

In recent years, research has expanded its horizons by applying ionic intercalation techniques, particularly, potentially opening a broader path toward what is known as room-temperature superconductivity at ambient pressure.

Moreover, this technique has been applied also to layered materials, such as transition metal dichalcogenide (TMD) compounds. Indeed, ionic gate driven hydrogen intercalation process can induce a superconducting phase transition, confirming the capability of the technique to tune the intrinsic quantum phases of the materials [2].

Within this framework, iron-based superconductors stand out, exhibiting some of the highest  $T_C$  values, second only to the aforementioned cuprates. In particular, iron chalcogenides have garnered special interest, following experimental results demonstrating that protonated  $FeSe$  samples exhibit a superconducting phase with a critical temperature of 45 K starting from the 8 K of the pristine material [3].

*FeSe* appears to be a particularly promising material for ionic intercalation due to its simple and layered crystalline structure, which plays a crucial role in its superconducting properties [4]. These unique characteristics make *FeSe* an excellent testbed for this technique, facilitating the study not only of *FeSe* itself but also of its derived compounds obtained through partial atomic substitution.

This context includes the study conducted in this thesis, which aims to provide a comprehensive characterization of  $Fe(Se, Te)$  thin films, whose maximum critical temperature can reach 23 K, as shown in the literature [5, 6].

Beyond the potential increase in its critical temperature,  $Fe(Se, Te)$  is also of great interest because studies suggest that  $Fe(Se, Te)$  supports a non-trivial  $\mathbb{Z}_2$  topological invariance, classifying it as a topological superconductor [7]. This characteristic makes  $Fe(Se, Te)$  highly significant for applications, as it can host Majorana zero modes, as suggested by scanning tunneling microscopy and spectroscopy studies [8, 9, 10].

Given this context, the objective of this thesis is to investigate the superconducting phase of  $Fe(Se_{0.5}Te_{0.5})$  and its response to hydrogen intercalation, by combining electric transport and spectroscopic measurements. To this end, we employ the point-contact Andreev reflection spectroscopy (PCARS) technique, which exploits the quantum phenomenon of Andreev reflection to assess the structure of the superconducting gap and, in principle, to look for possible signs of zero-bias conductance peaks (ZBCP). Indeed, the presence of Majorana fermions, in proper conditions, may be associated to the observation of ZBCP with specific characteristics that may appear in PCARS measurements [11, 12].

Concerning the structure of the superconducting gap, literature indicates that  $Fe(Se, Te)$  exhibits a multiband structure with two superconducting gaps [13]. Additionally, recent spectroscopic studies have revealed that  $Fe(Se, Te)$  is characterized by strong electron-boson interactions, typical of iron-based superconductors. This interaction manifests as energy peaks that are clearly visible in differential conductance curves, which can sometimes be misleading, as these values might be mistakenly interpreted as actual superconducting gaps [13, 14].

## 1.3 Thesis structure

The thesis is structured as follow:

- **Chapter 2:** This chapter aims to introduce the reader to fundamental concepts of superconductivity. We explore the relationship between BCS theory and Ginzburg-Landau theory, both of which describe the emergence of superconductivity in materials. Additionally, we classify different types of superconductors based on their defining characteristics.

We also provide an introduction to topological superconductors, emphasizing

their significance in modern applications, particularly due to their connection to Majorana fermions. The final section of the chapter focuses on Fe-based superconductors, discussing their atomic structure and the characterization of their Fermi surfaces.

- **Chapter 3:** This chapter presents the main characteristics of the iron-chalcogenides, specifically focusing on iron selenide telluride ( $Fe(Se,Te)$ ), which is the subject of this study. We begin by introducing the fundamental properties of

$FeSe$

, discussing its phase diagram and structural characteristics. A similar analysis is provided for the  $FeTe$  compound.

The core of the chapter is dedicated to a detailed examination of  $Fe(Se,Te)$ , including its structural properties, Fermi surface shape, and the effects of Te substitution on the properties of

$FeSe$

. Additionally, we investigate the superconducting behavior of  $Fe(Se,Te)$  as a function of the Se-Te ratio.

Special attention is given to Eliashberg theory, which explains the multiband superconductivity of the compound. Finally, we review key experimental evidence from the literature that supports the topological nature of iron selenide telluride.

- **Chapter 4:** This chapter aims to provide a comprehensive understanding of the point-contact spectroscopy (PCS) technique. We discuss the different operational regimes of PCS, such as the thermal and ballistic regimes. Additionally, we introduce the *soft-PC* method, which was employed in our experimental study and is explained in detail within this chapter. The second part of the chapter provides a physical description of the quantum phenomenon of Andreev reflection, which is detectable through the PCS technique and plays a crucial role in characterizing the properties of  $Fe(Se,Te)$ . Since a theoretical framework is necessary to analyze the conductance spectra of the material, we introduce the Blonder-Tinkham-Klapwijk (BTK) model and its derivations. This model allows us to extract the value(s) of the superconducting gap(s), enabling a complete characterization of the superconducting phase.
- **Chapter 5:** This chapter provides an introduction to the ionic gating technique, along with the ionic intercalation procedures. The latter are characterized by the presence of a gate voltage which generates an electric field on the

system. This electric field plays a crucial role in driving ions into the target material.

In our study, the process is carried out using a deep eutectic solvent (DES) as an electrolyte, positioned between the  $Fe(Se, Te)$  sample and the metallic gate. The electrolyte undergoes ionic dissociation, providing  $H^+$  ions that, under the influence of the electric field, are intercalated into the compound. Finally, we evaluate the efficiency of this procedure when applied to iron-chalcogenide materials.

- **Chapter 6 and 7:** Chapter 6 describes the materials and methods employed to perform various types of measurements, including resistivity and point-contact spectroscopy. Additionally, we provide a detailed characterization of our sample, which follows the stoichiometry  $Fe_{1+\delta}(Se_{0.5}Te_{0.5})$ . Chapter 7, instead, presents all the obtained results, from the pristine sample to the protonated one. In particular, we focus on the electrical transport properties and the spectroscopic study performed via point-contact Andreev reflection spectroscopy (PCARS).
- **Chapter 8:** In the final chapter, we present the conclusions of this work by summarizing the key findings and results obtained. Additionally, we discuss potential future directions that could be explored following this study on the iron selenide telluride compound.

# Chapter 2

## Iron based superconductors

### 2.1 Basic concepts of superconductivity

Superconductivity is a property observed in several metals that undergo a phase transition when cooled below a **critical temperature**  $T_C$ . This transition is marked by an abrupt drop to zero resistivity in the material, signaling the shift from the normal state to the superconducting (SC) state. In addition to the resistivity dropping to zero, another hallmark of superconductivity is the expulsion of magnetic field flux from the bulk of the material, i.e. the Meissner effect (fig: 2.1).

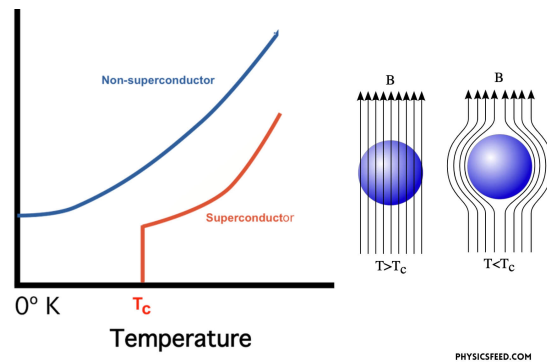


**Figure 2.1:** *The two key features of the superconducting phase. On the left, a pictorial representation of the abrupt drop to zero resistivity ( $\rho$ ); on the right the expulsion of the magnetic field. Reprinted from [15].*

The first superconductor was discovered in 1911 by physicist Heike K. Onnes, who observed this phenomenon in a highly pure mercury wire cooled to 4.2 K. During the cooling process, Onnes noted a sharp drop in the material's resistivity. This groundbreaking discovery dramatically transformed the field of condensed

matter physics, opening new possibilities for technological applications [16].

Following this discovery, research efforts aimed at identifying other materials showing similar behavior. Soon, the list of superconductors became longer and longer, with the discovery of superconducting phase in elements like gallium (Ga), lead (Pb), and tin (Sn), all of which showed analogous superconducting properties, except for their critical transition temperatures ( $T_C$ ). Therefore, the first important result was the observation of a non-universal  $T_C$  value, which instead depends on the material and its intrinsic characteristics. The superconducting state persists up to a critical magnetic field  $H_c$ , beyond which superconductivity is destroyed. This threshold defines type I superconductors, which completely expel the magnetic field. In contrast, type II superconductors exhibit an intermediate behavior at fields in the range  $H_{c1} < H < H_{c2}$ . When the applied magnetic field exceeds a lower critical field  $H_{c1}$ , the magnetic field partially penetrates the material through vortices, while retaining its superconducting state. Only once  $H_{c2}$  is reached does the superconducting state break down entirely.

After the superconducting phase transition was first observed, physicists sought to uncover the mechanisms behind this phenomenon. For many metals and also compounds, this behavior is explained by the BCS theory [17], which characterizes conventional superconductors. However, some of the superconductors are characterized by a stronger electron-phonon coupling which can be explained by the Eliashberg theory, a generalization of the BCS theory. Finally, the non-conventional superconductors are defined by an electron-electron interaction which cannot be treated with the previous theory, that are implemented on a phenomenological level.

## 2.2 BCS theory for conventional superconductors

The existence of the superconducting phase is explained by the BCS theory, named after J. Bardeen, L. Cooper, and R. Schrieffer, who published their work in 1957. Their theory aims to analyze the microscopic properties of superconductors. According to this theory, there exists an attractive potential between conduction electrons, allowing them to overcome the Coulomb repulsion between like charges. At temperatures approaching absolute zero, the electrons in a metal tend to occupy all possible energy states, starting from the lowest up to a specific threshold known as the Fermi level  $\epsilon_F$ , which characterizes the maximum occupied energy state. Each energy level can hold only two electrons, which must adhere to the Pauli exclusion principle.

In particular, only electrons near the Fermi energy contribute to conduction, while the others form a stable configuration known as the Fermi sea, highly stable when  $T = 0$  K. As proposed by Cooper, two coupled electrons introduced into the

Fermi sea at zero temperature, find space among the already occupied levels instead of positioning over the Fermi energy. This results in the formation of Cooper pairs, which must have an energy smaller than the Fermi level. The formation of these pairs creates an instability among the electrons near the Fermi level, triggering microscopic condensation.

Therefore, the superconducting state arises due to the collective behavior of these Cooper pairs, which exhibit long-range quantum coherence. The superconducting state arises from the interplay between the Cooper pair's properties and the mechanism enabling their formation. Although electrons intrinsically obey Fermi-Dirac statistics due to their fermionic nature, Cooper pairs behave as particles that follow the Bose-Einstein distribution function [17, 18].

### 2.2.1 The role of electron-phonon interactions

The potential existing between two electrons that leads to the formation of a Cooper pair has been investigated from a microscopic point of view. The origin of this weak attractive interaction is mediated by the presence of phonons (i.e., excitations arising from deviations in the periodicity of the metal lattice). Electrons moving through the lattice excite the ionic lattice, which reacts by emitting a phonon that can be absorbed by another electron (fig: 2.2). Following this mechanism, the process becomes continuous and highly dynamic, resulting in consecutive interactions between different electrons. This creates a cycle that begins with the emission of a phonon and ends with its absorption by a moving electron, ultimately creating a bond defined by the Cooper pair's length (in conventional superconductors, this length is usually of the order of  $10^4$  Å).

An energy can also be associated with this pair. According to BCS theory, at  $T = 0$  K, the relative energy is given by  $\epsilon = 3.53k_B T_C$ , where  $k_b$  is the Boltzmann constant. This energy decreases as the temperature increases, reaching zero when  $T = T_C$ , which marks the breaking of the Cooper pair.

The key aspect of Cooper pair formation lies in the interaction of electrons with phonons. It is, therefore, unsurprising that most metals that are not good conductors exhibit a superconductive phase. In contrast, good conductors such as gold (Au) and silver (Ag) are characterized by very weak interactions between electrons and phonons. This weak interaction reduces the effect of phonon scattering on the motion of negatively charged particles, reducing the resistivity, but also weakening the pairing interaction required for the onset of superconductivity.

### 2.2.2 BCS approach

The Ginzburg-Landau theory seeks to describe the properties of superconductors from a macroscopic perspective, rooted in microscopic principles. To achieve this,

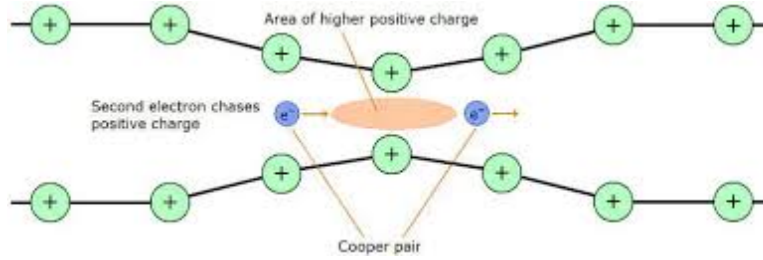


**Figure 2.2:** Pictorial view of the formation of a Cooper pair. The first electron (on the right) passes through ions, exciting them and generating a surplus of positive charge, which attracts the second electron (left), thus forming the Cooper pair. Reprinted from [19].

it introduces a complex function known as the order parameter  $\psi(\mathbf{r})$ , which encapsulates the essential features of the superconducting phase transition. Specifically, this function vanishes when the temperature exceeds the critical temperature, while its magnitude quantifies the degree of superconducting order at a given position  $\mathbf{r}$  for  $T < T_C$ .

From the BCS theory perspective, the order parameter can represent a one-particle wave function describing the center of mass of a Cooper pair—composed of two electrons occupying the same quantum state. Since  $\psi(\mathbf{r})$  does not capture the relative positions of the particles within the pair, its applicability is limited to phenomena that vary slowly compared to the size of the Cooper pair. Below  $T_C$ , this characteristic length is given by the correlation length of the Cooper pair [20, 21].

When there is no external field and no current flowing through the superconductor, the order parameter uniformly describes all particles in the ground state. This observation demonstrates that the two theories—BCS and Ginzburg-Landau—are not independent. The Ginzburg-Landau macroscopic theory can be understood as the limit of BCS theory near the critical temperature (i.e., when  $T \rightarrow T_C$ ). In this framework, the order parameter is mapped to another fundamental quantity, known as the superconducting gap  $\Delta(\mathbf{k})$ , where  $\mathbf{k}$  represents the particle’s wave vector.

In general, the wave vector  $\mathbf{k}$  is directly linked to the particle’s energy, meaning the value of the gap may vary accordingly. In simplified cases, the gap can be treated as a constant, independent of  $\mathbf{k}$ . The modulus describes the range of forbidden energies for quasiparticles (electrons deriving from the breaking of a Cooper pair) near the Fermi level, such that the total energy of one of such electron is given by:

$$E_k = \sqrt{\epsilon_k^2 + \Delta^2} \quad (2.1)$$

where  $\epsilon_k$  is the electron's *kinetic energy*. At zero temperature the following condition holds:

$$E_k \leq \epsilon_F \rightarrow \epsilon_k \leq \pm \sqrt{\epsilon_F^2 - \Delta^2} \quad (2.2)$$

indicating that single electrons cannot occupy this energy band, only Cooper pairs can exist within it.

Using BCS theory, one can analyze how the energy gap varies as the temperature increases. As shown in figure (2.3) the gap remains nearly constant up to  $T \sim 0.4T_C$ . Beyond this point, it begins to decrease, ultimately reaching zero at  $T = T_C$ .

Observing the behavior of the energy gap with respect to temperature, one can compute a theoretical value of the critical temperature, given by:

$$k_b T_C = 1.13 \hbar \omega_c \times e^{-1/N(0)V_0} \quad (2.3)$$

where  $N(0)$  is the electron density of states evaluated at  $T = 0$ , while  $V_0$  is the coupling potential between electrons, and  $\hbar \omega_c$  is the energy associated with the phonons frequency

Again, according to the BCS theory [17, 18], when a Cooper pair appears, it is characterized by an energy of  $3.53 k_B T_C$ . This energy can be compared to the forbidden energy gap of electrons, leading to the identification of an important dimensionless quantity:

$$\frac{2\Delta}{k_b T_C} = 3.53 \quad (2.4)$$

This parameter is independent of the system's degrees of freedom and remains valid under the assumption of weak electron-phonon coupling, which is a fundamental premise of BCS theory.

## 2.3 Classification of superconductors

There exists no perfect classification for superconductors. However, they can be categorized based on their intrinsic behavior under an applied field (e.g., Type I and Type II superconductors) or according to the theoretical framework they follow (e.g., conventional and unconventional superconductors).

### 2.3.1 Type I/II superconductors

The superconducting state can be perturbed—and ultimately destroyed—by the application of an external magnetic field. Based on their behavior under such conditions, superconductors are categorized into two types: type I superconductors remain in their superconducting phase as long as the external magnetic field does not exceed a specific threshold, known as the critical field  $H_C(T)$ , which generally depends on the temperature. When  $H_{\text{ext}} < H_C(T)$  and  $T < T_C$ , the material

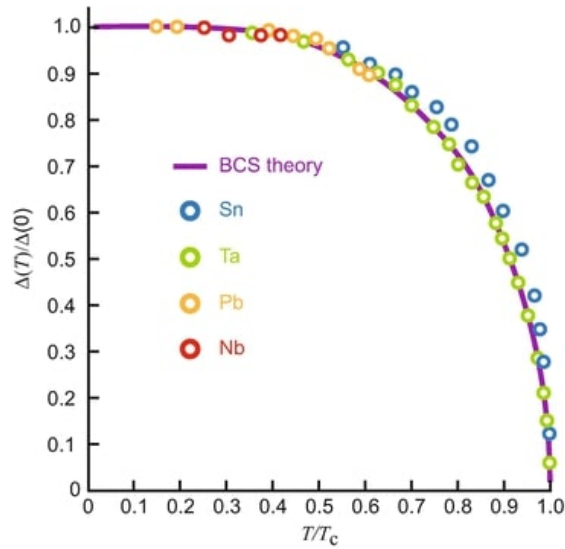


**Figure 2.3:** Illustrates the behavior of the superconducting gap, normalized to its value at  $T = 0$ . On the horizontal axis, the reduced temperature ( $T/T_C$ ) is plotted. The graph compares theoretical results with experimental data from various conventional superconducting materials. Reprinted from [22].

exhibits complete expulsion of any magnetic field from its bulk (the Meissner effect) and remains in its superconducting state. However, when the external field exceeds the critical threshold, a phase transition occurs, and the material reverts to its normal state (fig: 2.4 left).

Type II superconductors exhibit a fundamentally different magnetic behavior and constitute most superconductors discovered to date. They generally possess higher critical temperatures and are characterized by two distinct critical magnetic field values,  $H_{C1} < H_{C2}$ , as shown in figure 2.4 right.

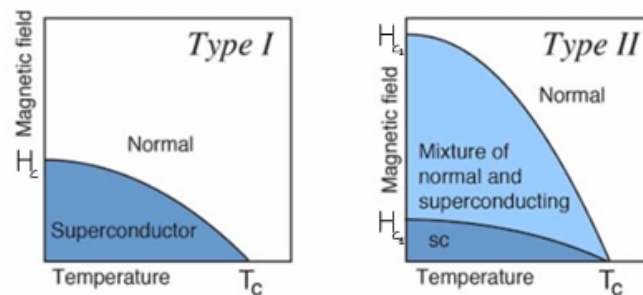


**Figure 2.4:** On the left we see the pictorial phase transition characterizing the type I superconductors in terms of external field and temperature; on the right the phase diagram related to the type II superconductors. Reprinted from [23].

When the external applied field  $H_{\text{ext}}$  is lower than  $H_{C1}$ , type II superconductors behave similarly to type I, demonstrating the Meissner effect. However, as soon as  $H_{\text{ext}}$  increases beyond  $H_{C1}$  and enters the interval  $H_{C1} < H_{\text{ext}} < H_{C2}$ , the magnetic field begins to penetrate the material in a specific manner [24, 25]. In this regime, the magnetic field enters the material in a grid-like arrangement, forming vertical vortices of magnetic flux. Within the vortex cores, the material transitions to its normal state, while the surrounding regions remain in the superconducting phase, allowing a supercurrent (a current with zero resistance) to flow. These vortices create localized magnetic fields that are quantized, corresponding to a quantum particle called a fluxon, associated with a quantum flux value of  $2.07 \times 10^{-15}$  Wb. This arrangement forms the well-known Abrikosov lattice [24, 25], as shown in 2.5.

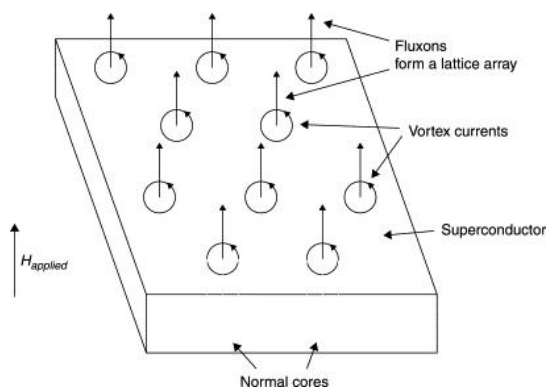


**Figure 2.5:** Diagrammatic representation of the vortices that appear in type II superconductors. Reprinted from [26].

When  $H_{\text{ext}} > H_{C2}$ , superconductivity is completely destroyed, even at temperatures below  $T < T_C$ . At this point, the vortices become densely packed, and their cores overlap, leading the entire material to transition to the normal state.

### 2.3.2 Conventional and unconventional superconductors

Superconductors can also be classified based on the theoretical framework they belong. Conventional Superconductors are well-described by the BCS theory, which assumes weak electron-phonon coupling as the primary mechanism for superconductivity. On the other hand, unconventional superconductors are materials that deviate from the BCS framework and are characterized by alternative interaction mechanisms, such as electron-electron interaction. Most known superconductors fall into this category. Examples include high- $T_C$  cuprates and Fe-based superconductors, which are the focus of this discussion.

### 2.3.3 High/Low $T_C$ superconductors

The critical temperature ( $T_C$ ) is a key parameter used to classify superconductors into two families: **low-temperature superconductors (LTS)** and **high-temperature superconductors (HTS)**. However, the distinction is not so rigorous and it depends on the kind of material we deal with. Generally speaking, we can put the threshold at  $T \sim 30$  K even if some materials are listed as high temperature one but their critical temperature it's lower than 30 K.

This distinction is particularly important from an operational perspective, as the choice of refrigeration system depends on the  $T_C$  of the material. For HTS, liquid nitrogen, with a boiling temperature of 77 K, is sufficient. It is less expensive and easier to handle. However, for LTS, liquid helium is required due to its significantly lower boiling point ( $T_{\text{boiling}} = 4$  K), making it much more costly and difficult to produce. Nevertheless, in recent year the crucial choice is not on the refrigerant liquid, because most of the refrigeration systems are a closed cycle ones. Therefore, is better to focus on which kind of cycle we need to use, such that a pulse-tube cryocooler.

### 2.3.4 Topological superconductors

Shapes in nature can be described and classified using a mathematical concept known as topology. For instance, if two shapes can be deformed one into the other this means that they belong to the same topological class.

This concept can be extended also for a quantum mechanical wavefunction. In fact, we say that two different wavefunctions adiabatically connected can be referred to as topological identical. However, when we do not consider the atomic limit of the wavefunction, the system described by such wave function can be treated as topological non-trivial system. Indeed, topological classifications are possible, theoretically speaking, for different quantum many-body systems characterized by a gap in the energy-band spectrum to protect the occupied states.

The first quantum mechanical system signaled as topological was the quantum Hall system which adiabatic continuity can be described by an integer number called Chern number [27]. Topological materials have gained significant attention in the past decade due to their ability to exhibit unique phenomena arising from various topological phases.

Therefore, the topological phases are characterized by a symmetry constraint. Systems hosting topology without symmetry are intrinsic topological ordered with a long-range entangled whereas the systems defined by a symmetry constraint are short-range entangled. The latter can be classified as topologically trivial or symmetry-protected topological phases (SPT). Moreover, this can be divided into noninteracting and interacting phase, depending on the strength of electron-electron

interaction [28]. Therefore, these phases have paved the way for groundbreaking applications already demonstrated at the laboratory scale. Notable examples include: the quantum spin Hall effect [29, 30], quantum anomalous Hall effect [31, 32], topological dipoles for next-generation photovoltaic and photodetectors [33, 34], high-efficiency thermoelectric [35, 36], energy conversion and storage processes [37]. Among topological materials, topological superconductors (TSCs) are particularly noteworthy because they can host Majorana bound states (MBSs), also known as Majorana zero modes (MZMs). These states are of great interest as potential qubits for topological quantum computation.

To better understand the fundamental concepts behind topological superconductivity (TSC), we need to introduce some key symmetry properties.

First, **time-reversal symmetry (TRS)** is a property of a system that remains unchanged when the direction of time is reversed. The only difference in this transformation is that some observables, such as velocity, change direction. However, certain systems break this symmetry, meaning their description under time reversal is non-trivial. A notable example is a **ferromagnet**, where the magnetic moments do not remain invariant under time reversal, leading to TRS breaking.

Another important symmetry is **chiral symmetry**, an intrinsic property of condensed matter systems. This type of symmetry distinguishes between right-handed and left-handed configurations of a system, playing a crucial role in the classification of topological phases.

Superconductors, in general, are characterized by strong electron-electron interactions. By applying a mean-field theoretical approach, these interactions are approximated as an effective potential. TSCs belong to the class of symmetry-protected topological (SPT) phases, similar to topological insulators.

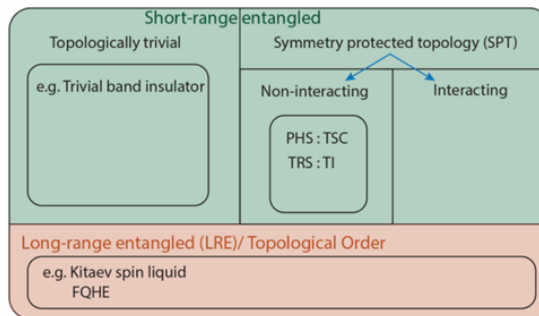


**Figure 2.6:** Classification of gapped topological phases of matter on the associated TSC classes. Reprinted from [28].

In particular, there are at least four subcategories that belong to the superconducting (SC) and superfluid *Bogoliubov de Gennes* (BdG) symmetry family. While it is not entirely correct to categorize this family as purely superconducting, since

the topological insulator (TI) family can also host fully gapped quasiparticles similar to superconductors, it is useful for understanding the broader context. Within this group, we find class D, which breaks time-reversal symmetry and can host 1D *p-wave* topological superconductors (TSC) and 2D *p+ip* TSCs. Other families also exist, such as class DIII, which contains two chiral *p-wave* superconductors with opposite chirality in 1D.

Majorana fermions can emerge in a topological superconductor (TSC) because they are linked to the electrons pairing, that can support such edge states. In conventional metals and insulators, a quasiparticle carries a specific electrical charge, while its antiparticle is the same particle but with the opposite charge. A superconductor provides an ideal environment for the emergence of Majorana fermions due to particle-hole symmetry. However, this is not true for all superconductors. Conventional superconductors are not favorable hosts for Majorana fermions because the quasiparticle, formed from the superposition of an electron and hole, involves opposite spins and cannot be its own antiparticle, which is crucial for the definition of Majorana bound states. In this case, we would have an antiquasiparticle where the electron and hole have opposite spins. This observation makes the *chiral p-wave* and *p+ip* pairing superconductors (1D and 2D, respectively) the natural candidates for hosting Majorana fermions. However, these are not the only possible systems: experimental evidence also suggests that the DIII class in 3D can exhibit 2D Majorana fermion modes.

### 2.3.5 Majorana fermions and topological superconductivity

Topological superconductors (TSCs) are considered to be the most promising platform for exhibiting Majorana fermions. In 1929, Paul Dirac derived the equation for the relativistic motion of electrons, now known as the Dirac equation. This theory predicted that for every fermion, there exists an antiparticle differing only in charge sign. This theoretical prediction was confirmed experimentally in 1934 when Anderson discovered the positron—a particle with the same mass as the electron but opposite charge. Building on this, Ettore Majorana predicted the existence of particles that are their own antiparticles [38]. He noted that the complex conjugate of a wave function satisfying the Dirac equation also satisfies the same equation. If the wave function is real, it becomes self-conjugate, indicating the existence of particles indistinguishable from their antiparticles—Majorana particles. These particles obey Fermi-Dirac statistics and are thus also referred to as Majorana fermions.

Following this theoretical prediction, physicists sought to identify particles that could meet the criteria to be their own antiparticles. Among known particles, only neutrinos are hypothesized to satisfy these conditions. However, superconducting

topological materials have emerged as a potential host for Majorana fermions. This idea is supported by two key observations: topological non-trivial surface states in TSCs can host gapless excitations that follow the relativistic Dirac equation; The superconducting phase itself facilitates the necessary conditions. In TSCs, a superposition of electron and hole excitations occurs, enabling them to behave as neutral particles that can act as their own antiparticles [39] (fig. 2.7)

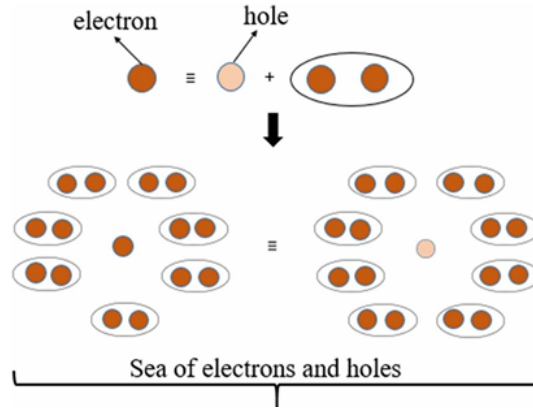


**Figure 2.7:** A pictorial representation of how Majorana fermions emerge from the interaction of electrons and holes with Cooper pairs, rendering electrons and holes indistinguishable. Reprinted from [39].

### 2.3.6 Signature of Majorana Fermions in TSCs

The existence of Majorana fermions in TSCs can be demonstrated through several key phenomena, briefly described below [40]:

- **Zero bias conductance peak (ZBCP):** TSCs are expected to exhibit bulk superconductivity with topologically non-trivial surface states or gapless surface states. These can be probed using point-contact spectroscopy measurements, which serve as a preliminary check to determine whether the conducting surface states of a TSC can host Majorana modes. The presence of Majorana fermions in conducting surface states significantly affects the conductance between the normal metallic and superconducting states, often producing a peak in the conductance spectra at zero bias. This arises from the tunneling of electrons [41, 42, 43]. However, the observation of a ZBCP alone is insufficient to confirm the presence of Majorana fermions. Other phenomena, such as heating effects at the contact [44] or magnetic scattering [45] can also produce similar peaks.
- **Quantized thermal conductivity:** Majorana fermions are associated with

a phenomenon known as the thermal quantum Hall effect [27]. In a topological superconductor, the bulk remains thermally insulating, and Majorana bound states are too localized to carry heat. Consequently, heat conduction occurs only via surface states. Similar to the quantum Hall effect (QHE), the thermal quantum Hall effect features quantized heat conduction. The quantization unit for this effect is given by  $\frac{1}{3}(k_b/e)^2 T e^2/h$ , where  $T$  is the temperature and  $\frac{1}{3}(k_b/e)^2$  is known as the Lorentz number [46].

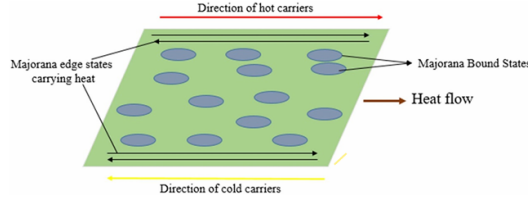


**Figure 2.8:** *The image shows the behavior of the Majorana fermions involved in the heat conduction. Reprinted from [46].*

- **Anomalous Josephson effect:** An important feature linked to the presence of Majorana Fermions is the anomalous Josephson effect. This effect differs from the zero bias conductance peak (ZBCP) in that the tunneling process involves Cooper pairs rather than individual electrons. In the anomalous Josephson effect, tunneling occurs between two TSCs (topological superconductors). When a Cooper pair tunnels from one TSC to the other, passing through Majorana bound states (MBSs), it causes a phase shift between the voltage and the current from  $2\pi$  to  $4\pi$ . This results in a fractional Josephson effect, which is also known as the anomalous Josephson effect [47].

## 2.4 Fe-based superconductors

### 2.4.1 General information about Fe-based superconductors

In 2001, it was discovered that metallic iron exhibits a superconducting phase transition when subjected to high hydrostatic pressure, leading to a transition temperature of 2 K [48].

This finding was quite significant because, according to the BCS theory, Cooper pairs are formed by two electrons occupying the same state and having opposite spins, which satisfy the Pauli exclusion principle. However, iron typically has non-zero magnetic moment, which imposes a ferromagnetic order of spins, forcing the electrons to have parallel spins, thus preventing the formation of conventional spin-singlet Cooper pairs and superconductivity. The transition to a superconducting

state under pressure occurs because pressure changes iron's atomic structure from body-centered cubic *bcc* to hexagonal close-packed *hcp* (fig:2.9). In the *hcp* structure, the spins are not forced into any particular order, allowing the transition to a superconducting phase.

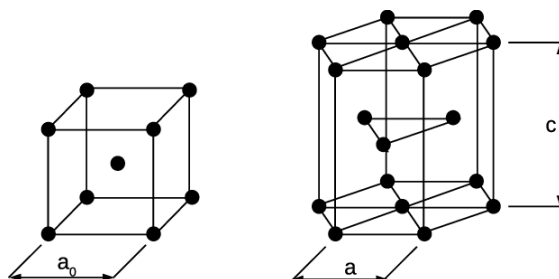


**Figure 2.9:** The *bcc* (body-centered cubic) atomic structure on the left, and the *hcp* (hexagonal close-packed) structure on the right.

This discovery was remarkable because it challenged the belief that magnetism inherently conflicts with superconductivity. In 2008, a new family of superconductors, known as Fe-based superconductors, was discovered. These materials do not require external pressure to exhibit superconductivity and show a relatively high critical temperature, competing with the cuprates. For instance, *LaFeAsO* doped with *fluorine*(*F*) exhibits a superconductive phase transition with  $T_C = 26$  K [49], which sparked interest in the search for higher-temperature superconductors.

## 2.4.2 Fe-compounds structure

The discovery of Fe-based superconductors led to the identification of several families of these materials. These compounds can be grouped according to their structural characteristics (fig: 2.10)

- **family "11"**: in this family we associate the model compound *FeSe*;
- **family "111"**: where the general formula is given by  $MFeAs$ , with *M* which states for an *alkali metal*;
- **family "122"**: symbolized by  $MFe_2As_2$  where, this time, *M* stand for *alkalin earth metals*;
- **family "1111"**: denoted by the formula  $ReFeAsO$  and *Re* corresponding to *rare-earth metals*;
- **families "1144" and "12442"**: these two groups have been synthesized only in 2016 and present important differences with respect the previous one, such as the atomic structure and the magnetic order characterizing the compounds;

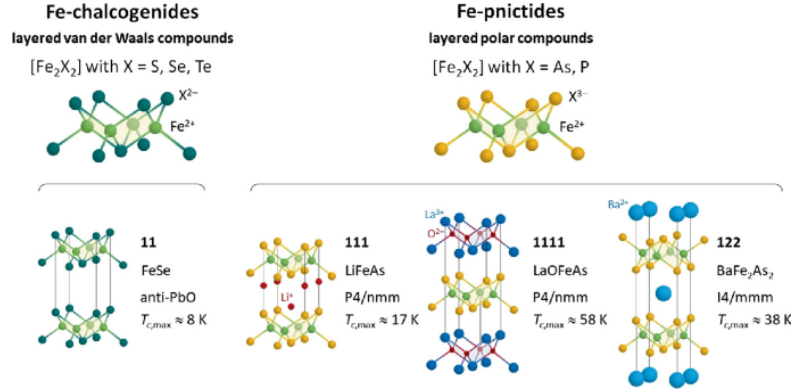


**Figure 2.10:** Schematic representation of different Fe-based families, highlighting structural differences. Reprinted from [50].

There exists a common link between all these families, which is the layered structure formed by iron (Fe) atoms that bond with other elements. Specifically, there are two possibilities for the bonding: the first is with a **pnictogen** (such as P or As), and the second is with a **chalcogen** (from group VI-A of the periodic table, e.g., Se or Te). These compounds are commonly known as iron-chalcogenide superconductors, which serve as the focus of this thesis work, since  $Fe(Se, Te)$  belongs to this family [49].

In all these compounds, the Fe atoms are positioned in such a way that they occupy the center of the unit cell, while the pnictogen or chalcogen atoms occupy the vertices of the tetrahedron. What is crucial here is the arrangement of the Fe-layers, where the other atoms are directed upwards or downwards, but not within the same plane as the Fe-layer. This arrangement highlights the importance of the crystallographic parameters of these compounds, as they play a crucial role in their superconducting phase transition.

In particular, the intermediate layers that characterize these materials are key to understanding their superconducting behavior. While Fe is electrically conductive, any other element in the mid-layers (whether pnictogen or chalcogen) is insulating. Furthermore, the distance between the layers varies among different families, governed by the  $c$  parameter in the atomic structure, underscoring the importance of these crystallographic parameters. Studies have shown that the value of the  $c$  parameter significantly affects the critical temperature, suggesting a connection between the superconducting phase transition and the atomic structure of Fe-based materials [51].

### 2.4.3 Unconventional superconducting coupling

It is well-known that the key to the superconducting phase transition lies in the formation of Cooper pairs, typically driven by electron-phonon coupling. However, this mechanism does not apply to Fe-based superconductors, where the interaction is much weaker. Therefore, another explanation is needed for the appearance of the superconducting phase in these materials. Generally, Fe-based compounds need to be doped with elements, as previously mentioned in section 2.4.2, to achieve the phase transition. In their undoped state, the antiferromagnetic order imposed by iron conflicts with superconductivity. This manifests through spin density waves (SDW), which create alternating parallel and anti-parallel spins. The introduction of other atoms disrupts this ordering, pushing the system into a disordered, unstable state affected by fluctuations [52, 53].

In the case of Fe-based superconductors, spin fluctuations are likely responsible for electron pairing. These fluctuations induce an oscillating potential in real space, which attracts electrons, causing them to form Cooper pairs and thus facilitating the superconducting phase transition.

### 2.4.4 Fermi surface structure

The atomic structure of Fe-based compounds has significant implications for their physical properties. One of the most important influences is the shape of the Fermi surface. The Fermi surface is defined in the reciprocal lattice, starting from the real space lattice, with coordinates given by the wavevector  $\mathbf{k}$ , which describes the energy (and hence the momentum) of the electrons. Each electron is described by a three-component vector  $\mathbf{k} = (k_x, k_y, k_z)$  corresponding to a specific energy. Electrons with the same energy occupy a confined region that forms the surface known as the Fermi surface. When the temperature  $T=0$ , electrons occupy energy states below the Fermi level, and the Fermi surface approaches a spherical shape. The radius of this sphere is given by:

$$|k_f| = \sqrt{\frac{2m_e\epsilon_F}{\hbar^2}} \quad (2.5)$$

where  $m_e$  is the electron mass and  $\epsilon_F$  the Fermi level. Electrons occupy the states inside the sphere, corresponding to energy levels below the Fermi one (fig. 2.11).

When considering more complex structures, the shape of the Fermi surface begins to change as well. An example of this is seen in Cu-based superconductors, where the carriers are confined between the copper and oxygen planes. This confinement influences the shape of the Fermi surface, making it no longer spherical but instead acquiring a cylindrical shape. This is a common feature in materials exhibiting a

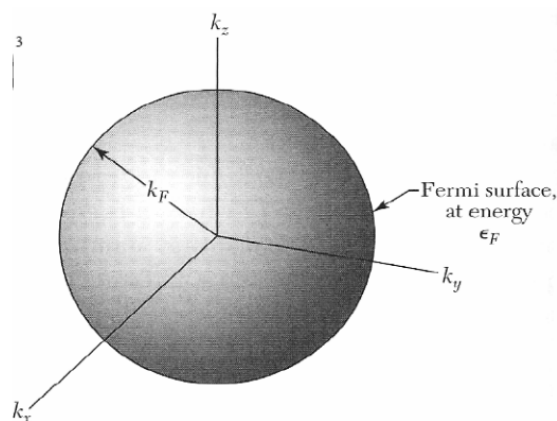


**Figure 2.11:** *Simplified view of the spherical Fermi surface of monovalent metals. Reprinted from [54].*

layered structure, which are typically characterized by a cylindrical Fermi surface. However, unlike the cuprates, Fe-based superconductors are described by a Fermi surface that lacks perfect two-dimensionality. As a result, there is a deformation of the cylindrical shape, which is clearly visible in the figure (2.12) [55].

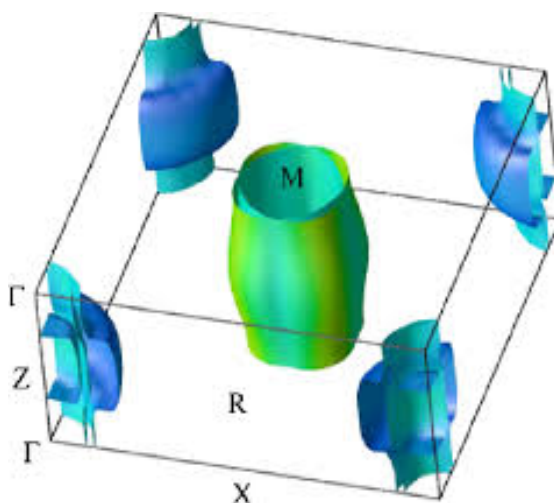


**Figure 2.12:** *3D reconstruction of the Fermi surface in LaFeASO. In the figure, the holonic Fermi surfaces near the corners are related to the  $\Gamma$ -point (associated with holes), while the central group corresponds to the M-point (associated with electrons). Reprinted from [56]*

### 2.4.5 Multiband character of superconductors

In condensed matter physics, the concepts of the Fermi surface and electron bands are closely related. Typically, superconductors are described by a single energy band that crosses the Fermi surface, leading to a unique and continuous Fermi surface. In this case, the material can exhibit a single energy gap or a continuous distribution of gaps, which are referred to as isotropic and anisotropic gap conditions, respectively.

However, superconducting materials can also have an electronic structure characterized by multiple energy bands. These bands arise from the superposition of atomic orbitals that cross the Fermi level, creating distinct sheets of the Fermi surface. Since the system has separate Fermi surfaces and multiple bands contributing to conduction, the superconductor may exhibit different energy gap values, which can sometimes coincide. For example, in a two-band system, to break a Cooper pair in band 1, an energy of  $2\Delta_1$  is required, while in band 2, an energy of  $2\Delta_2$  is needed. The behavior of multiband superconductors is often explained by an approximate solution to the BCS equations, though these are not always entirely accurate. A more suitable model is the Shul and Matthias model [57]. In this context, the superconducting phase transition is related to couplings within the same band. Consequently, the material will exhibit different critical temperatures ( $T_C$ ) for each energy gap. On the other hand, coupling between different bands results in separate gaps that share the same critical temperature.

### 2.4.6 Nesting of Fermi surfaces

Most Fe-based superconductors must be doped to enter the superconducting phase. In their pure state, these materials exhibit an antiferromagnetic (AFM) order, which is typically realized through a *spin density wave* (SDW). In real space, the modulation associated with the SDW occurs over a length scale denoted by  $\lambda$ , which corresponds to a wave vector in the reciprocal lattice,  $q = 2\pi/\lambda$ . The wave vector  $\mathbf{q}$  can connect the  $\Gamma$  point to the M point, leading to the phenomenon of **nesting** of the Fermi surface.

We have observed that superconductivity in iron-based materials can be achieved through partial substitution of Fe atoms with appropriate elements, leading to the formation of *chalcogenides* and *pnictogenides*. This substitution suppresses the ferromagnetic order, perturbing the spin ordering and thereby allowing band coupling. The nesting of the Fermi surfaces corresponds to a competition between antiferromagnetic (AFM) and superconducting behaviors. This implies that the doping effect, which impacts the antiferromagnetic order, also influences the Fermi surfaces. In fact, as the AFM ordering is perturbed and eventually overtaken by the superconducting phase, the nesting effect disappears. This occurs because doping can introduce either negative or positive carriers, which in turn modify the band structure. These modifications change the cylindrical sheets of the holonic and

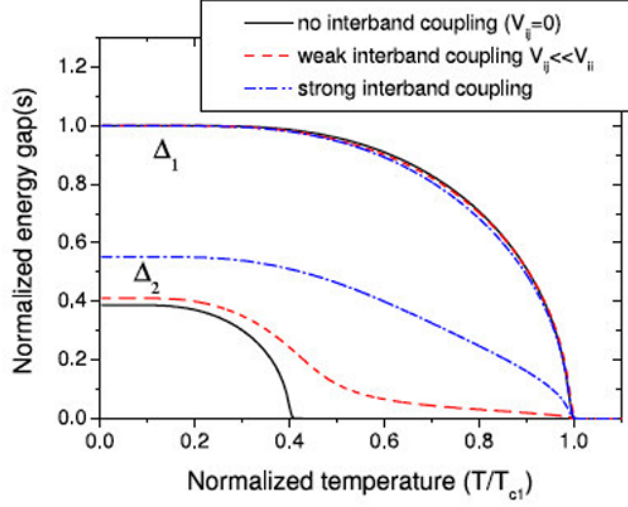


**Figure 2.13:** The figure shows how the gaps, corresponding to different bands, behave with respect to the reduced temperature  $T/T_C$ , following the Shul and Matthias model. It can be observed that the gaps vanish at different critical temperatures, which depend on the strength of the intraband coupling. The case of weak interband coupling is represented by the red dashed line, while strong interband coupling is shown by the blue dashed line, exhibiting a tail as  $T \rightarrow T_C$ . Reprinted from [57]

electronic Fermi surface, making the translation via the wave vector  $\mathbf{q}$  impossible. As a result, nesting no longer occurs [58].

However, there is no direct one-to-one correspondence between the nesting phenomenon and the superconducting phase transition. In iron-based superconductors, the key to the transition lies in the inter-band coupling.

### 2.4.7 Superconductive band coupling

The mediator effect that enables the superconducting phase transition in iron-based superconductors is driven by fluctuations in the spin ordering and the defects introduced by doping the compound. These defects act as an oscillatory attractive potential for the carriers. In the reciprocal lattice, this effect is mapped into a change in the sign of the superconducting gaps,  $\Delta(\mathbf{k})$ , when transitioning from one point on the Fermi surface to another translated by the wave vector  $\mathbf{q}$ . This results in the coupling between the holonic bands and the electronic ones. For example, this occurs when  $\Delta(\mathbf{k})$  is positive on the cylinder at the  $\Gamma$  point and negative in the vicinity of the M point, with the gap changing signs as it is translated by the

wave vector  $\mathbf{q}$ , which governs the spin ordering of the system.

Iron-based superconductors are characterized by a multiband structure, which can cross the Fermi level, thereby contributing to the conduction of electrons. This leads to stronger inter-band coupling, characterized by different gap values, each of which vanishes at a critical temperature that is unique to each gap.

### 2.4.8 Analysis of structural parameters

Iron-based superconductors are very peculiar because their superconducting behavior arises from several interrelated features, including the atomic lattice and reciprocal space. The atomic structure plays a fundamental role in shaping these properties. Specifically, Fe-based superconductors are characterized by a layered structure, where Fe atoms occupy distinct planes from the substituted atoms. Recent studies have shown that the critical temperature ( $T_C$ ) is influenced by the parameter  $c$  of the atomic lattice. It has been observed that when  $c$  increases,  $T_C$  tends to decrease. Therefore, research efforts have been devoted to on reducing this  $c$ -parameter to reach higher critical temperatures, ultimately paving the way for room-temperature superconductivity [51].

To decrease  $c$ , one can focus on doping atoms that occupy the intermediate layers between the Fe-planes. This approach aims to minimize the distance between these planes, directly linked to the parameter  $c$ . The vertical distance between layers depends on two factors: first, the intrinsic size of the atoms—the larger the atomic number, the greater the space required between the layers; and second, the interaction between the pnictogen (or chalcogen) atom, the Fe atom, and the other elements forming the insulating layers. If the interaction is stronger, the distance between the planes becomes shorter, reducing  $c$  and thereby increasing the critical temperature.

Fe-As compounds are a good example to better understand this feature. In this case, the Fe atoms are substituted by As, and the distance between Fe and As atoms, along with the angle of the Fe-As-Fe bond, are key parameters. Experimental results show that the optimal values of these two degrees of freedom for maximum  $T_C$  occur at an angle of  $109.5^\circ$  and a distance of 1.38 [51]. However, this behavior is not universal, as in some intercalated *FeSe* compounds, the critical temperature increases along with the interlayer spacing.

## Chapter 3

# Properties of the $Fe(Se, Te)$ superconductors

### 3.1 General features of $FeSe$ related superconductors

The discovery of iron-based superconductivity marks a significant advancement in solid-state physics, with a profound impact on the study of high-temperature superconductivity [59, 60]. Based on their structural configurations, these materials can be classified into several families, each exhibiting a range of unique physical phenomena, such as multi-band structures, extremely low Fermi energy, and the presence of nematic and antiferromagnetic (AFM) ordered states. These unconventional properties make them strong candidates for high-temperature superconductors, a primary focus of research in recent years [61, 62, 63]. Furthermore, the superconducting phase transition in these materials cannot be explained by conventional electron-phonon coupling, suggesting that cuprates are no longer the sole compounds exhibiting high  $T_C$  values. This shift in perspective has redirected attention toward understanding the behavior of Fe-based compounds [64, 65, 66].

The **iron-chalcogenide** compounds belong to the *family "11"* of the iron-based superconductors. They have the advantage of a very simple crystal structure and non-toxicity (in contrast to FeAs-based compounds). Similar to cuprates, iron-based superconductors exhibit a quasi-two-dimensional crystal structure. Notably, the FeCh layer (where Ch can be S, Se, or Te, for instance) plays a crucial role, as experimental evidence shows that it significantly affects the superconducting properties of these materials. Furthermore, the Fe layer is *sandwiched* between two Ch layers, which induces a folding of the corresponding electronic structure (see fig. 3.1).

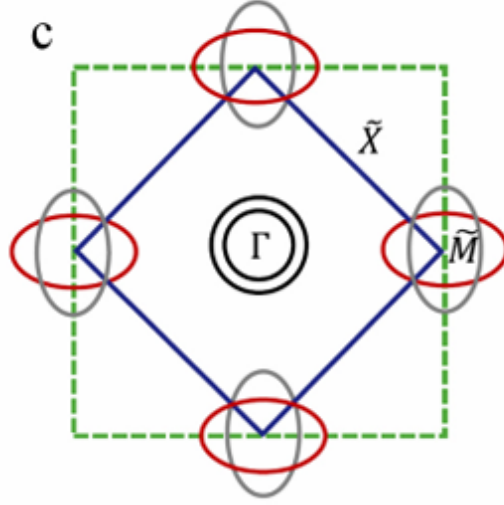


**Figure 3.1:** Fermi sheets in the folded Brillouin Zone, whose boundaries are the represented by solid blue line. Reprinted from [67].

Among all the iron-based superconductors,  $FeSe$  and its related systems have attracted particular interest due to their unique properties.

### 3.1.1 Iron-selenide ( $FeSe$ )

The  $FeSe$  superconductor has a simple crystal structure consisting of  $FeSe$  layers, where the Se atoms do not lie in the same plane as the Fe atoms. This simplicity makes  $FeSe$  an ideal candidate for theoretical studies on the mechanism of superconductivity.

Bulk  $FeSe$ , with a superconducting transition temperature ( $T_C$ ) of 8 K, was discovered in 2008 and crystallizes in the tetragonal  $\beta - FeSe$  phase, which adopts a PbO-type structure at ambient pressure [68] (fig. 3.2). Experimental evidence indicates that excess Fe is crucial for stabilizing the crystal structure of  $Fe_{1+\delta}Se$ , and the superconducting phase transition is highly sensitive to the stoichiometry ( $\delta$ ) [4].

Moreover, the critical temperature ( $T_C$ ) can be enhanced by applying pressure: under *high pressure* ( $\sim$  GPa),  $T_C$  increases to 36.7 K [70], enabling the emergence of a new magnetic order while suppressing the nematic one. However,  $FeSe$  undergoes a structural transition from the tetragonal to the orthorhombic phase at 90 K, which is not accompanied by any magnetic transition. This transition results in superconductivity only in the orthorhombic phase, with  $T_C = 12$  K [70, 71, 72, 73] (fig. 3.3).

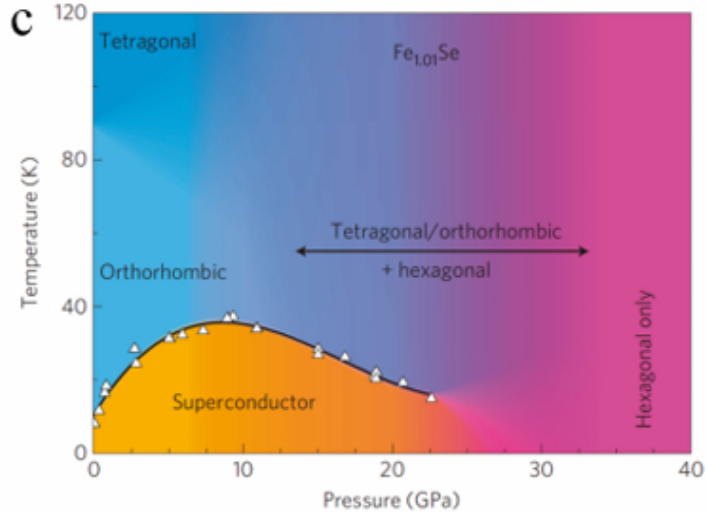


**Figure 3.2:** Phase diagram of  $Fe_{1.01}Se$  as function of pressure. Reprinted from [69].

Chemical methods, such as intercalation or ionic liquid gating, can also be employed to raise the critical temperature without applying high pressure, achieving  $T_C = 44$  K.

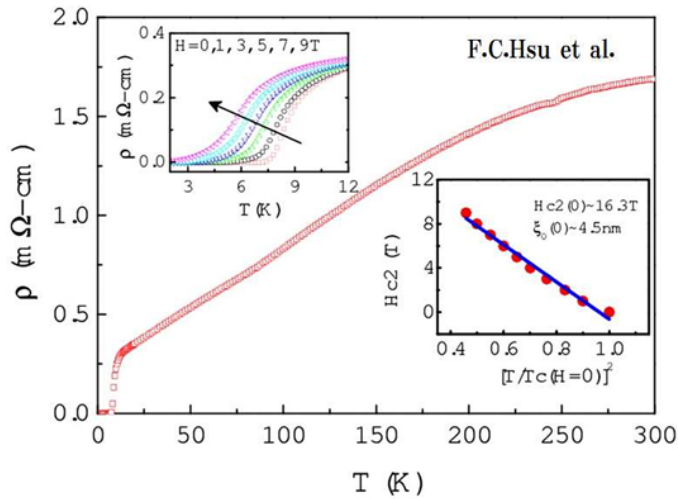


**Figure 3.3:** Temperature dependence of resistivity for  $FeSe$ . The upper inset shows the behavior of resistivity with respect to temperature under high magnetic fields. Reprinted from [68].

This feature uniquely characterizes  $FeSe$  compared to its counterparts, as the orthorhombic transition in similar compounds is typically accompanied by a magnetic transition. In contrast, in  $FeSe$ , spin fluctuations suppress the antiferromagnetic (AFM) character of the compound and are enhanced under the application of high pressure.

The band structure and Fermi surface of the  $FeSe$  superconductor (fig. 3.4) exhibit behavior analogous to other iron-based superconductors. They are characterized by low-energy electronic states, with two hole-like Fermi surface sheets at the zone center and two electron-like Fermi surface sheets around the corners. Angle-resolved photoemission spectroscopy (**ARPES**) can be performed to gain insights into the unique properties of this compound, enabling key observations [74, 75, 76].

First, at low temperatures below the structural transition, the  $\Gamma$  point is dominated by two hole-like bands, while near the M point, an electron-like band crossing the Fermi level and a hole-like band at higher energy are observed. These findings are consistent with quantum oscillation and **scanning tunneling microscope (STM)** measurements [77, 78, 79].

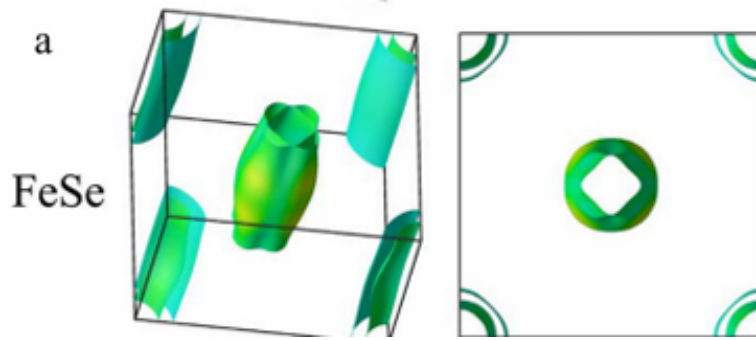


**Figure 3.4:** Fermi surface of the bulk  $FeSe$  through calculations. Reprinted from [80].

### 3.1.2 Iron-telluride (FeTe)

The FeTe compound, which is similar to  $FeSe$ , exhibits quite different behaviors. In fact, it does not undergo a superconducting phase transition but instead shows a structural/magnetic transition at  $T_{MS} = 70$  K [81, 82]. Above this temperature threshold, it behaves like a semiconductor, while below 70 K, it assumes a metallic behavior. Moreover, FeTe is not superconducting except in the special case of tensile-stressed thin films, where a phase transition occurs at  $T_C = 13$  K [83]. From the reciprocal lattice perspective, some ARPES measurements reveal a pair of nearly electron-hole compensated Fermi pockets, strong Fermi velocity renormalization,

and the absence of SDW gaps, which contrasts with the  $FeSe$  case, where the SDW phase actually appears, allowing for the occurrence of a superconducting phase transition [84].

The measured electronic structure of FeTe is quite similar to that of other iron-chalcogenides, except for the antiferromagnetic structure, which is rotated by 45 degrees in FeTe. This is in agreement with the Fermi surface nesting picture for the formation of spin-density wave (SDW) below  $T_{MS}$ . Above the magnetic transition critical point, the spectral weight is concentrated near the  $\Gamma$  and M points. The  $\Gamma$  point is dominated by two hole-like bands, while two electron-like bands are observed near the M point. As the temperature is lowered below  $T_{MS}$ , the spectral weight distribution changes: the distribution around M is suppressed, meaning the spectral weight shifts from low binding energy to high binding energy [85] (fig. 3.5).

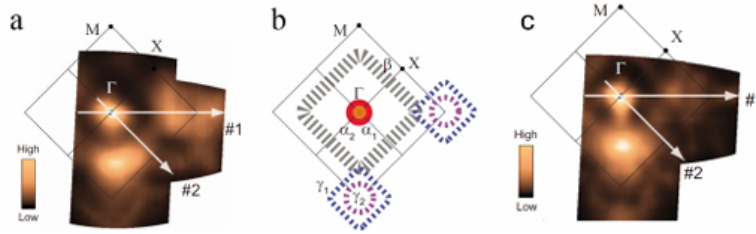


**Figure 3.5:** (a) Fermi surface of  $Fe_{1.06}Te$  at  $T = 135$  K; (b) Spectral weight distribution around  $E_F$ ; (c) Fermi surface of  $Fe_{1.06}Te$  at  $T = 15$  K. Reprinted from [86]

The ARPES measurements show a temperature-dependent change, revealing a coherent quasiparticle peak near the Fermi level below  $T_{MS}$ , along with a hump structure displaced to higher energy, featuring a dip between these two structures. The *peak* behavior is similar to what is observed in manganites and doped cuprates, which can be explained by polaron formation, while the hump feature is interpreted as an incoherent excitation of electrons strongly coupled to bosons. Indeed, the quasiparticle is associated with coherent polar motion, which, at low temperatures, may explain the metallic transport observed in the SDW state [87].

## 3.2 Iron-selenide-telluride ( $Fe(Se,Te)$ )

Finally, by partially substituting Se atoms with Te within the same lattice, we obtain a new compound described by the minimal formula  $Fe(Se,Te)$ . An enhancement of the critical temperature is then observed, reaching  $T_C = 15$  K in the bulk and 23 K in thin films [5, 6].

Moreover,  $Fe(Se, Te)$  is also predicted to possess **topologically protected Dirac surface states**, which could be a key point for the next generation of topological quantum computing [88, 89, 90].

An important challenge in the synthesized  $Fe(Se, Te)$  **superconductor** is the nonstoichiometric atomic ratios, with excess Fe atoms spontaneously occupying the interstitial sites. Usually, a different labeling is used for the formula that takes into account the relative abundance of the different atomic components:  $Fe_{1+\delta}Se_{1-x}Te_x$  (where  $x = 0 \div 1.0$ ) [91]. The extra Fe atoms are related to **local magnetic moments** that affect the system through a **strong pair-breaking effect**, suppressing the appearance of bulk superconductivity. This suggests that one should work to eliminate this excess in order to access and maximize the superconducting phase transition. The process can be carried out in several ways that are applied during crystal growth, such as electrochemical deintercalation or acid etching.

### 3.2.1 Te-substitution effect on $FeSe$ compound

Following the discovery of  $FeSe$ , it was natural to ask whether chemical substitution, either at the Se or Fe site, could change the properties of the compound. Indeed, the substitution of Te has important experimental evidence.

It was found that the superconducting transition temperature increases with Te doping ( $x$  in  $Fe(Se_{1-x}Te_x)$ ), reaching its maximum value for  $x = 0.5$ , and then decreases with further Te doping. In fact, we know that the FeTe compound is non-superconducting.

For the  $FeSe$  material, a structural transformation from tetragonal symmetry to triclinic symmetry occurs at  $T = 105$  K, which changes the lattice parameters without breaking magnetic symmetry. This transformation is strongly connected with the appearance of superconducting character. The Te substitution confirms that the low-temperature structural deformation is crucial to the competition between the magnetic and superconducting behaviors [5].

$FeSe$  with tetragonal  $PbO$ -type structure was reported to undergo a phase transition leading to a hexagonal atomic structure. FeTe with the same tetragonal structure approaches the same transition, but at a much higher temperature. It is reasonable to think that the partial substitution of Te in  $FeSe$  should stabilize the tetragonal phase, which persists, in fact, for temperatures  $T > 730$  K (the threshold of  $FeSe$ ) [92].

The temperature dependence of the resistivity changes with the concentration of Te at zero magnetic field (fig: 3.6). For  $x < 0.2$ , the samples show metallic behavior in the normal state, while for  $x > 0.3$ , the normal-state resistance increases as the temperature decreases before the onset of superconductivity. Exactly for  $x = 0.2$ , a sharp drop in resistance is observed, signaling a superconducting phase transition

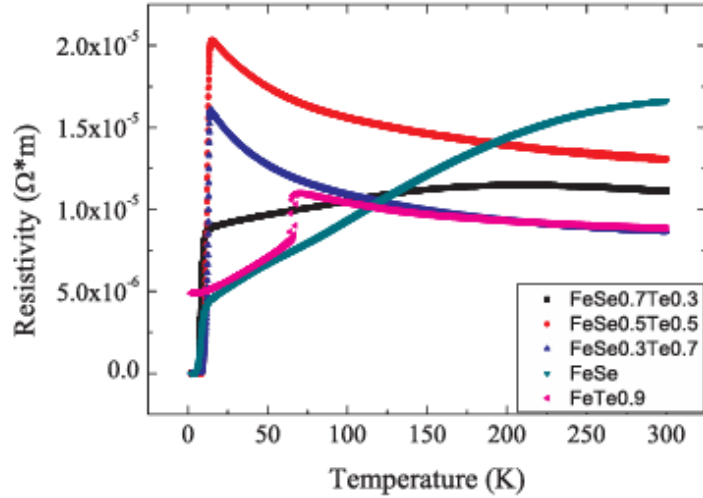


**Figure 3.6:** The figure shows the resistivity as a function of temperature for different concentration of tellurium. Reprinted from [5].

at  $T_C = 13.7$  K, which is higher than the onset value for the  $FeSe$  compound. However, the  $T_C$  value increases, reaching its maximum when  $x = 0.5$ , approaching 15.2 K. Indeed, a sharper superconducting phase transition is observed for  $x = 0.5$  and  $x = 0.7$ , indicating that these samples are more homogeneous.

It is interesting to observe that for these higher Te concentration samples, the normal-state resistance is of semiconductor type, even though the critical temperature increases. As the value of  $x$  increases further, the  $T_C$  decreases. For  $x = 0.9$ , the critical temperature drops to 11.4 K.

The variation in critical temperature can also occur through the application of high pressure, which enhances its value. This is linked to the structural deformation observed at low temperatures.

To study how Te doping affects the low-temperature structural change observed in  $FeSe$ , samples can be investigated using X-ray techniques at room and low temperatures.

Following figure 3.7, the lattice expands due to the fact that the ionic radius of Te is larger than that of Se. By normalizing the expansion values through the cell parameters, one can observe that the lattice actually expands in an asymmetric way: indeed, along the  $c$ -axis, the expansion is  $\sim 8.1\%$  (for  $x = 0.5$ ), while along the  $a$ -axis it increases by about 0.6% [5]. Increasing the number of Te atoms may lead to further expansion of the cell, and the distance between Fe-Fe in the iron plane increases. Moreover, the increase in the  $c$ -parameter provides an increase in the density of states at the Fermi level, enhancing the value of the critical temperature.

The bottom panel in figure 3.7 shows how both the  $\gamma$  angle of the distorted

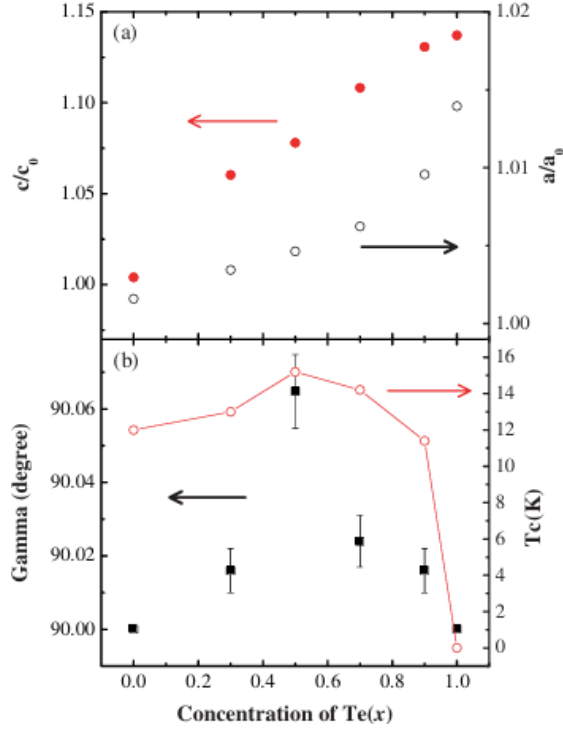


**Figure 3.7:** (a) Lattice expansion ratios of the tetragonal  $FeSe_{1-x}Te_x$  found through X-ray at room temperature, where  $a_0$  and  $c_0$  are referred to the lattice parameters of  $FeSe$ ; (b) The picture shows the behavior of the  $\gamma$  angle as a function of  $x$ , together with the critical temperature value. Note that here the critical point is defined as the temperature at which the resistance reaches the 90% of the normal state value. Reprinted from [5].

lattice and the  $T_C$  approach a maximum value exactly for  $x = 0.5$ . This correlated behavior suggests that the value of the critical point depends more deeply on the level of the distortion rather than the length of the Fe-Fe bond. At room temperature, the  $FeSe_{0.5}Te_{0.5}$  lattice actually distorts, which is correlated with what is observed for the  $FeSe$  compound when  $T < 105$  K. Indeed, we can observe that the mere presence of the Te atoms is sufficient to induce local strain in the lattice. This evidence suggests that structural distortion at low temperatures is deeply connected to the origin of superconductivity in  $Fe(Se, Te)$  compounds.

### 3.2.2 Topological character of $FeSeTe$

Topological insulators and iron-based superconductors have gathered significant attention in solid state physics due to the reasons previously discussed. Iron-based

superconductors, in general, are multi-orbital electronic systems whose electronic structure is mainly determined by the Fe 3d orbitals. Recent studies have shown that Fe-based superconductors can carry intrinsic nontrivial topological properties.

Among all the possible candidates,  $Fe(Se, Te)$  has also acquired significant interest. Indeed, single-layer  $Fe(Se_xTe_{1-x})$ , described by a critical value  $x_c \sim 0.7$ , seems to be capable of supporting nontrivial  $Z_2$  topological invariance, which originates from the parity exchange at the  $\Gamma$  point. This nontrivial topology comes directly from the Te(Se)-layer height, meaning that by manipulating this parameter, which can be adjusted through the concentration  $x$ , one can drive a topological phase transition. In the bulk material, the two-dimensional  $Z_2$  topology extends into a strong 3D  $Z_2$  invariance, while in a thin film, it shows an oscillatory behavior with a trilayer structure, being topologically trivial. These observations enable an important link between high-temperature superconductivity and topological properties, with  $Fe(Se, Te)$  acting as a central study material [7].

**Majorana zero modes** (MZMs) obey non-Abelian statistics, holding great potential for applications in topological quantum computation. We already discussed (see section 2.3.5) the appearance of MZMs in  $p$ -wave superconductors. In recent years, fully gapped bulk iron-based superconductors have emerged as a promising venue for Majorana Fermions. In particular, experimental evidence shows MZMs in topological vortices on the surface of  $FeTe_{0.55}Se_{0.45}$ , observed via **scanning tunneling microscopy/spectroscopy** (STM/S) [8, 9, 10].

When the system is cooled down to sufficiently low temperatures, the conductance of an MZM is characterized by a quantized plateau at the value  $2e^2/h$ , with  $e$  being the **elementary charge** and  $h$  the **Planck constant**. This quantized feature arises from perfect resonant **Andreev reflection**, which will be discussed later, guaranteed by the intrinsic particle-hole symmetric nature of MZMs [11, 93, 12].

Indeed, since the presence of MZMs is an important signal for a superconductor to be topologically non-trivial, iron-based materials show another important feature, namely **zero bias conductance peaks** (ZBCP), which can be studied via STM/S. Here, the tunnel coupling can be continuously tuned by changing the tip-sample distance, which automatically adjusts the tunnel-barrier conductance. Some experimental results show a sharp ZBCP at a vortex core in  $FeTe_{0.55}Se_{0.45}$  samples when a magnetic field of  $H = 2 T$  is applied (fig: 3.8). This peak does not disperse or split across the vortex core, remaining well-defined at zero energy.

However, in order to prove that  $Fe(Se_{1-x}Te_x)$  is a topological superconductor, it is not sufficient to observe MZMs and ZBCP, even though they are preliminary signatures of topological phases. Therefore, three further phenomena must be observed through spectroscopic measurements.

First, Dirac-cone-type surface states should arise through spectroscopy analysis. Then, one must also observe *helical spin polarization* of the surface states, which

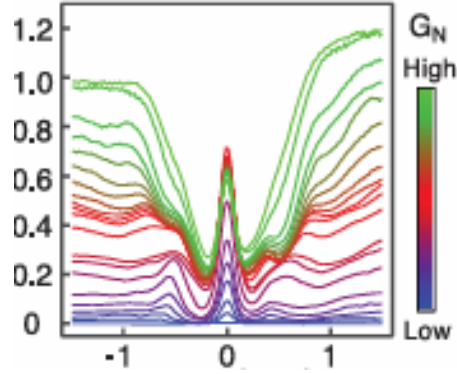


**Figure 3.8:** The plot shows the conductance spectra with different tunnel coupling values defined in  $G_N$ . The vertical axis is then given by  $dI/dV (2e^2/h)$  while the horizontal one measure energy in meV. Reprinted from [94].

aims to lock the spin direction perpendicular to the momentum direction. Finally, the system must exhibit an s-wave superconducting gap in the surface states when below the critical temperature [89]. However, the topological surface band has never been directly observed, which is due to the small energy and momentum scales. Indeed, Dirac-cone-type surface states can be studied using **angle-resolved photoemission spectroscopy** (ARPES).

Peng et al. [89] have been able to provide insights into the  $Fe(Se_{1-x}Te_x)$  ( $x=0.55$ ): a Dirac-cone-type topological surface band exists on its surface. Indeed, when the bulk bands open superconducting gaps, s-wave superconductivity is induced in the surface band via interband scattering, exhibiting topological superconductivity due to the *spin-helical* texture, whereas the bulk superconductive phase is topologically trivial. However, applying an external magnetic field leads to the appearance of a pair of MBSs, which can explain the emergence of zero-bias peaks (fig: 3.9). Additionally, if a magnetic order domain is imposed on the surface, it suppresses the superconducting phase within the domain, creating itinerant Majorana Fermions along the domain edge. Moreover, due to the intrinsic topological superconductivity on the surface, it should be easy to produce MBSs and Majorana edge modes. Finally, these topological features, combined with the high-temperature superconducting transition, make  $Fe(Se,Te)$ , which is also easy to grow, a promising platform for studying MBSs and paving the way for advancements in quantum computing [89].

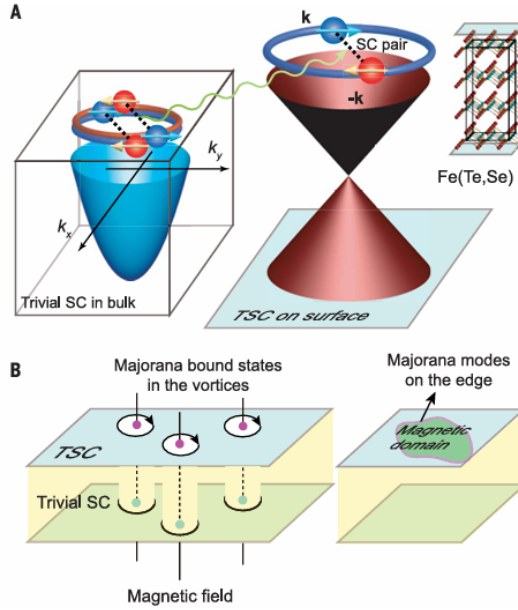


**Figure 3.9:** (A) A pictorial representation of topological superconductivity on the surface of  $FeTe_{0.55}Se_{0.45}$ , highlighting the distinction between bulk and surface states. In the bulk, the electrons are not spin-polarized, and the  $s$ -wave superconducting pairing is topologically trivial. (B) When a magnetic field is applied, it induces vortices in the system. These vortices act as boundaries for the topological superconductivity on the surface, where Majorana bound states are expected to emerge within the vortex cores. Reprinted from [89].

### 3.3 Multi-band Eliashberg theory

In section (2.4.4), we have seen how the iron-based superconductors are characterized by a particular shape of the Fermi surface, described by different sheets. Therefore, the energy gap can be different on each of them, leading to the appearance of **multi-band superconductivity**. The latter can also be viewed as a specific case of anisotropic superconductivity, and for this reason, an extension of the BCS theory is required, which takes into account two, or even more, bands. Indeed, in an interband superconducting system, such as the Fe-based superconductors, it is sufficient to consider a multi-band Eliashberg model with a small number of free parameters [95].

The possibility of interpreting the data using Eliashberg theory turns out to be very important when the information gathered on the energetic scale of the electron-boson coupling function, which is fundamental in the BCS theory, is not reliable. Indeed, the competition between the superconducting state and the magnetic order present in most Fe-based superconductors suggests that the starting point for the pairing mechanism is actually due to **spin fluctuations** [96], supported by experimental evidence that highlights the antiferromagnetic spin dynamics [97]. In the strong-coupling regime, some information on the spectrum of the mediating boson can be obtained through point contact Andreev reflection spectroscopy (PCARS) [98], allowing investigation of the coupling between electrons and Fermi surfaces.

In the Eliashberg theory [99] the order parameter is a complex function of energy

$$\Delta = \mathcal{R}e[\Delta(E)] + i\mathcal{I}m[\Delta(E)] \quad (3.1)$$

where  $E$  stands for the energy, while the imaginary part accounts for the finite lifetime of Cooper pairs describing the information about the electron-boson spectrum, well denoted as  $\alpha^2F(\omega)$  (**Eliashberg function**). Note that also the **superconducting density of states** (DOS)  $N(E) = \text{Re}[E/(E^2 - \Delta^2)]$  extracts some information on the electron-boson interaction [100]. However, even though in multi-band superconductors it is not possible to completely determine the  $\alpha^2F(\omega)$  as in single-band ones, it is possible to try to reproduce the observed features in the conductance curve by choosing different electron-boson spectra. Again, in this field, an important contribution is provided by PCARS, which can give an experimental valuation to the theoretical results predicted by the theory. However, some assumptions are needed: first, we consider the case in which the electronic structure of Fe-based superconductors can be described by one hole band (denoted as band 1) and two electron bands (denoted as bands 2 and 3). Moreover, the gap symmetry is assumed to be  $s\pm$ , such that the sign of the gap  $\Delta_1$  (related to band 1) is the inverse of that of  $\Delta_2$  and  $\Delta_3$  [95, 101].

Indeed, many spectroscopy techniques show at most two gap amplitudes for iron-based superconductors, meaning that one needs to take into account at least three effective bands for the Eliashberg model in order to reproduce results correctly. These gaps and the critical temperature can be derived in the  $s\pm$  wave three-band Eliashberg theoretical model, where it is sufficient to solve six coupled equations for the gaps  $\Delta_i(i\omega_n)$  (where  $i = 1 \dots 3$  is the band index) and the renormalization functions  $Z_i(i\omega_n)$ . Therefore, the crucial quantity is given by the **electron-boson coupling constant** identified by

$$\lambda_{ij}^{ph,sf} = 2 \int_0^{+\infty} d\Omega \frac{\alpha_{ij}^2 F^{ph,sf}(\Omega)}{\Omega} \quad (3.2)$$

where  $\Omega$  describes the energy of the mediating boson in terms of frequency. However, solving these equations is a hard problem, as one needs to provide a large number of input parameters. Fortunately, some of them are actually correlated, so several approximations can be applied, and some values can be inferred by experiments in order to simplify the equations themselves. For instance, let's consider the coupling constant matrix: each entry  $\lambda_{ij}$  is, in general, composed of a contribution due to the electron-phonon interaction and another from the electron-spin fluctuation (SF), which in turn leads to  $\lambda_{ij} = \lambda^{ph} + \lambda^{sf}$ . One can observe that the coupling between two electron bands (band 2 and 3) is small, so the related constant coupling can be set to zero, i.e.,  $\lambda_{23} = \lambda_{32} = 0$ ; moreover, one should take into account that in pnictides, the electron-phonon coupling is small too, leading to a dominant contribution arising from intra-band coupling only. Indeed, for compounds like  $Fe(Se, Te)$ , one has  $\lambda_{ij}^{ph} = 0$ ; finally, spin fluctuations provide inter-band coupling between the two quasi-nested FS sheets, leading to  $\lambda_{ii}^{sf} = 0$  [101, 102]. In conclusion one has [103]:

$$\lambda_{ij} = \begin{pmatrix} \lambda_{11}^{ph} & \lambda_{12}^{sf} & \lambda_{13}^{sf} \\ \lambda_{21}^{sf} & \lambda_{22}^{ph} & 0 \\ \lambda_{31}^{sf} & 0 & \lambda_{33}^{ph} \end{pmatrix} \quad (3.3)$$

However, the crucial ingredient remains the electron-boson spectral function  $\alpha^2 F(\Omega)$  of the bosons involved in the pairing, which has to be specified for each case, since some differences can lead to important modification.

In conclusion, as mentioned earlier, another important quantity for studying iron-based superconductors, such as in our case, is the spectral function  $\alpha^2 F^{ph,sf}(\Omega)$ . While the electron-phonon spectral function can be found in the literature [104], for spin fluctuations, we assume that the spectrum is characterized by a Lorentzian shape [13]:

$$\alpha^2 F^{sf}(\Omega) = C_{ij} [L(\Omega + \Omega_{ij}, Y_{ij}) - L(\Omega - \Omega_{ij}, Y_{ij})] \quad (3.4)$$

where

$$L(\Omega \pm \Omega_{ij}, Y_{ij}) = \frac{1}{(\Omega \pm \Omega_{ij})^2 + Y_{ij}^2} \quad (3.5)$$

and  $C_{ij}$  are normalization constants, crucial in determining the values of the coupling constants( $\lambda_{ij}$ ). Here,  $\Omega_{ij}$  and  $Y_{ij}$  represent the peak energies and the half-widths of the Lorentzian functions, respectively [95].

## Chapter 4

# Point-contact spectroscopy (PCS)

### 4.1 Basics concepts of PCS

**Point contact spectroscopy** (PCS) is a very useful experimental technique that provides insight into the scattering events affecting conduction electrons, by studying the I-V characteristics of contacts between metals. Discovered in the 1970s by Yanson, this method was initially applied to the study of conductor metals to characterize various scattering processes, such as interactions with phonons, magnons, or defects. However, due to its effectiveness, this technique has since been extended to the study of superconductors.

In materials exhibiting a superconducting phase transition, the interface between the metal and the superconductor allows the observation of quantum phenomena, such as **Andreev reflection** or **quasi-particle tunneling**, depending on the height of the potential barrier at the interface. By fitting the resulting I-V curve, one can estimate the superconducting gap  $\Delta$ , its symmetry, and other intrinsic properties [105].

The strength of the PCS technique is related to its no-destroying character, indeed several measurements can be performed on the same sample without any important damage on it. The procedure has two different ways to be performed: the first consists in electrically contacting the surface of the material with a sharp metallic tip; the second takes place through metallic wire (usually Au or Pt wire) which is stuck on the surface by means of a silver paint (Ag-paint) (fig. 4.1). In both cases the size of the contact plays a crucial role for the quality and the accuracy of the measurement.

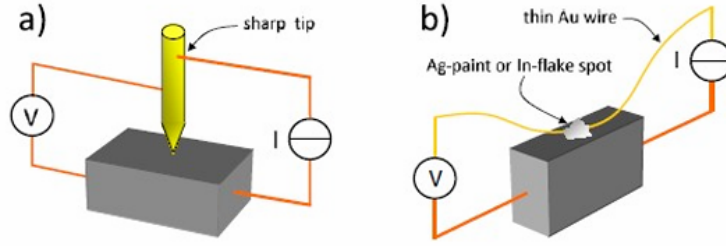


**Figure 4.1:** Pictorial experimental setup for PCS measurement in the two configurations. (a) Metallic probe that contacts the surface of the material; (b) Soft-PC procedure that uses Ag-paint or IN-flake spot to stabilize the metallic wire. Reprinted from [105].

### 4.1.1 Different spectroscopy regimes

The PCS produces good results if one can guarantee some important features strictly related to the geometry of the contact itself. In the normal contact case (metallic tip), these conditions are taken into account by the **Knudsen ratio** defined as

$$K = \frac{l}{a} \quad (4.1)$$

where  $l$  represents the mean free path of the conduction electrons while  $a$  is the contact surface area. Based on its value we can distinguish three different regimes in which the measurement can be more or less reliable showing different features.

#### Thermal regime

The **thermal regime** is determined by the condition  $K \ll 1 \Rightarrow l \ll a$ , where we can easily find the resistance of the junction, computed by Maxwell, leading to

$$R_M = \frac{\rho}{2a} \quad (4.2)$$

with  $\rho$  is the **resistivity** of the material.

The formula can be derived by observing that when  $a \gg l$ , the electrons undergo inelastic scattering, and their flux is tuned by means of the contact, which is determined by diffusion processes. In these conditions, one can assume the validity of Ohm's law  $\mathbf{j} = \sigma \cdot \mathbf{E}$ , from which we can derive the Maxwell resistance. Indeed, when the electrons pass through the contact, their kinetic energy is entirely converted into thermal energy due to dissipation effects, which depend on the value of the applied voltage. In fact the maximum temperature reached at the center of the contact can be evaluated:

$$T_{max}^2 = T_{bath}^2 + \frac{V^2}{4L} \quad (4.3)$$

with  $T_{bath}$  is the external temperature (which can be controlled) and  $L$  it's the **Lorentz number**  $L = \chi/\sigma T$ , defined by the ratio between the **thermal conductivity** ( $\chi$ ) and the electrical one ( $\sigma$ ).

### Ballistic regime

The **ballistic regime** is described by the condition  $K \gg 1 \Rightarrow l \gg a$ , obtained with a very small contact area. In this regime, the voltage drop between the electrons is entirely localized on the contact region. When the electrons flow through the metallic wire, they are actually accelerated and then pushed into the second electrode with an energy given by  $eV$  ( $e$  being the elemental charge), without undergoing scattering events. This is also known as **Sharvin limit** and the resistance of the contact can be evaluated [106]

$$R_0 = R_S = \frac{4}{3} \frac{\rho l}{\pi a^2} \quad (4.4)$$

This value turns out to be independent of  $l$  since  $\rho \propto l^{-1}$ , so the dependence on the mean free path is eliminated by their product, meaning that the only degree of freedom is the geometry of the contact ( $\rightarrow a$ ). Moreover, this value corresponds to the zero-order resistance, found by solving the Boltzmann equation, which can be implemented only when no interactions occur. Indeed, the Sharvin limit is an approximation because the electrons passing through the contact always experience at least one inelastic scattering due to the presence of phonons or impurities.

In order to take into account these higher-order processes, one needs to consider different contributions to the current passing through the contact due to the several scatterings (fig: 4.2), leading to an increase in the measured resistance. The first order correction is provided by

$$I^{(1)} = \frac{2\pi e}{\hbar} \Omega_{eff} N(0) \int_0^{eV} d\epsilon \int_0^\epsilon d\epsilon' S(\epsilon - \epsilon') \quad (4.5)$$

with  $N(0)$  it's the density of states evaluated at the Fermi energy,  $\Omega_{eff} = 8a^3/3$  is the effective volume available for the inelastic scattering which are responsible for the correction and  $S(\epsilon)$  consists in the spectral function of the related interaction [105]. In the particular case of the electron-phonon (strong) coupling the spectral function is defined by the already discussed  $\alpha^2 F(\Omega)$  of the Eliashberg theory (see section 3.3) mediated by the **efficiency function**:

$$\eta(\theta) = \frac{1}{2} \frac{(1 - \theta)}{\tan \theta} \quad (4.6)$$

which aims to take into account the contribution of the scattering angle  $\theta$ , defined as the angle difference between the direction of the electron before and after the

scattering.

Some information about the spectral function of the electron-phonon scattering can be gathered just by considering the second-time derivative of the current with respect to the voltage

$$\frac{d^2 I}{dV^2} = \frac{4e^3 m_e^2 v_F}{3\pi \hbar^4} a^3 \alpha^2 F_p(eV) \quad (4.7)$$

where  $m_e$  is the electron mass evaluated at the Fermi level,  $v_F$  the Fermi velocity.

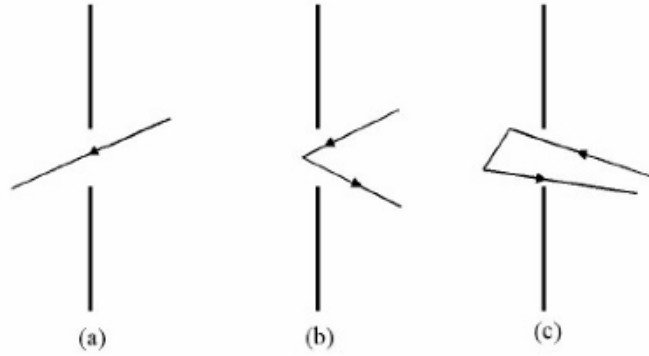


**Figure 4.2:** The figure shows the three kind of scattering that can experience the electrons: (a) zero-order contribution (no scattering); (b) single collision and momentum inversion; (c) double scattering. Reprinted from [107].

### Intermediate regime

This regime can be found between the thermal and the ballistic one, here the expression of the resistance change again and was found years ago by the physicist Wexler for an *homogeneous contact*

$$R = \frac{4\rho l}{3\pi a^2} + \Gamma(K) \frac{\rho}{2a} \quad (4.8)$$

it is composed by two terms: the first coincides with the Sharvin definition while the second corresponds to the Maxwell one weighted by the  $\Gamma$  coefficient which weakly depends on the Kundsens's ratio and can range between  $[0.7; 1]$  where the extremes correspond respectively to  $K = \infty$  and  $K = 0$ . However, the  $\Gamma$  coefficient is usually set at 1, and the dominant contribution depends on the value of the contact radius  $a$  [105].

When we deal with a *hetero-contact*, the expression of the measured resistance becomes more complex because we need to take into account the differences between the materials, for which we assume spherical Fermi surfaces

$$R = \frac{2h}{e^2 a^2 (\min[k_{F2}, k_{F1}])^2} \mathcal{Y} + \Gamma(K) \frac{\rho_1 + \rho_2}{4a} \quad (4.9)$$

with

$$\mathcal{Y} = \frac{4k_{F1}k_{F2}}{(k_{F1} + k_{F2})^2} \quad (4.10)$$

where  $\rho_i, k_{Fi}$  are related to the  $i = 1, 2$  metal. In particular  $k_F$  is the Fermi wave vector which describes the radius of the Fermi surface of both materials and they are used in the assumption that the contact occurs between two simple metals for which one can assume the **free electron approximation** [108]

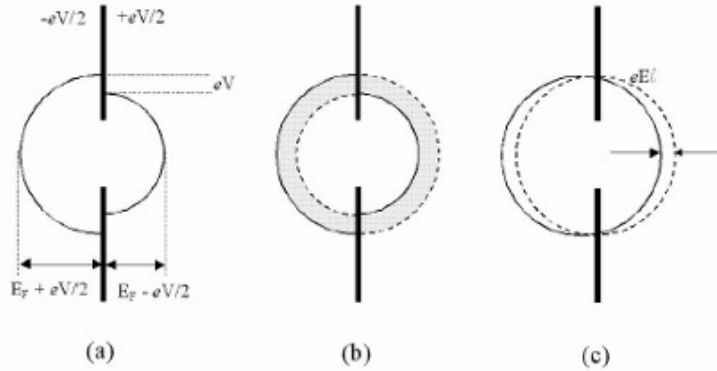


**Figure 4.3:** The panels illustrate the electron distribution at the center of a perfect contact across three distinct transport regimes: (a) Ballistic, (b) Intermediate, (c) Thermal. Reprinted from [55].

### Diffusive regime

The **diffusive regime** takes place in between the ballistic and the intermediate one. Here the mean free path is still very small with respect to  $a$ , but its **diffusion length**  $\Lambda = \sqrt{l_i l_e}$  for the inelastic scattering is greater than the contact radius. That's why the scatterings experienced by the electrons are only the elastic ones [105]. These kinds of scattering processes do not imply any dissipation effect and, by consequence, they do not provide any thermal energy to the contact region. However, they affect the electron distribution and, hence, the Fermi surface because the electrons are redistributed in an isotropic way inside an energetic shell  $\sim eV$  around the surface itself (fig: 4.3). Moreover, the inelastic scattering is still present but it actually enters in a different way: it shows a reduction of the effective volume  $\Omega_{eff}$  by a factor  $a/l$  with respect to the ballistic regime because the probability that the electron was scattered back decreases due to the simultaneous presence of

the elastic scattering (which dominates now) [105]. In conclusion, the expression of the resistance in this regime changes also because of the modification introduced in the *efficiency function* which no longer requires the constraints related to the conservation of momenta, which is intrinsic in the elastic scattering process [105].

### 4.1.2 Soft-PC

The **soft point-contact** procedure was introduced to overcome some problems that affect the standard PCS such as the occasional damage of the surface because of the metallic tip or the mechanical stability of the contact itself. Indeed, even a very small stress on the tip, caused by thermal contraction at low temperature, can destroy the contact and make the measurement not accurate.

The soft-PC consists in keeping the metallic wire (usually made of Au or Pt) locked on the surface thanks to the help of chemical substances such as conductive silver-paint. Even if the paint spot seems to be large, the effective contact region is still sufficiently small to guarantee the ballistic regime. In particular, the contact area is characterized by multiple parallel nano-contacts which provide a certain resistance. Then, the resistance of the single contacts can be higher than the total one and thus, it's possible to obtain a parallel between ballistic and diffusive contacts leading to a very low resistance. The latter can be modified by providing short voltage pulses to the junction, thanks to which one can stop some nanoscopic contacts and open others, causing a variation in the total resistance. However, this procedure needs to be controlled in order to guarantee accurate measurement; indeed, the optimal value of resistance goes up to  $\sim 100 \Omega$ .

If the material is polycrystalline, the contact is located equivalently on one of the surfaces. By the way, one needs to make the spot on a part of it that is not oxidized, therefore it is necessary to expose a "clean" surface in order to make reliable measurement.

If the sample is a single crystal or a thin film, the contact is made in such a way to direct the current usually along the  $c$ -axis or, more rarely, along the  $ab$  plane. In this case, it's crucial to keep track of the roughness of the material, which can be measured by means of **atomic force microscope** analysis (fig: 4.4).

## 4.2 Andreev reflection

PCS is an important procedure able to study the interaction of electrons with elemental excitations which can be different for each material, such as phonons in metals, magnons in magnets, etc. When one of the electrodes in point-contact measurements is a superconductor, we observe that a **N-S junction** (normal-superconductor) is formed, where the optimal condition is reached in the ballistic regime, enabling the **Andreev reflection** (PCAR) spectroscopy. For simplicity, we

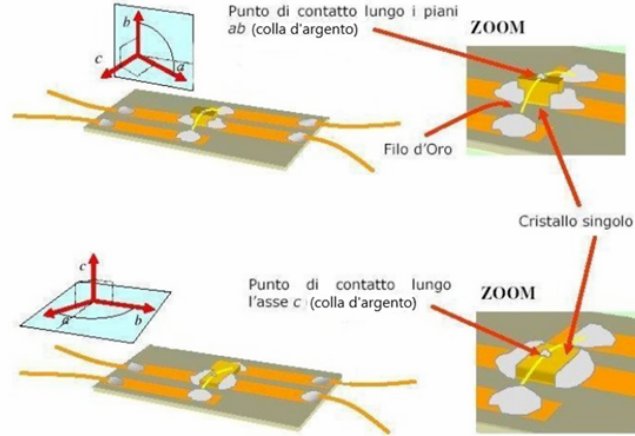


**Figure 4.4:** Schematic view of how to build the soft-PC setup in the case of the current directed along  $ab$  plane (top panel) and along the  $c$  axis (bottom). Reprinted from [105].

consider an isotropic gap superconductor with no potential barrier at the interface, meaning that the contact is a pure metallic one.

Depending on the value of the applied voltage on the junction with respect to the superconducting gap  $\Delta$ , we can observe two possible cases:

#### Case 1: $V < \Delta/e$

In this case, we cannot have any electrons coming from the metallic part of the junction that are able to propagate through the interface since in the superconductor only Cooper pairs can exist in this energy range. However, the electrons cannot be totally reflected in the metal either, otherwise, one couldn't observe any current between the metal and superconductor, which is indeed measured experimentally. We can deal with this system using a theoretical approach based on the **Bogoliubov-De Gennes** equation, which admits the possibility that the electron gets reflected into the normal metal as a hole, simultaneously injecting a Cooper pair in the SC, defining the **Andreev reflection** phenomenon (fig: 4.5).

Therefore, if this is true, the procedure needs to satisfy the charge and momentum conservation laws, and for this reason, it is necessary that 2 electrons, forming a Cooper pair, flow in the superconductor, adding them to the condensate. Macroscopically speaking, the incident electrons provide a charge equal to  $2e$ , doubling the conductance of the SC, implying a conversion into supercurrent at the interface. Moreover, since the wavevector  $\mathbf{k}$  remains the same, and observing that the incoming particle is an electron while the reflected one is a hole, the group

velocity changes sign, meaning that the path followed by the hole in the normal metal exactly retraces the same path of the electron unless scattering events occur.

It's also important to point out that the Andreev reflection phenomenon does not provide any increase in entropy since both the electron and hole belong to the same fermionic excitation in the normal metal, leaving the occupation number unchanged during the process. This means that there is no dissipation effect in the process and thus a zero-value resistance at the interface of the junction (fig: 4.5).

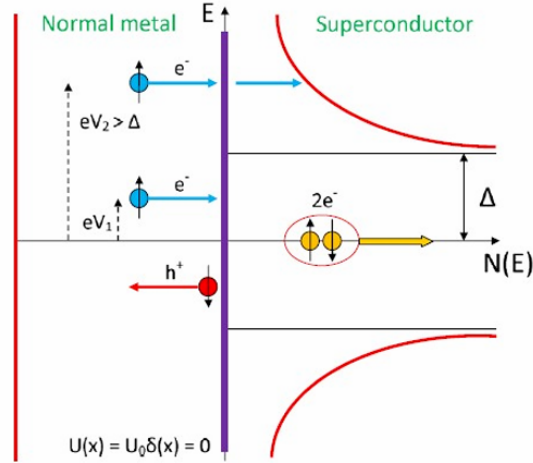


**Figure 4.5:** Schematic representation of PCARS in an ideal N-S junction at zero temperature, illustrating the cases in which the electron energy is larger or smaller than the superconducting energy gap. When the electron energy is larger than the gap, it generates a Cooper pair, and normal transmission occurs. When the electron energy is smaller than the gap, Andreev reflection takes place, where a hole is reflected back into the normal metal. Reprinted from[105].

In particular, when the conductance is enhanced because of the electron injection as a Cooper pair, this produce a non linearity in the I-V characteristic which gives information about the elementary excitations experienced by the electrons themselves. Indeed, PCAR is considered a useful tool to gather some signature of **Majorana fermions** which consist in form of quasi-particle excitation for the electrons exhibiting **zero bias conduction peak** (ZBCP) that are the preliminary sign of potential topological character.

### Case 2: $V \gg \Delta/e$

When this condition is satisfied, a certain number of electrons having energy between 0 and  $\Delta$  undergoes the Andreev reflection, which gives a constant contribution through the junction, defining the *excess current* independent of the applied bias. Instead, the electrons characterized by an energy greater than  $\Delta$  are injected

into the superconducting part of the junction, resulting in a conductance value equal to that of a N-N junction described by a current that depends on the applied voltage [105] (fig: 4.6).

Let's consider, for instance, the case where the area of electron injection is very small. This leads to a high value of current density, inducing a small volume of the superconductor to undergo a phase transition to the normal state. Here, even for small values of the applied bias, the electrons flowing through the interface experience the Andreev reflection phenomenon, getting reflected as holes in the normal metal, retracing the same path of the incoming electrons. When  $V > \Delta/e$ , a part of the electrons is still affected by the AR process, while most of them penetrate the superconductor with energy higher than the gap without being reflected.

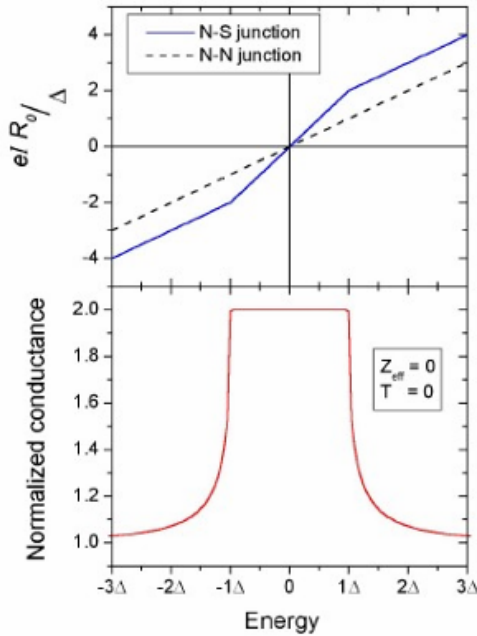


**Figure 4.6:** The picture proposes a comparison between the N-N/N-S junction through their I-V characteristic. The panel below shows the normalized conductance of the N-S junction at  $T=0$  following the BTK model. Reprinted from [55].

## 4.3 Fitting models

### 4.3.1 BTK 1D model

The junction behavior is theoretically described by the model proposed by Blonder, Thinkam, and Klapwijk in 1982, which deals with a superconductive junction characterized by a small contact area and a high current density, the most frequently encountered case. The model is known as the **BTK model**, which provides a generalized description for the Andreev reflection occurring at the interface of the N-S junction. The model is based on the Bogoliubov-De Gennes equations, which are able to characterize the quasi-particle states in superconductors where the coupling potential actually depends on the position, allowing the determination of the probability current due to the quasi-particle excitation [109].

The model was developed based on the assumption that all the momenta are perpendicular to the interface, while the energy barrier between the normal metal and the superconductor is described as a sharp repulsive potential  $U_0\delta(x)$  localized at the interface. Then we introduce the non-dimensional quantity

$$Z = \frac{U_0}{\hbar v_F} \quad (4.11)$$

where  $v_F$  is the Fermi velocity and  $Z$  incorporates the characteristic of the barrier. Indeed, when  $Z$  is small also the barrier is since the electrons require lower energy in order to pass the potential barrier. However, an electron coming from the normal part of the junction can experience 4 different processes with a given probability:

- **Probability that Andreev reflection occurs:** the electron is reflected as an hole going back through the path of the incoming particle. In particular this probability decrease when  $eV < \Delta$  and  $Z$  increases while in the case of  $eV > \Delta$  the electrons cannot cross the junction in any case (case A in fig. 4.7).
- **Mirror reflection probability:** the electron is reflected as it is; the chance of this case increases with the increasing of the barrier height (case B in fig. 4.8).
- **Transmission probability in the superconductor as an electron-like quasiparticle (ELQ):** as the barrier increases this probability decreases while when  $eV < \Delta$  this probability measure is zero (case C in fig. 4.7).
- **Transmission probability in the superconductor as an hole-like quasiparticle (HLQ):** here the particle crosses the Fermi surface describing an **anomalous** reflection; this probability has zero value when  $eV < \Delta$  and still small in the opposite case (case D in fig. 4.8).

If a potential barrier is present ( $Z \neq 0$ )  
four cases are possible:

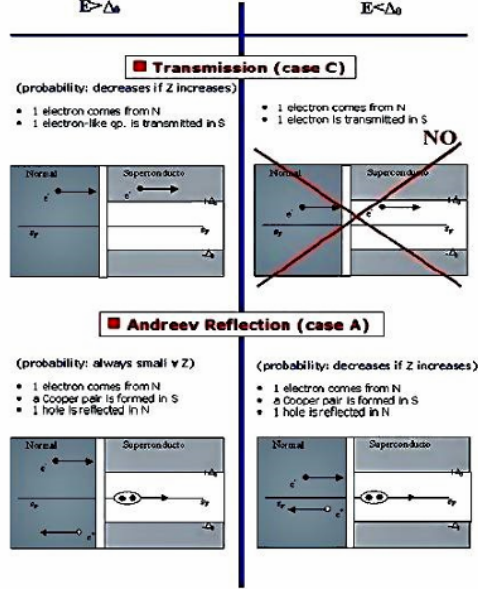


**Figure 4.7:** Pictorial representation of the probabilities of the cases A/C. Reprinted from [105].

Based on these different cases as consequence several contributions to the conductance of the N-S junction arise. We focus on the *normalized* conductance using the value when the superconductor is in its normal state, i.e  $G = (dI/dV)_{NS}/(dI/dV)_{NN}$  measured at  $T=0$ . For the purpose of the model we introduce some parameters

$$\tau_N = \frac{1}{1 + Z^2} \quad (4.12)$$

known as **transparency** of the barrier, which is linked to the opposite of the barrier strength  $Z$ . Also we have

$$\gamma(E) = \sqrt{\frac{E - \sqrt{E^2 - \Delta^2}}{E + \sqrt{E^2 - \Delta^2}}} = \frac{E - \sqrt{E^2 - \Delta^2}}{\Delta} \quad (4.13)$$

fundamental for derive the conductance from the Bogoliubov-De Gennes equation which reads

$$\sigma(E) = \tau_N \cdot \frac{1 + \tau_n |\gamma(E)|^2 + (\tau_N - 1) + |\gamma(E)|^2}{|1 + (\tau_N - 1)\gamma(E)|^2} \quad (4.14)$$

and then

$$G(E) \doteq \frac{\sigma(E)}{\tau_N} \quad (4.15)$$

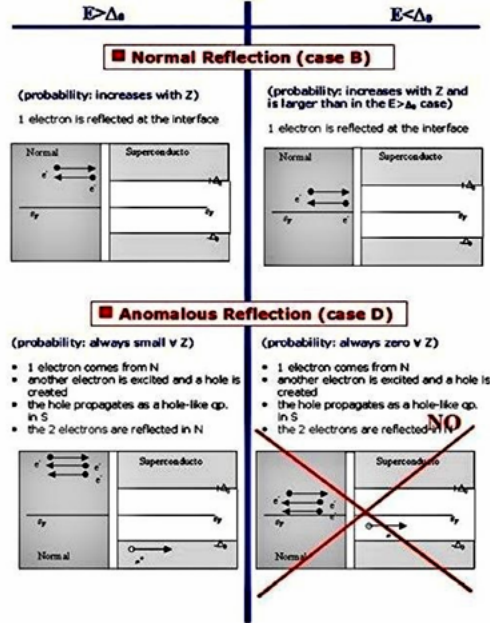


**Figure 4.8:** Schematic view of the probabilities associated to the possible reflection of cases B and D. Reprinted from [105].

For instance, figure 4.9 shows the behavior of the normalized conductance for different values of  $Z$  and temperature when the other is fixed. We can observe that when  $Z = 0$ , which corresponds to the perfect transparency case, the dominant process is the Andreev reflection (4.2), implying a double value for the conductance when  $\Delta > eV$ ; for  $Z \in (0; 10)$  and  $\Delta \approx eV$ , we observe two peaks, while the zero-bias conductance assumes lower values. When  $Z > 10$ , at  $T = 0$ , one can recognize the quasiparticle density of states described in BCS theory. Indeed, as soon as the transparency starts to decrease, the probability related to the Andreev reflection also decreases, allowing for the phenomenon of the **tunnel effect**: the electron has a non-zero probability of passing through the barrier even if it doesn't have sufficient energy to overcome the barrier, with the constraint that free electron states exist in the superconducting compound, i.e., the energy of the particle is still greater than the superconducting gap.

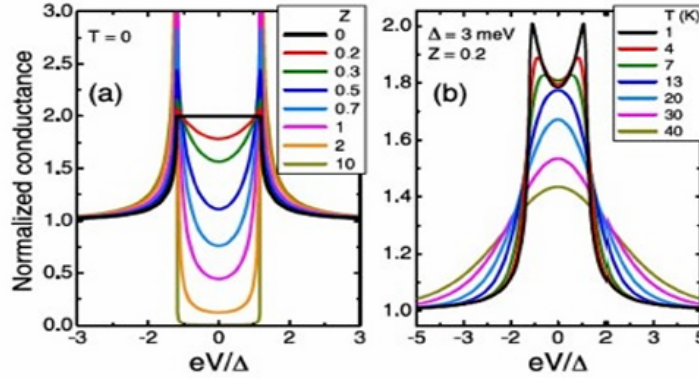


**Figure 4.9:** The scheme shows the behavior of the normalized conductance at fixed  $T$  (left) and  $Z$  (right) letting free respectively  $Z$  and  $T$ . On the left panel we can observe that as  $T$  increases the conductance gets lowered passing from a two-peaked shape to a single peak one set at zero bias. Reprinted from [105].

However, the BTK approach is not an exact model. Despite its fundamental utility, it is based on several approximations which allow one to obtain simple and clear results.

The computations are made in the ideal case of zero temperature, assuming a one-dimensional process, meaning that the incoming particles are perpendicular to the interface and parallel to the current. Then the potential barrier is of  $\delta$ -type, i.e., with zero width, while the Fermi surface is spherical and identical on both sides of the junction. Finally, the superconductor is homogeneous, isotropic, has an  $s$ -symmetry gap, and is characterized by a flat and pure contact with the normal metal.

In order to build a more general method, some of these assumptions need to be relaxed. For instance, we can drop the  $T = 0$  condition by calculating first the zero-temperature conductance and then performing the convolution integral with the Fermi distribution, evaluating it at the desired temperature. Moreover, one can also try to describe two-dimensional processes in order to consider the case of an anisotropic gap, which characterizes most of the Fe-based superconductors. These considerations lead to the development of the **BTK 2D model**, built by Y.Tanaka and S.Kashiwaya.

### 4.3.2 2D BTK model

The **2D BTK model** provides a more concrete treatment compared to the 1D approach, which is characterized by many approximations. Here, the electrons can cross the interface along any direction, dictated by the angular measure  $\theta_N$ ,

given that the normal component of the velocity ( $\mathbf{v} \cdot \mathbf{n}$ ) is oriented towards the superconducting part of the junction while the wavevector  $\mathbf{k}$  remains parallel to the interface during the entire process [110].

This geometric degree of freedom is, indeed, quite important since it affects the expression of the transparency coefficient, which now depends on  $\theta_N$  too. So one has

$$\tau_N(\theta_N) = \frac{\cos^2(\theta_N)}{\cos^2(\theta_N) + Z^2} \quad (4.16)$$

which turns out to coincide with the expression 4.12 when the angle is zero, i.e when the incoming electron is perpendicular to the interface (fig: 4.10)

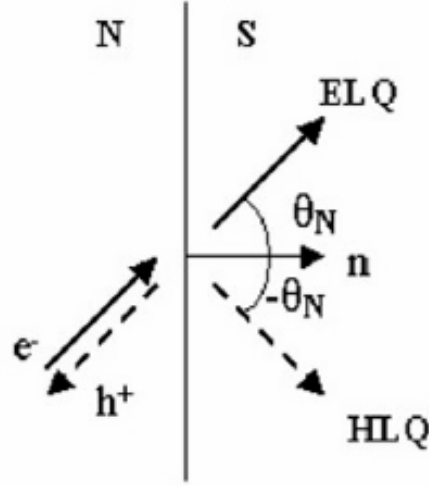


**Figure 4.10:** Geometric representation of the electron crossing the N-S interface with an angle  $\theta_N$  with respect to the interface itself. Reprinted from [105].

Indeed, if  $Z=0$  all the particles are transmitted with same probability meaning that  $\tau_N \simeq 1$ , but as  $Z$  increases not all the electrons are transmitted: the particles which hit the surface with a given angle  $\theta_N$  close to  $\pi/2$  have higher chance to be reflected by the surface ( $\tau_N \simeq 0$ ). By consequence also the expression of the conductance is affected by this new parameter reading

$$\sigma(E, \theta_N) = \tau_N(\theta_N) \cdot \frac{1 + \tau_N(\theta_N)|\gamma(E)|^2 + (\tau_N(\theta_N) - 1)|\gamma(E)^2|^2}{|1 + (\tau_N - 1)\gamma(E)^2|^2} \quad (4.17)$$

which holds only for an isotropic gap. In order to consider also the non-isotropic case we need to take into account also the dependence on the wavevector  $\mathbf{k}$  and

then specify between the gap "seen" by the ELQ or the one "seen" by the HLQ characterized respectively by the angle  $\theta$  and  $(\pi - \theta)$  where the angle lives in the azimuthal plane  $(k_x, k_y)$  [110]. Therefore, if one assumes that the  $x$  direction is the perpendicular one with respect to the interface, the gap related to the EQL is denoted as  $\Delta_+ = \Delta(\theta)$ , while the dual case is given by  $\Delta_- = \Delta(\pi - \theta)$  leading to the expression

$$\sigma(E, \theta_N) = \tau_N(\theta_N) \cdot \frac{1 + \tau_N(\theta_N)|\gamma_+(E)|^2 + (\tau_N(\theta_N) - 1)|\gamma_+(E)\gamma_-(E)|^2}{|1 + (\tau_N - 1)\gamma_+(E)\gamma_-(E)\exp(i\phi_d)|^2} \quad (4.18)$$

where  $\phi_d = (\phi_- - \phi_+)$  is the phase difference associated to the gaps  $\Delta_{\pm}$  which can assume two values (0 or  $\pi$ ) depending on the sign of the gap, while instead

$$\gamma_{\pm}(E) = \frac{E - \sqrt{E^2 - |\Delta_{\pm}|}}{|\Delta_{\pm}|}. \quad (4.19)$$

Moreover, we have now to consider all the contributions coming from all the possible angles  $\theta_N$  which translates in integrating over all its possible values allowing one to compute the normalized conductance which is now expressed as:

$$G_{2D}(E) = \frac{\int_{-\pi/2}^{+\pi/2} \sigma(E, \theta_N) \cos(\theta_N) d\theta_N}{\int_{-\pi/2}^{+\pi/2} \tau_N(\theta_N) \cos(\theta_N) d\theta_N} \quad (4.20)$$

which refers to the zero temperature case. Again, in order to approach the value also for higher temperatures we need to compute a convolution with the Fermi function evaluated at that specific temperature.

### Broadening parameter

Despite the accurate and clear interpretation provided by the BTK model, if one compares the experimental results obtained on the conductance curves and the ones fitted by the model, some differences are evident: in particular, the maximum value of the fitted curve turns out to be more peaked with respect to the real case, meaning that the BTK curves are less broadened.

This discrepancy is due to the fact that the quasi-particle has a finite lifetime and, consequently, a not well-defined energy. However, also some external factors can affect this intrinsic behavior: inelastic processes reduce the lifetime of the quasi-particle when crossing the interface because of the presence of defects, superficial contamination, or degradation of the sample.

In this respect, we introduce the **broadening parameter**  $\Gamma$ , which enters as the imaginary part of the energy, affecting all the already written physical quantities (fig: 4.11). Indeed, it's sufficient to substitute each  $E$  with  $E - i\Gamma$  and, for instance the normalized conductance is written as

$$G_{2D}(E) = \frac{\int_{-\pi/2}^{+\pi/2} \sigma((E - i\Gamma), \theta_N) \cos(\theta_N) d\theta_N}{\int_{-\pi/2}^{+\pi/2} \tau_N(\theta_N) \cos(\theta_N) d\theta_N} \quad (4.21)$$

Again, the recipe to build the fitting for temperatures different from 0 is the following: first, one has to compute  $G_{2D}(E)$  at  $T = 0$  using the broadening parameter as shown before; then we are in a position to start the convolution operation with the Fermi function at different temperatures, concluding with the tuning of all the parameters in order to build a curve that well reproduces the experimental one.

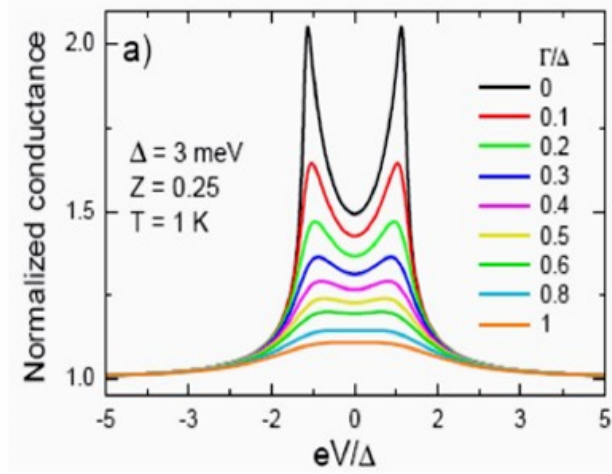


**Figure 4.11:** Example of fitting curve where the broadening parameter is present with different values with respect to the gap one. Reprinted from [105].

In conclusion, the model is well described by the cooperation of three parameters:  $\Delta$ ,  $Z$ , and the new one  $\Gamma$ . Thanks to the variation of these parameters, one is able to find a good fit for superconductors having isotropic or anisotropic gaps depending on the angle  $\theta$ , also for temperatures different from zero.

**Soft-PC and spreading resistance** When performing the soft point contact measurement, in order to achieve accurate spectroscopic results, the electrons crossing the electrodes must not lose energy, i.e., dissipation is forbidden. If one of the electrodes is highly resistive, the dissipation effect can become significant. For this reason, it is necessary to introduce a new resistance component known as the **spreading resistance**  $R_{SP}$ , whose value can affect the entire measurement.

The technique itself requires the use of Ag-paint to ensure both the mechanical stability and electrical conductivity of the wire, which may lead to a significant

increase in  $R_{SP}$ . However, the resistance of the silver spot is actually much smaller than that of the contact, which is of the order of some hundreds of Ohms, while the former is just a few Ohms and can be considered negligible.

Nonetheless, this contribution may not be insignificant when the sample is in its normal state. For instance, thin films can exhibit high resistance values even if their resistivity is not large, implying that a pure geometric effect is present. This effect leads to an increase in the superconductive electrode's resistance (usually zero) to a value comparable with the normal one as the temperature approaches the critical point.

### 4.3.3 BTK model for d-symmetry gap

One of the most interesting gap shapes in nature is denoted as the **d-symmetry gap**. In this case, one can utilize the BTK 2D model, where the superconducting gap depends on the azimuthal angle  $\theta$ .

Let us consider an energy gap with a symmetry  $d(x^2 - y^2)$ , which is defined as  $\Delta = \Delta_0 \cos(2\theta)$ . It follows that for  $\theta = \pi/4$ , the gap acquires a zero value, while it is positive for  $\theta < \pi/4$  and negative for  $\theta > \pi/4$  (fig: 4.12).

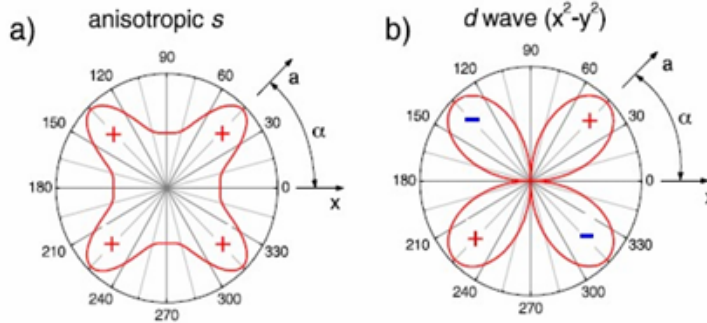


**Figure 4.12:** The picture shows on the left a schematic representation of an *s*-wave anisotropic gap, while on the right a *d*-wave one. Reprinted from [105].

This lead to an additional dependence in the expression of the  $\gamma$  complex function which now reads

$$\gamma(E, \theta) = \sqrt{\frac{E - \sqrt{E^2 - \Delta^2(\theta)}}{E + \sqrt{E^2 - \Delta^2(\theta)}}} \quad (4.22)$$

In order to compute the normalized conductance, one can use equation 4.20, where now both  $\tau_N$  and  $\Delta$  depend on  $\theta_N$  and  $\theta$ , respectively. Indeed, we point out

that the two angles are generally different and coincide only when  $k_x$  is directed along the perpendicular to the interface. Therefore, we define the difference between the two angular components as  $\alpha$ .

When  $\alpha = 0$ , the perpendicular to the interface is aligned with the "lobes" of the order parameter, meaning that both ELQ and HLQ see the gap with the same sign, i.e.,  $\Delta(\theta_N) = \Delta(-\theta_N)$  for any value of the angle, where the conductance curve changes with  $Z$  (fig: 4.13).

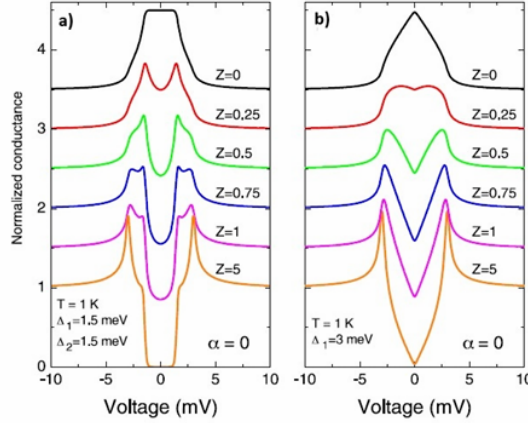


**Figure 4.13:** The picture shows different curves in the  $\alpha = 0$  case in the case of anisotropic  $s$ -wave gaps (a) and a  $d$ -wave gap symmetry. Reprinted from [105].

In the dual case, when  $\alpha \neq 0$ , defining the misalignment case, for some values of  $\theta_N$  the two order parameters assume different signs for ELQ and HLQ, leading to constructive interference phenomena between the two. This produces the appearance of a Zero Bias Conductance Peak (ZBCP) in the normalized conductance curve for  $\alpha, Z \neq 0$ . The peak is more pronounced as  $Z$  increases, reaching its maximum value for  $\alpha = \pi/4$  ( $\forall \theta_N$ ), i.e., when the perpendicular direction is aligned with the direction of the nodes (fig: 4.14).

#### 4.3.4 BTK multi-band model

The **multi-band BTK model** builds upon the 2D BTK model, attempting to generalize its key features. It serves as an approximation, allowing us to consider the total conductance as a weighted sum of the partial conductances associated with the different gaps. However, this is not strictly accurate, as it overlooks the real shape of the Fermi surface (which we assume to be spherical) and the gap values for each wavevector  $\mathbf{k}$ . Despite these limitations, the model proves quite useful for studying many materials, such as Fe-based superconductors.

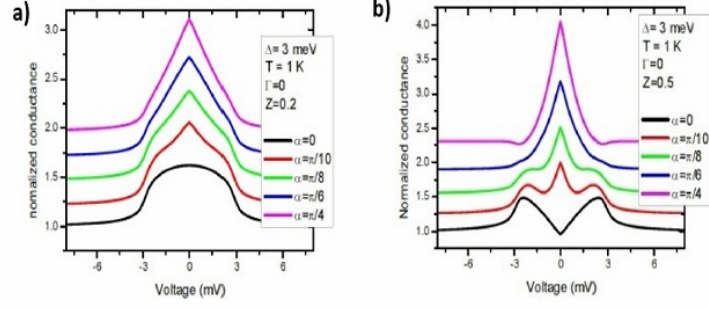


**Figure 4.14:** The figure shows the normalized conductance curve for two values of  $Z$  in a  $d$ -wave superconductor and the appearance of the ZBCP. Reprinted from [105].

The model involves computing the normalized conductance for each band using equation 4.20, which, for example, gives values  $G_1$  and  $G_2$  for bands 1 and 2. These values are then combined into the total conductance  $G$  through a weighted sum, yielding the normalized conductance at zero temperature:

$$G = \omega_1 G_1 + (1 - \omega_1) G_2 \quad (4.23)$$

with  $\omega_1$  the weight associated to the first band and  $(1 - \omega_1) = \omega_2$ , due to normalization condition, the weight associated to the second band. Again, in order to compute the conductance for temperatures different from zero, we need to perform the convolution with the specific Fermi function obtaining the set of parameter:  $(\Delta_i, \Gamma_i, Z_i, \omega_i)$  with  $i = 1, 2$ .

# Chapter 5

## Ionic gating and ion intercalation procedures

In the last decades, several methods have been studied, all of them aiming to modify some properties of the material in a suitable way, i.e. try to enhance the critical temperature of the superconductors. A good place is occupied by the **ionic gating** technique, and the different methods based upon it. In this chapter we are going to summarize the different techniques used in the past years including the recently-developed method of gate-driven protonation.

### 5.1 Ionic gating

The **ionic gating** technique is a well-known procedure that allows one to study and control the electrical charge transport and the electronic ground state in various materials. This is due to its intrinsic nature, which enables significant modulation of the surface charge density through the so-called **electric-double-layer field-effect transistor** (EDL-FET) architecture [111].

The **electric field effect** (EFE) can tune the surface conduction properties of different materials through the application of a transverse electrostatic field which is controlled by a gate electrode that is separated from the surface of the material by an electronically-insulating medium, leading to one of the most fundamental physical phenomena for semiconductor devices [112, 113]. Indeed, when a bias is applied to the *metal-insulator-semiconductor* (MIS) structure (fig. 5.1), a change in the concentration of carriers in the semiconductor layer is observed, leading to a significant modification in the conductivity of the material. This can be expressed as  $\sigma = qn\mu$ , where  $q$  represents the electric charge,  $n$  is the charge density, and  $\mu$  is the mobility of the charge carriers. If we recall that the **resistivity**  $\rho \propto 1/\sigma$ , it is clear that this procedure leads to an increase (or a decrease) in the resistivity. The

resistance variation strictly depends on the sign of the applied gate voltage and the position of the Fermi level. Indeed, this modification occurs when the free-carrier concentration is reduced due to the semiconductor depletion, which is induced by the application of a suitable gate bias. Therefore, when an inverse voltage is applied to the semiconductor (leading to the accumulation case), a strongly conducting channel of the opposite carrier type with respect to that of the bulk semiconductor material arises at the interface between the semiconductor and the insulator [112]. Based on these observations, the FE can be used as a gating mechanism, which, depending on the values of the applied gate voltages, allows the current-carrying properties of the layer to be altered, turning the semiconductor into a material that can be either highly conductive or resistive. In the first scenario, a current can flow through the layer, when a conducting channel at the SI interface is opened, whereas the source-drain current cannot flow if the gate bias shut down the conducting channel. With this in mind, a conducting channel can be opened and closed simply by modulating the applied gate bias. In fact, the MIS architecture can function as a gate that controls the current flow between two reservoirs of charge, externally connected to a circuit through ohmic contacts, representing the key point of the well-known **field-effect transistor** (FET) (fig. 5.1) [112]. When the insulating layer is an oxide, this device is known as a MOSFET (metal-oxide-semiconductor FET).

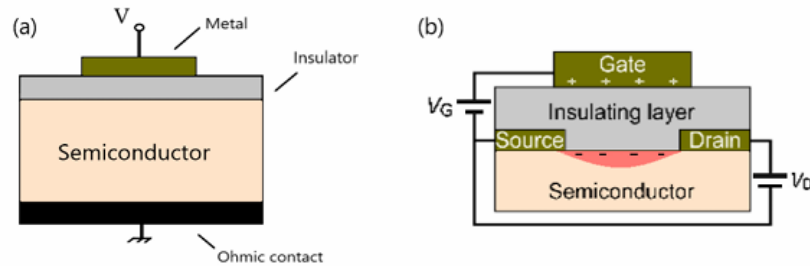


**Figure 5.1:** The picture show a schematic view of the the MIS structure before the gate bias application (a) and with gate voltage  $V_G \neq 0$  leading to the FET architecture. Reprinted from [114]

Together with electronic device applications, the FE procedure is used for a broad variety of purposes. In conventional FE gating techniques, solid gate dielectrics are usually implemented, inducing a relatively small surface charge. Therefore, its capability to induce phase changes in materials is severely limited, leading to the idea of finding different ways of doping the material, possibly based on an electrochemical concept that exploits the effect of a huge electric field. The solution

was thus to substitute the gate oxide with an electrolyte [115].

The use of an electrochemical transistor employs the MOSFET structure to obtain a more efficient modulation of the surface charge density on the materials through the use of an electrolyte as a gating medium instead of the insulator. Indeed, by applying a bias voltage between the gate electrode and the active channel of the transistor, solvated ions in the electrolyte move towards both electrodes following their charge polarity. Electrostatic fields are generated through the dense accumulation of ions on the surface of the channel, a phenomenon first described by von Helmholtz in 1853. When two conducting materials form an interface, they define an electric double layer (EDL), where one of the layers is characterized by an excess of surface charge, either positive or negative, while the other contains a surplus of opposite sign, imposing a balance between the two. Ions in the first layer are adsorbed onto the surface, also due to chemical reactions, whereas ions in the second layer are attracted due to the presence of the *Coulomb force*, which characterizes the interactions between particles [116]. When the electrolyte is highly concentrated, as in the case of **ionic liquids**, the thickness of the EDL is of the order of nanometers. The voltage drop is localized within the EDL itself, while the electric field induced can be very high ( $\gtrsim 10$  MV/cm) [114, 116]. With these values of electric field, the EDL gating also depends on the density of states of the sample and the electrochemical stability window of the electrolyte itself, leading to a maximum charge density accumulation of up to  $10^{14} - 10^{15}$  cm<sup>-2</sup>, much higher than that provided by solid gate dielectrics [116]. In these conditions, we refer to this structure as the **EDL-FET** [116, 117], as depicted in figure 5.2.

However, gating dynamics and effectiveness depend strongly on the properties of the electrolytes used. Among all the possibilities, **ionic liquids** (ILs) have shown some of the best performances and easy practical application as gate materials in the realization of FET-based devices.

Ionic liquids are molten organic salts or eutectic mixtures of both organic and inorganic salts, generally characterized by a melting point or glass-transition temperature lower than 373 K [119, 120]. They are composed of organic and/or inorganic ions. Moreover, their non-isotropic intrinsic character arises from their strong electrostatic and dispersive interactions at different scales, while also exhibiting high thermal and chemical stability, along with non-volatility and non-toxicity. Since they remain in a fluid state over a wide temperature range, they can be exposed to higher voltages than the ones applied on solid electrolytes, without undergoing oxidation processes, thanks to their large electrochemical windows (i.e the applied voltage value at which the ionic dissociation starts). Therefore, one of the crucial parameters determining the specific choice of IL is the **specific capacitance**, which determines the number of carriers that can be induced in the conducting channel of the FET when a specific voltage is applied. Indeed, the

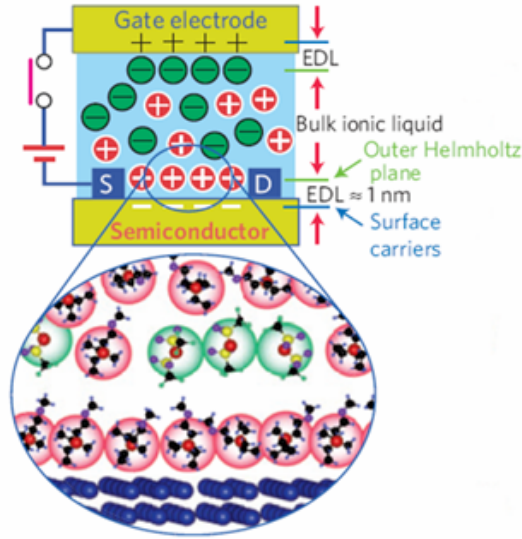


**Figure 5.2:** Zoom on the interface between the ionic liquid and semiconductor in a general EDL-FET structure. Reprinted from [118].

accumulated charge  $Q$  in a parallel-plate capacitor is given by the simple relation

$$Q = CV \quad (5.1)$$

where  $C$  is the capacitance and  $V$  the applied voltage. It's obvious to observe that higher is the value of the capacitance the same is for the quantity of charge induced in the system. In particular one has

$$C = \frac{\epsilon_0 \epsilon_r A}{d} \quad (5.2)$$

which depends on the geometry of the capacitor itself, area and plate distance, and on the permittivities of the vacuum and of a specific medium. Even though the  $\epsilon_r$  values of ionic liquids range from about 1 to 10, they are still able to produce an excess capacitance on the order of  $10 \mu F cm^{-2}$ , thanks to the formation of electric double layers (EDLs) at the interfaces with a thickness of the order of 1 nm, which can operate up to moderately high frequencies up to few MHz [120].

In conclusion, we observe that by exploiting the potential of ionic gating, within the electrostatic limit—which implies that no electrochemical interactions occur at the electrolyte/electrode interface, so that the induced charge density must be confined to the surface of the material under ultrahigh electric fields—one can control the surface transport properties of a wide variety of materials. These materials include metal chalcogenides and 2D materials, and this technique can

potentially modify the properties of the compounds themselves, ranging from structural modifications to critical temperature shifts in superconductors.

## 5.2 Ion intercalation

The properties of layered materials can be modified through the process of **ion intercalation**, which involves the controlled insertion of ions into the crystal lattice of the host material. During intercalation, the ions are typically injected within the interlayer spaces, forming a chemical bond with the original atoms, which alters the material's unique properties [121]. This ion positioning typically leads to a weaker coupling between atoms, increasing the distances between them and, in turn, directly affecting various material properties (fig. 5.3).

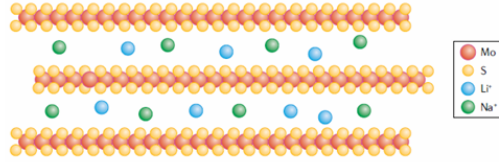


**Figure 5.3:** Pictorial scheme about the ion intercalation of  $Li^+$  and  $Na^+$  in a layered material such as  $MoS_2$ . Reprinted from [121].

The technique can be performed using element doping methods as well as ion-beam implantation, but it is not without drawbacks. Indeed, this can lead to the formation of dopant clusters (in the doping method) or localization only on the surface of the material (in the ion-beam case). In this context, the use of ionic liquid (IL) as an electrolyte for gating technique remains a good alternative to other conventional ion intercalation methods, especially when the material is a thin film, which is dominated by surface properties.

Although the first studies were conducted in the early 2000s, significant experimental evidence has been gathered in the last few decades. In 2017, Lu et al. [122] focused on the evolution of single ionic species ( $Li^+$ ,  $K^+$ ,  $H^+$ ,  $O^{2-}$ ) without delving deeply into their effects on the gated material. However, other important insights are obtained by studying the layered semiconductor  $MoS_2$  intercalated with  $Li^+$  and  $K^+$ . It was found that using different electrolytes in the same material led to a wide variety of phases [121]. Specifically, the system underwent an *insulator-to-metal-to-superconductor* phase transition when doped with  $Li^+$ , in stark contrast to the  $K^+$  doping, which induced distortions and defects throughout the material.

### 5.3 Protonation

The ion intercalation can be performed also through the insertion of  $H^+$  denoting the **protonation** (or hydrogenation) process.

Let us consider a system which is ready to be intercalated using IL as an electrolyte, with a well defined electrochemical window. Given that voltage value it releases hydrogen and oxygen ions. If the gating procedure is performed under ambient conditions, applying a negative gate bias can drive the negatively charged  $O^{2-}$  ions into the films, thereby controlling the oxygen vacancies. On the other hand, applying a positive gate bias leads to the splitting of water into two ionic components,  $OH^-$  and  $H^+$ , with the latter being driven into the material and intercalated into the structure (fig: 5.4).

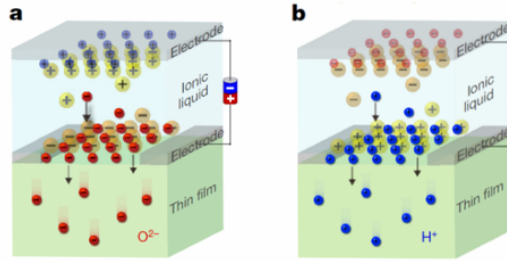


**Figure 5.4:** Schematic view of the two kind of applied voltage which leads to the oxygen (a) and hydrogen (b) intercalation. Reprinted from [122]

One can observe the intercalation via **X-ray diffraction (XRD)** analyses [122], which highlight the presence of ions due to shifts in the diffraction peaks, linked to the increase in interlayer spacing induced by intercalation [123]. Moreover, experimental evidence shows that ILG-induced phase transformation can occur with different ionic liquids, which need to have sufficient residual water to achieve the phase transformation [122]. The XRD analysis is fundamental both *in situ* and *ex situ*, as it confirms the non-volatility of the transformation. This provides an important consequence: when intercalation is successful, the  $H^+$  ions can be non-volatile, allowing for post-gating measurements [3].

Experiments involving ionic liquids have been widely used in transition metal oxides, showing a reversible tuning of the concentration of oxygen and hydrogen ions through the application of voltages of different signs. Furthermore, electric-field controlled phase transformations can also occur along with the modulation of optical and magnetic properties [122]. However, intercalation alters the carrier density, which in turn modifies the electrical transport measurements, an important consideration for verifying post-gating treatment modifications.

This approach is particularly useful and powerful when applied to high- $T_C$

superconductors, with the aim of modifying their superconducting properties, such as the critical temperature, of the compound. In 2018, Cui et al. [124] applied this method to iron (Fe)-based superconductors, particularly focusing on  $FeSe_{1-x}S_x$  and  $BaFe_2As_2$ . The intercalation of  $H^+$  in bulk crystals induces superconductivity in the second compound while increasing the superconducting transition temperature on the first one, through the electron doping effect. Just one year later, under optimized protonation conditions—defined by a protonation temperature of 350 K, improving proton diffusion efficiency in the crystal with a gating period of 12 days during which water is completely dissociated—an enhancement of the superconducting volume ratio was observed [3].

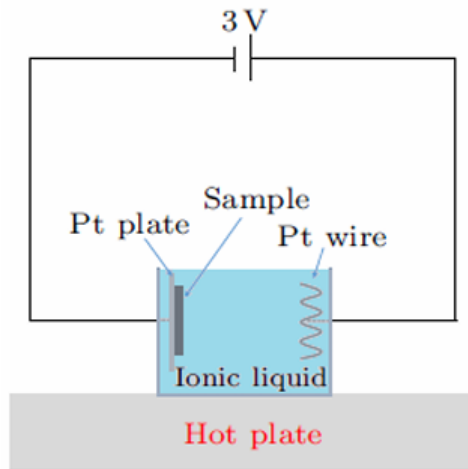


**Figure 5.5:** Schematic experimental setup used by Cui’s group in [3]

They discovered that  $FeSe_{0.93}S_{0.07}$ , under these protonation conditions, exhibits a single high- $T_C$  phase with a superconducting transition temperature of  $T_C = 43.5$  K [3]. The superconducting properties were determined through magnetization measurements as well as transport measurements. In fact, panel 5.6 illustrates how the resistance of the material changes as a function of temperature after the protonation procedure in  $FeSe_{0.93}S_{0.07}$  single crystals. Furthermore, the presence of intercalated protons in the lattice can be confirmed through proton *nuclear magnetic resonance* (NMR), enabling direct probing of the hydrogen’s presence.

In 2022, Meng et al. [125, 126] investigated on protonated  $FeSe$ , observing discrete superconducting (SC) phases in  $H_x-FeSe$  single crystals. Through protonation and deprotonation stages, they found a maximum critical temperature of 44 K. The crystalline structure of  $H_x-FeSe$  remained unaffected by the protonation process, suggesting that the discrete SC phases are intrinsic and directly related to carrier concentration. This implies that the  $FeSe$  interlayer spacing is not fundamental in determining the high  $T_C$ , and the superconducting phase transition

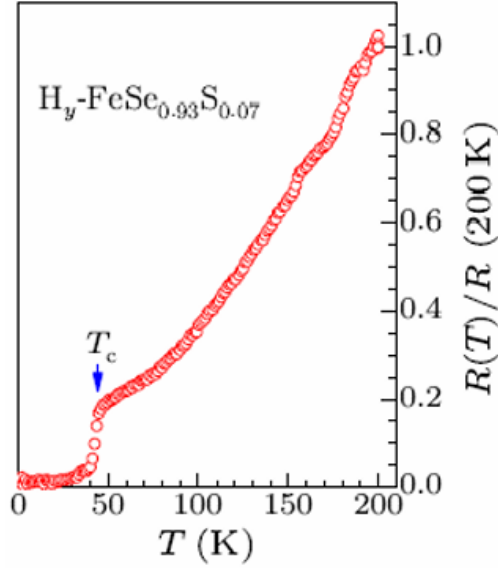


**Figure 5.6:** Resistance as a function of temperature of  $FeSe_{0.93}S_{0.07}$  compound post protonation technique. Reprinted from [3]

can be explained by a **Lifshitz transition**, that is an abrupt change in the Fermi surface topology [125]. The protonated  $FeSe$  compound was not only marked by an enhancement of the critical temperature but also by an increase in the critical current density, enabling wide technological applications [126]. The optimized protonation conditions allow compounds to alter their critical temperature or, better, to achieve a superconducting phase transition, as shown in table (5.1).

Meanwhile, along with the studies on the intercalation of Fe-based superconductors, several new materials exhibiting a superconducting phase transition were discovered through simple intercalation of organic compounds. This is the case for **tetrabutylammonium** ( $TBA^+$ ) and **cetyl-trimethylammonium** ( $CTA^+$ ), which were intercalated into  $FeSe$  through electrochemical intercalation techniques [127, 128]. They found that both compounds,  $(CTA)_{0.3}FeSe$  and  $(TBA)_{0.3}FeSe$ , exhibit a superconducting phase transition at  $T_C = 45$  K and  $T_C = 50$  K, respectively, both at ambient pressure. Particularly, electron doping of the  $FeSe$  plane, coupled with minimal interaction between atoms and organic ions, reduces impurity phases and disorder in the  $FeSe$  plane.

The gate-driven hydrogen intercalation process has been shown to be highly impactful on other types of materials as well, such as transition metal dichalcogenide compounds. Indeed, it has been demonstrated that a superconducting phase transition can be induced in  $TiSe_2$  under specific protonation conditions, which

Compound	$FeSe$	$FeSe_{0.93}S_{0.07}$	$ZrNCl$	$1T-TaS_2$	$Bi_2Se_3$
$T_{c,before}$	9 K	8 K	0	0	0
$T_{c,after}$	41 K	43.5 K	15 K	7.2 K	3.8 K

**Table 5.1:** Summary of the effect of protonation in different materials: some of them are able to achieve a superconducting state with modest value of  $T_C$  [3].

are primarily related to the duration of the process and the applied gate voltage value [2].

Despite these important findings, most of these Fe-based compounds are not very stable in the atmosphere, exhibiting degradation back to the pristine state, which results in a decrease in the critical temperature value (as observed in the case of FeSeS [124]). However, some differences can be highlighted between the organic and inorganic intercalation cases. In particular, it has been observed that the group with organic-intercalated  $FeSe$  [129] requires a higher gate bias than the hydrogen-intercalated one [125, 126] to achieve significant changes. Moreover, the difference between the two groups can also be seen from a structural point of view. The organic-intercalated compound shows a swollen crystal lattice due to a large increase in the interlayer distance induced by the atomic size of the cations, which are larger than the  $H^+$  ions [125, 126].

In conclusion, based on these results, one might be interested in analyzing the effect of gate-driven  $H^+$  intercalation in other materials, in order to capture new features and behaviors. With this in mind, we performed this procedure on the  $Fe(Se, Te)$  compound, and the results are presented in the following chapters.

# Chapter 6

## Materials and methods

### 6.1 $Fe(Se,Te)$ properties

This thesis aims to investigate the transport properties of  $Fe(Se_{0.5},Te_{0.5})$  thin films in both their pristine and protonated states. The primary objective is to explore the modification of the compound's superconducting behavior through gate-driven hydrogen ion intercalation ( $H^+$ ). As discussed in Chapter 5, this procedure has demonstrated the potential to enhance the critical temperature of the material, potentially opening avenues for achieving room-temperature superconductivity. Additionally, point-contact measurements were performed using PC technique (and soft-PC as well) to access the structure of the superconducting gap of the material and probe its possible topological properties [88, 90].

#### 6.1.1 Sample growth

The films were provided by the group of Professor Kazumasa Iida from Nihon University (Japan). The films were grown by pulsed laser deposition using a KrF excimer laser (wavelength 248 nm) and a  $Fe(Se_{1-x}Te_x)$  target placed over of a  $CeO_2/YSZ$  substrate.

#### Pulsed Laser Deposition (PLD)

Pulsed laser deposition (PLD) is a highly effective technique for depositing thin films with precise control over their composition and structure. A high-power pulsed laser, often an excimer laser such as  $Nd:YAG$  or  $KrF$  at 248 nm, is used to irradiate the target material in either a vacuum or a controlled atmosphere. The laser beam focuses on the surface of a solid target, causing its evaporation into a plasma phase that contains particles ejected from the compound. These particles expand perpendicularly to the target surface and deposit onto a substrate (e.g.,

$CaF_2$  or  $CeO_2/YSZ$ ), whose temperature can be controlled to enhance adhesion and crystallinity.

PLD can be applied to a wide variety of materials, including metals and superconductors, while preserving the compound's composition due to the congruent evaporation during ablation. Among its advantages is the ability to precisely tune the film thickness and construct multilayer heterostructures.

### Properties of $CeO_2/YSZ$

Cerium dioxide and yttria-stabilized zirconia ( $CeO_2/YSZ$ ) is a composite substrate commonly used in thin-film deposition, especially for high-temperature superconductors. YSZ is known for its high chemical stability and excellent mechanical strength. Importantly, it has low electrical conductivity, an important feature for resistivity measurements.

$CeO_2$  serves as a buffer layer between the YSZ substrate and the film, providing good lattice compatibility with most superconducting materials. The  $CeO_2/YSZ$  system combines the properties of both materials to create a crystallographically compatible surface for superconducting films, which often require a well-defined orientation to optimize their properties. Furthermore, the  $CeO_2$  layer acts as a barrier to prevent the diffusion of chemical species between the film and the substrate. The quality of the  $CeO_2$  layer's deposition is crucial, as defects in this layer can compromise the epitaxial growth of the superconducting film.

## 6.2 Sample mounting

The mounting of the sample varies depending on the type of measurement to be performed and the equipment used. Specifically, the experimental setup differs depending on whether the sample must be mounted in the sample chamber of a cryogenic insert for a top-loading cryostat, or on the *cold finger* of a bottom-loading pulse-tube cryocooler. In my study, in the first case, the sample must be mounted in a vertical position, whereas in the second one, it is mounted horizontally. In the following sections, I will explain the basics of resistivity measurement and describe the different mounting configurations.

### 6.2.1 Resistivity measurement

As discussed in the previous chapter (1), electrical resistivity is an intrinsic macroscopic property that provides insights into the microscopic mechanisms governing the transport of electric charge in a material. Additionally, a sharp drop in resistivity at a specific critical temperature, which varies for each material, indicates the transition to a superconductive state. In my case, the samples have very small dimensions, making the measurement of resistivity a challenging task.

The electrical resistance ( $R$ ) of a material is defined using **Ohm's law**:

$$R = \frac{V}{I} \quad (6.1)$$

where  $V$  is the applied voltage and  $I$  is the electric current. If the resistance remains constant over a significant voltage range, Equation (6.1) can be used to predict the material's behavior. Resistance is directly related to the resistivity of the material through the equation:

$$\rho = R \cdot \frac{A}{L} \quad (6.2)$$

Here,  $A$  and  $L$  represent the geometry of the sample, corresponding to its cross-sectional area and length, respectively. However, equation (6.2) holds for the collinear configuration, which is the one used in this work. This configuration consists of placing two current electrodes on opposite sides of the sample (defining the *channel length*), through which the drain-source current ( $I_{DS}$  black solid line in figure 6.1) can flow. Along this *channel*, we have two (or more, depending on the geometry) voltage electrodes (red solid line in figure 6.1), which must be much smaller than the current electrodes. Through these, we measure the voltage drop along the current flow, whose value is controlled, allowing us to determine the resistance (see fig. 6.1).

A nanovoltmeter is used to measure the voltage drop across the sample, while a current generator induces a current flow through it. For our samples, the typical current is in the range of 1 to 10  $\mu A$ . Using Equation (6.2) and the known geometric dimensions of the sample, the resistance (and thus, the resistivity) can be determined. Therefore, recording the  $I$ - $V$  characteristics we can compute the sample's resistance as a function of variables such as time, gate voltage, or temperature.

One challenge lies in the fact that the electrical leads connecting measurement the instruments to the sample often have a higher resistance than the sample itself. This can lead to an higher resistance value, with respect to the real sample one. To address this, a four-wire configuration is employed (figure 6.2). This technique effectively eliminates systematic errors caused by the resistance of the leads and contact resistances, which can compromise the measurement accuracy.

The key advantage of the four-wire configuration is the physical separation of the circuit carrying the current from the one measuring the voltage drop across the sample. This separation ensures that the resistance of the wires and contacts becomes negligible in the measurement. Additionally, it is crucial that the voltage contacts do not overlap with the current contacts. Overlapping contacts would lead to inaccurate measurements because the measured voltage would include the voltage drop across the current contacts.

Furthermore, the voltage contacts should be placed as far apart as possible to minimize the influence of uncertainties in the contact width relative to the total



**Figure 6.1:** *Example of  $Fe(Se,Te)$  mounting. We can see the G.E. Varnish in the background, on top the sample with the Ag-spots. The black arrow define the flow of the drain-source current ( $I_{DS}$ ), while the red arrow indicates the voltage drop between two electrodes*

distance between them. This setup ensures the accuracy and reliability of the resistivity measurements.

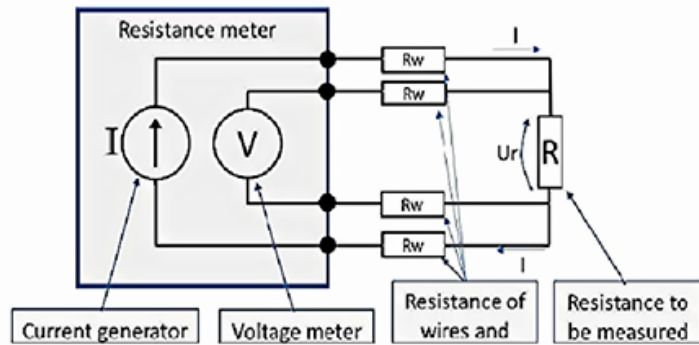


**Figure 6.2:** *The panel shows the theoretical configuration of the 4-wire technique. Reprinted from [130].*

## 6.2.2 Horizontal setup

This setup is used for measurements carried out in the bottom-loading dry cryostat, where the cooling system is a Cryomech pulse-tube cryocooler. The standard

sample configuration in this setup would be a direct vertical connection to the *cold finger* of the cryostat. The presence of the liquid electrolyte on top of the sample would however result in the electrolyte flowing off the sample during the gating process. As a consequence, a suitable sample holder had to be employed to allow keeping the sample and its electrochemical cell in horizontal configuration during the all measurement runs. Such sample holder was realized as follows.

The first step is to provide the sample with a support, which consists of a *pool* made from **Loctite Stycast**. Stycast is a two-component, thermally conductive epoxy encapsulant designed for electronic and electrical applications, as well as environmental protection. It is characterized by good thermal conductivity, excellent heat dissipation, chemical resistance, and physical strength, along with crucial electrical insulation properties. We molded the compound into a box-like structure (referred to as a "*pool*") and cured it under an infrared lamp for several hours. After curing, the *pool* exhibits complete electrical insulation and significant hardness.

The sample is then glued to the *pool* using **G.E. Varnish**, a phenolic resin-based adhesive commonly used in cryogenics for its excellent electrical insulation and high thermal conductivity when fully cured. Additionally, as we will see later, G.E. Varnish is used to lacquer the leads and contacts on the sample, creating an insulating layer that prevents direct contact between them and the electrolyte.

Once the layer beneath the sample is cured, securing it firmly to the *pool*, the next step is to fill the *pool* with G.E. Varnish. The gate electrode (a platinum electrode in this case) is then positioned on the side of the sample at the same height. This electrode is required to allow applying the gate potential during the ionic gate-driven protonation process.

Finally, the Stycast *pool* is attached to a support called the *L-holder*, located between the two contact boards. The *L-holder* ensures the sample is positioned horizontally when mounted on the cryocooler (see figure 6.3).

The electrical contacts are established through a two-step wiring process. First, the contact board is connected to the boundary of the *pool* using *Au/Pt* wires with a diameter of 25  $\mu\text{m}$ . Each contact board has four electrodes realized with Sn soldered onto copper, with an In layer on top. The gold wire is secured in the In block exploiting its malleability at room temperature, forming an electrical connection between the *pool* and each of the electrodes.

The second step involves connecting the *pool* to the sample using Pt wires with diameters of 25 or 50  $\mu\text{m}$ . These wires are anchored to the sample surface using **silver conductive paint**, an electrically conductive adhesive. The silver spots must be as small as possible for precise measurements, though the current contacts need to be wider than the voltage contacts (see figure 6.1).

For point-contact measurements, the voltage contact setup requires modifications. In the soft-PC technique (see section 4.1.2), the contact is secured with an Ag spot on the sample surface. The size of the silver spot is critical for accurate

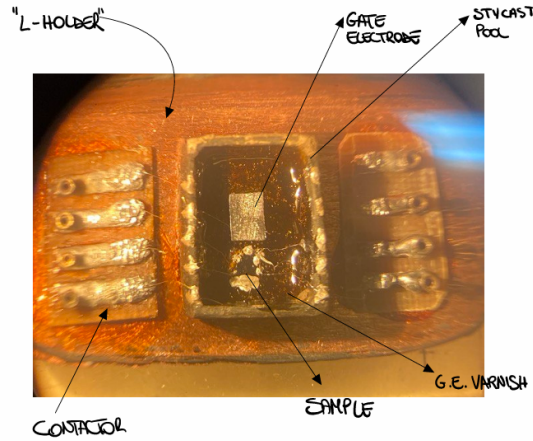


**Figure 6.3:** Representation of a complete horizontal mounting of the sample. The system is now ready for cryogenic measurements.

measurements: it must be as small as possible to ensure reliability but sufficiently large to mechanically secure the wire during thermal fluctuations.

The ionic gate-driven hydrogen intercalation process necessitates additional adjustments to the experimental setup. A layer of G.E. Varnish is applied first to cover the contacts, and second to forming a slight *dam* that is raised around the sample's surface. This barrier simultaneously prevents direct contact between the reactive Ag spots and the electrolyte, and spatially contains the droplet of ionic liquid used in the protonation process.

The liquid employed for this purpose is a **deep eutectic solvent** (DES), an emerging class of environmentally friendly solvents related to ionic liquids. For this study, we used a mixture of **choline chloride and glycerol**, in 1:3 ratio (referred henceforth simply as DES), to perform ionic gating.

The choice of this DES is due to several physical properties that facilitate an optimal protonation process. Indeed, it is characterized by a high proton density, which can be readily exploited for intercalation. Additionally, its low viscosity is important, as it improves the homogeneity of the hydrogen transfer.

Moreover, the key advantage lies in its large electrochemical window, which prevents electrochemical processes that do not involve the release of  $H^+$  ions, forming with a low threshold voltage. Furthermore, the DES remains in a liquid state over a wide temperature range, both above and below room temperature, allowing for an optimized protonation process [131].

Therefore, DES is applied to both the gate and the sample, confined within the G.E. Varnish *dam*. The ionic dissociation of the liquid enables the intercalation of hydrogen ions into the  $Fe(Se, Te)$  sample.

Once the setup is complete, the *L-holder* is attached to the *cold finger* of the

cryocooler, and the electrodes on the contact board are connected (fig. 6.3). Proper connection is essential for accurate signal analysis through LabVIEW.

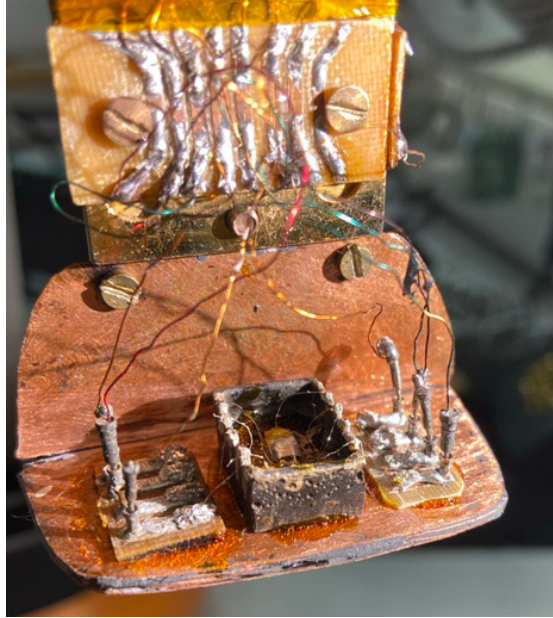


**Figure 6.4:** Complete mounting of the sample on the cold finger of the pulse-tube cryocooler.

As shown in Figure 6.4, the electrodes are connected using copper wires, with the terminal parts designed to be plugged into the female spring-loaded connectors soldered to the contact boards.

With this setup, the system is now ready to perform the gate-driven protonation process and be cooled to low temperatures to study the superconducting properties of the sample.

### 6.2.3 Vertical setup

This setup is used for measurements carried out by mounting the sample in on the cryogenic insert of the Oxford top-loading wet cryostat, where the cooling power is provided by the evaporation of liquid He in the variable-temperature insert (VTI). In this case, the gate-driven protonation process can be performed before the insert is inserted in the VTI: the insert can thus be placed horizontally during the process and quickly cooled below the melting point of the DES after its completion, eliminating the need of the L-holder to prevent DES flow-off. However, the practical electrical connections of the  $Fe(Se, Te)$  films remain the same as in the previous case, with the stycast *pool* now surrounded by an additional structure.

In this setup, a small copper container prevents the dispersion of the ionic liquid and contamination of the cryostat. The DES is characterized by significant surface tension, which plays a critical role during the cooling process. Before the ionic liquid freezes, its strong adhesion to the surface, combined with the dam-like structure built on top of the material, keeps the droplet well-confined on the film, enabling the protonation technique.



**Figure 6.5:** *Sample chamber of the cryogenic insert used in the Oxford top-loading wet cryostat. Here, the sample was prepared for soft-point contact measurement, so the pool was not necessary.*

To complete the mounting, the sample needs to be enclosed under a **kapton** foil. This serves the purpose of catching any residual spillage of the DES and preventing contamination of the entire cooling machine.

When performing point contact measurements, in general, the copper structure is replaced by a simple sample holder to which the film is glued. This holder consists of a conductive copper layer, which is used to create the electrical contacts, and a fiberglass layer that ensures electrical insulation for the system. A practical example is shown in figure 6.6, which illustrates the three steps involved in creating the support. This is also useful for pristine transport measurements. However, for Soft-PC measurements, the contact on the sample must be adjusted as discussed

in section (4.1.2) (fig: 6.5).

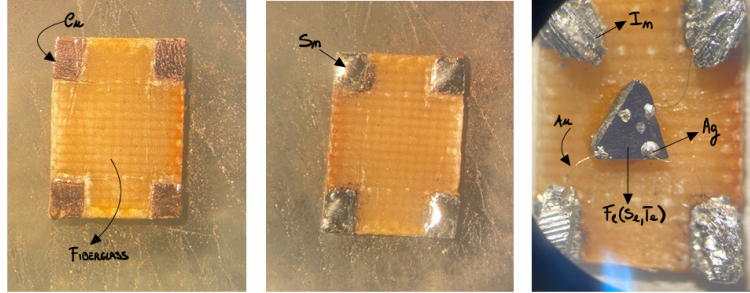


**Figure 6.6:** On the left, we can see the fiberglass base with the four purpose-designed angles, where a copper layer is still present to ensure electrical conductivity. In the central panel, the four angles are welded with tin, on top of which indium can also be welded. The last panel shows the complete mounting of the sample on the support, ready to be glued to the descendant.

## 6.3 Cooling systems

One of the two main goals of this thesis was to compare the pristine  $Fe(Se,Te)$  film with the intercalated one, aiming to observe any critical temperature shift and possibly detect changes in the structure of the superconducting gap. In this regard, we need to examine the properties of the compound by varying the temperature. Therefore, the resistance is measured as a function of temperature, ranging from room temperature down to temperatures close to absolute zero ( $1.6\text{ K} \div 4.5\text{ K}$ ). The minimum temperature reached depends on the cryostat used for the measurement. In this section, we will discuss the operational principles of the cryostats employed during these measurements.

### 6.3.1 Pulse-tube cryocooler

About half of the measurements were performed in a Cryomech bottom-loading dry cryostat where the cooling power was obtained using a **pulse-tube cryocooler**. The sample is placed inside an optically and thermally shielded chamber, which is anchored to the cryocooler's *cold finger* using screws (fig: 6.7) or simply inserted by means of the descendant. Therefore, wires enable the electrical connections necessary for measuring the sample's transport properties. Among these wires one is dedicated to applying the gate voltage,  $V_G$ , crucial for the protonation process *in situ*. This setup allows for tracking the resistance behavior as a function of both the applied voltage and temperature.

The instruments are interfaced with a computer running LabVIEW software, which helps to process the measurements. Through the program, parameters such as the gate voltage ramp for protonation or the  $I_{DS}$  (drain-source current which flows between the current electrodes) current can be precisely adjusted, enabling controlled experiments.

The electrical wiring of this cryostat allow simultaneous measurement of two independent voltage drops (*channels*) on a single sample. This is achieved using the collinear configuration.

Before the cooling process begins, it is essential to achieve a sufficient vacuum level. A combination of a rotary pump and a turbomolecular vacuum pump is used to create a vacuum environment of approximately  $5 \times 10^{-3}$  mbar. Only after reaching this level can cooling commence. Maintaining a vacuum is critical to prevent ice formation inside the chamber, which could compromise measurement accuracy. Additionally, in cases where the sample is sensitive to atmospheric conditions, a controlled environment is necessary to ensure reliable results.

The technology of pulse-tube cryocoolers is based on periodic (pulsed) phases of subsequent pressurization and expansion of a gas at a frequency of  $\sim 1$  Hz. Usually, the gas involved in the refrigeration process is  $^4He$ , and these phases correspond to heat exchange between the gas and the environment. The behavior of the  $^4He$  is well approximated by the thermodynamic Stirling cycle.

In a very simplified way, the compression pulses correspond to a release of heat,  $Q_H$ , to a heat exchanger at a constant temperature, while the expansion pulses correspond to the absorption of heat,  $Q_C$ , from a heat exchanger at a constant low temperature, i.e., the temperature that we want to reach in the cold finger. Then, the gas passes through a regenerative heat exchanger that stores a certain amount of heat and releases it in the next cycle.

### 6.3.2 Wet cryostat

All other temperature-dependent electric transport measurements were performed in an Oxford top-loading wet cryostat. Unlike in dry cryostats, where a closed refrigeration cycle is used as a source of cooling power, in wet cryostats this is provided by the flow and/or evaporation of suitable cryogenic fluids.

In my case, the cryogenic fluid used is liquid **helium**, which is the most commonly used substance for low-temperature analysis, between 77 K and 1.5 K. This is due to its intrinsic properties, namely **latent heat of evaporation** and **vapor pressure**. These properties are closely connected to the amount of heat exchanged over time, and they describe a nonlinear relation:

$$\frac{dQ}{dt} = Lp_{vap} \propto e^{-1/T} \quad (6.3)$$



**Figure 6.7:** *The figure shows the vertical setup, ready to be closed by the metal shield, which prevents thermal fluctuations during the measurement. At the bottom, we can see the thermometer, which is typically linked through G.E. Varnish behind the sample's copper support.*

The minimum temperature reached depends on whether  $^3\text{He}$  or  $^4\text{He}$  is used, as both exhibit completely different behaviors compared to classic liquids. Liquid helium, in particular, is a **quantum liquid**, characterized by a latent heat of evaporation that is one third of the value of corresponding classical liquids (fig. 6.8). Moreover, baths of liquid helium have relatively low cooling power because they evaporate very easily. For this reason, they require efficient heat shields to effectively separate the bath from the external environment.

However, the core of the refrigerant system is the vapor itself, which is pumped to achieve the lowest possible temperature. Modern cryocoolers typically use a **needle valve**, which can be manually controlled. This valve can be progressively opened or closed, adjusting the impedance of the helium flow, thus enabling the system to reach very low temperatures.

The cooling phase relies on the enthalpy of the gas produced by the evaporation of liquid helium, which implies a significant consumption of liquid helium. This can be problematic, as liquid helium is both rare and expensive, with  $^3\text{He}$  being more expensive than  $^4\text{He}$ . As a consequence, wet cryostats are usually operated together with a recondensing unit to mitigate the issue.

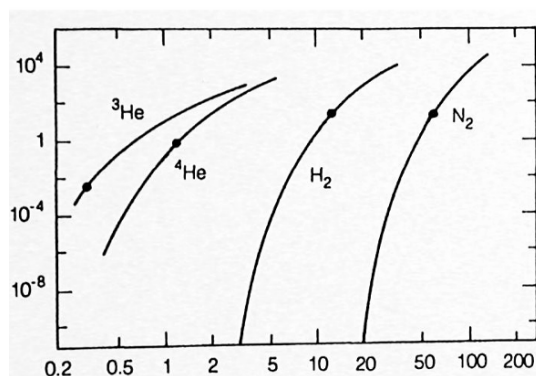


**Figure 6.8:** Vapour pressure of various cryoliquids. The horizontal axis measures temperature, while the vertical axis represents the vapour pressure. Reprinted from [132].

### Helium recondenser.

A helium recondenser is a closed-cycle refrigerator which is used to cool down a capillary tube in which warm He gas flows and is cooled back to its boiling point. In the case of the Oxford cryostat, the recondensing unit's cooling power is provided by a Cryomech pulse-tube cryocooler similar to the one used in the bottom-loading dry cryostat. The inlet of the recondenser is connected to the exhaust of the main bath of the cryostat whereas the outlet of the recondenser is connected to one of the transfer ports of the main bath. The role of the recondenser is to collect the He vapor boil-off from the main bath (which evaporates simply to keep the bath and cryostat to 4.2 K) and regenerate it thanks to the cooling power of the cryocooler, and reintroduce the reliquified He back into the bath, ready for the next refrigeration cycle (fig. 6.9). This process significantly reduces gas waste, allowing the research group to perform measurements for about three months with the same helium load.

### Vacuum techniques.

Most compounds are sensitive to the atmosphere, which is why experiments are typically conducted under vacuum conditions. Additionally, maintaining vacuum is necessary to prevent ice formation within the cavity or chamber where the sample is placed. Moreover, the vacuum condition is crucial in cryogenic. Indeed, in order to perform optimal cooling processes one have to grant a good vacuum condition.

Therefore, vacuum can be categorized into three regions based on the pressure levels:

- **Low vacuum:** From atmospheric pressure down to approximately  $10^{-2}$  mbar.
- **High vacuum:** From  $10^{-2}$  mbar to  $10^{-6}$  mbar.



**Figure 6.9:** *The figure shows the LaTEST 1 cryocooler, integrated with the recondenser. Here, the descendant was inserted for point-contact measurements.*

- **Ultrahigh vacuum:** Below  $10^{-6}$  mbar.

The instruments used for this experimental work either need low or high vacuum conditions, depending on the use of the bottom-loading or the top-loading respectively. Indeed, for the bottom-loading cryocooler this is accomplished through the use of two vacuum pumps that operate synergistically, one following the other (fig. 6.10).

The first pump is a *rotary vane pump*, which creates a good low vacuum by rotating the rotors. The rotation is synchronized by gears to avoid contact, with no oil used to seal the gap between the rotors. Following the booster pump is the second pump, a *turbomolecular pump*, which is responsible for achieving high vacuum conditions. To ensure optimal performance, the turbomolecular pump requires a pre-existing low vacuum. If the chamber is not pre-pumped, the turbo pump can overheat and become damaged.



**Figure 6.10:** *The image shows, on the left, the booster pump, responsible for maintaining low vacuum conditions, and on the right, the turbo pump, which is tasked with achieving high vacuum.*

# Chapter 7

## Experimental results

The key point of this thesis is to study and characterize the superconducting phases of  $FeSe_{0.5}Te_{0.5}$  compounds before and after ionic liquid gate-driven protonation. The primary objective is to identify any changes in its electrical behavior, particularly in its superconducting transition, by applying different values of gate voltage. To this end, we first thoroughly describe the pristine case, highlighting the resistivity measurements as a function of temperature. Additionally, we perform point-contact measurements to investigate the potential topological character present in the superconductor and also to characterize the structure of the superconducting gap of the sample. Indeed, preliminary measurements have been done by Professor Kazumasa Iida, which gently provides us the samples. Figure 7.1 shows their results.

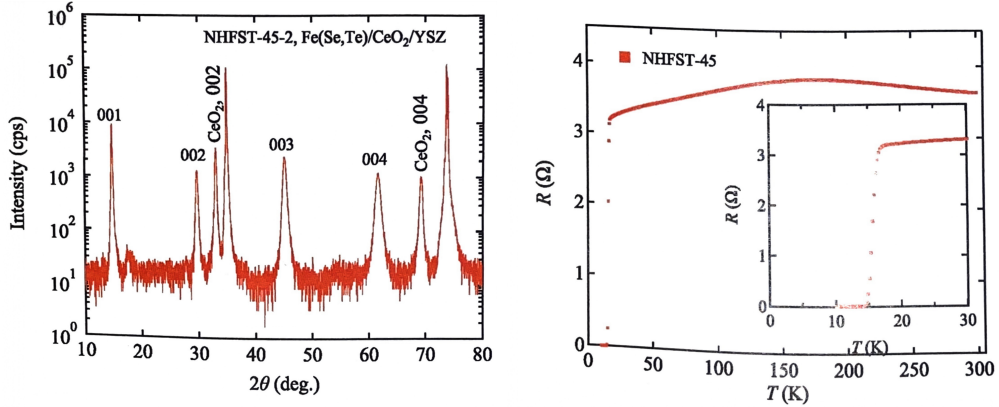


**Figure 7.1:** X-Rays spectrum and transport measurements performed by Professor Kazumasa on  $Fe(Se_{0.5}Te_{0.5})$ .

Following the study on the pristine compound, we focus on the protonated samples, whose characteristics are assessed after the application of a gate bias

using an electrolyte droplet placed over the sample. Our goal is to enhance the superconducting transition temperature and, similarly, perform point-contact measurements for comparison with the pristine case.

## 7.1 Measurements in pristine $Fe_{1+\delta}(Se_{0.5}Te_{0.5})$

### 7.1.1 AFM Measurements

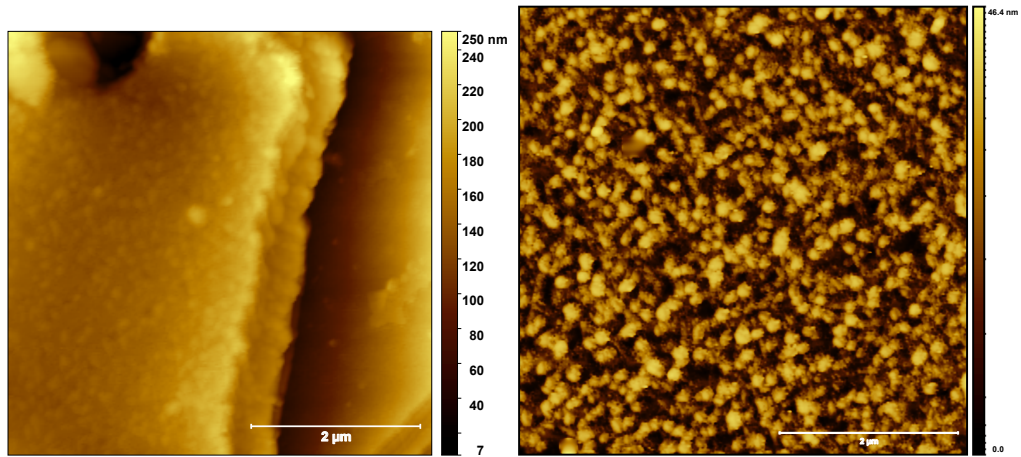


**Figure 7.2:** The left panel shows a two-dimensional AFM image that illustrates a region of the sample used for the analysis. The right panel exhibits the AFM image which highlights the grain boundaries of the film.

The material under study is the  $Fe(Se_{0.5}Te_{0.5})$  thin film. While the geometry of the samples varies depending on the specific measurements, they all have the same thickness. To determine the thickness of the sample, Atomic Force Microscopy (AFM) imaging was performed. These measurements were carried out using the *Innova Bruker* atomic force microscope, which provides highly accurate results for characterizing the sample's thickness and topology (fig.7.3).

By utilizing a metallic tip attached to a cantilever, we were able to examine the surface morphology of the thin film.

This measurement was essential for determining the film thickness, which was found to be  $t = 206 \pm 8$  nm. This value plays a crucial role in accurately calculating the resistivity of the sample.

To evaluate the thickness of the sample, we analyzed the AFM images using the software *Gwyddion*, which allowed us to accurately measure the height profile of the film. Specifically, we examined multiple height profiles across different regions of the sample, obtaining a range of thickness values. The previously reported thickness



**Figure 7.3:** *Innova Bruker atomic force microscope.*

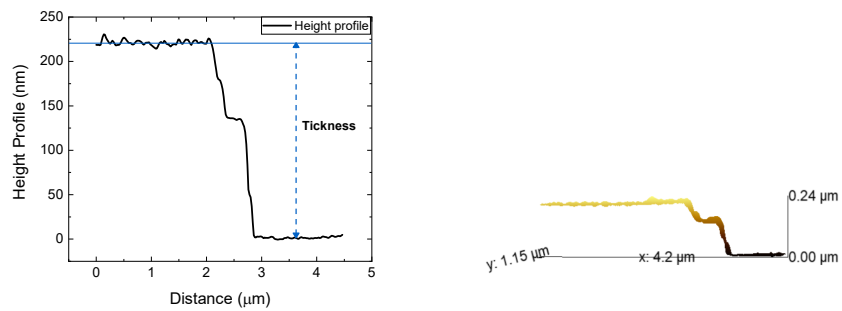


**Figure 7.4:** *On the left, a height profile used to determine the sample thickness is shown. The presence of an intermediate plateau is due to the incomplete breaking of the film during the cutting process of the corresponding  $Fe(Se,Te)$  batch. The right panel displays the corresponding 3D region from which the height profile was extracted.*

represents the mean of these measurements. The measurement uncertainty is defined as the semi-dispersion between the maximum and minimum thickness values.

Both panels of figure 7.4 displays one of these profiles, corresponding to a region of the sample that is free from impurities

The roughness of the sample was also estimated through data processing with

*Gwyddion*. In this case, selecting an appropriate region for analysis was crucial, as the presence of impurities could significantly affect the measurement. The key parameter we focused on was the root mean square roughness ( $R_q$ ) of the film. The region shown in figure 7.2 is used to perform the analysis yielding to  $R_q = 3.7$  nm.

Furthermore, a more detailed analysis was conducted using *Gwyddion* to extract information about the grain size of the sample. The grains, shown in figure 7.2, can be identified by following the boundaries of the yellow circular-like regions, which define the grain boundaries.

We performed the grain analysis to determine the equivalent disk radius of the grains ( $r_{eq}$ ) and their corresponding surface area ( $S_G$ ). The results are presented in Figure 7.5, which illustrates the distribution of these two quantities. By analyzing the figure, one can identify the most probable values for  $r_{eq}$  and  $S_G$ , as the graphs display their distribution over an area of  $5 \times 5 \mu\text{m}$  (specifically, the region shown in figure 7.2). The peaks of these distributions correspond to  $r_{eq} \simeq 72$  nm and  $S_G \simeq 0.015 \mu\text{m}^2$ .

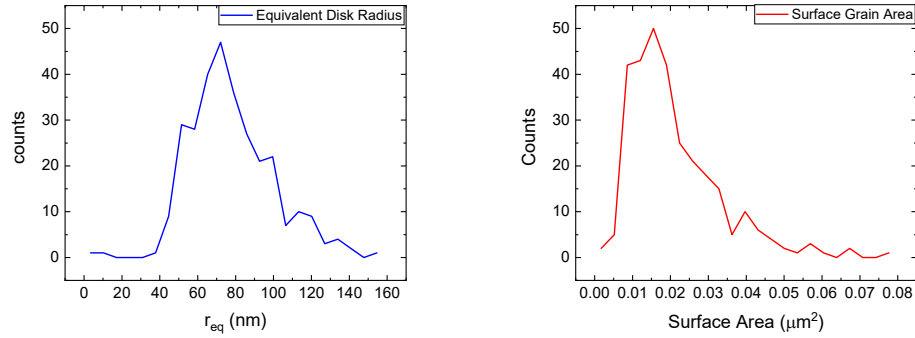


**Figure 7.5:** The left panel shows the distribution of the equivalent disk radius. The right image shows the distribution of the grain surface area.

### 7.1.2 Electron dispersive X-rays (EDX)

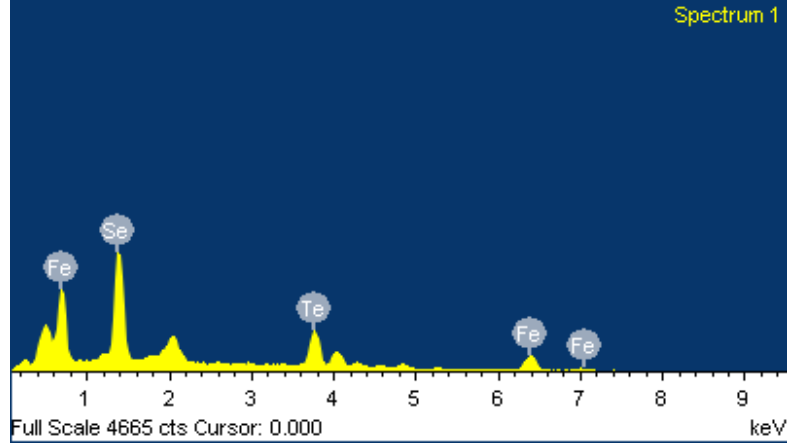


**Figure 7.6:** EDX spectrum provided by the x-rays emitted by the atoms.

To evaluate the stoichiometry of  $Fe_{1+\delta}(Se_{1-x}Te_x)$ , we performed EDX measurements, which allow for an accurate stoichiometric analysis of the samples. Specifically, we focused on two different regions of the surface, scanning them using a collimated electron beam. This beam excites the atoms present on the surface, causing them to emit characteristic X-rays, which are then collected by a cryogenic sensor. The energy dispersion acquired by the detector is subsequently analyzed and associated with specific atomic species using pre-established reference data.

In both regions, the EDX analysis confirmed the expected presence of Fe, Se, and Te (the spectrum of one of these regions is shown in 7.6). The latter elements were found in an atomic ratio of 1:1, corresponding to  $x = 0.5$ . Indeed, in these regions, we observed an excess of iron atoms, amounting to approximately 20% in the atomic distribution as we can see in table 7.1.

Elements	Weight%	Atomic%
Fe	43.63	58.86
Se	21.58	20.59
Te	34.80	20.55

**Table 7.1:** The results of the EDX measurements show the atomic and weight distribution of the elements in the material.

Finally, from now on we will refer to the sample  $Fe_{1+\delta}(Se_{0.5}Te_{0.5})$  simply as  $Fe(Se, Te)$ .

### 7.1.3 Transport measurements

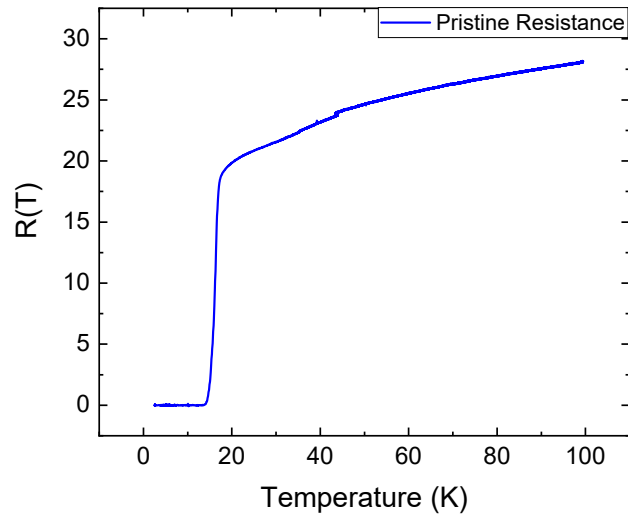


**Figure 7.7:** Resistance as a function of temperature up to 100 K.

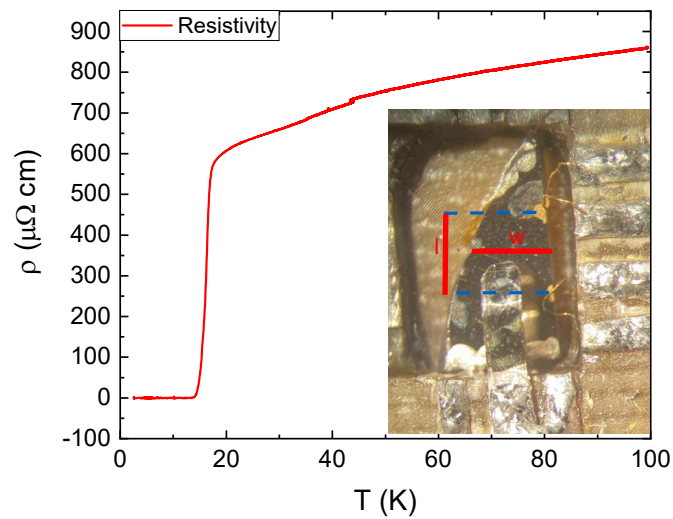


**Figure 7.8:** Resistivity as a function of temperature related to the sample configuration shown in the inset.

This section of the chapter aims to illustrate the transport properties of  $Fe(Se, Te)$  samples, focusing on the characteristics of the superconducting transition and subsequently investigating its spectroscopic properties through point-contact spectroscopy.

Figure 7.7 shows the resistance as a function of temperature up to  $T = 100$  K. In this temperature range, we observe that the resistance behavior is already noticeably curved.

Starting from these data, we reconstructed the resistivity behavior  $\rho(T)$  based on the sample's geometry. Specifically, we computed the channel length ( $l$ ) and channel width ( $w$ ) of the sample shown in the inset of figure 7.8. As a result, we obtained  $l = 1.72 \pm 0.38$  mm and  $w = 1.69 \pm 0.41$  mm. Additionally, using the thickness determined from the AFM measurements, we derived the resistivity as a function of temperature, as plotted in figure 7.8.

By analyzing the upmost panel of figure 7.9, we observe the behavior of the resistance normalized to its value at  $T = 35$  K. The trend follows that of a typical  $Fe(Se, Te)$  near optimal doping, exhibiting characteristic features such as a continuous decreasing of the resistance also before the superconducting transition. The critical temperature can be determined directly from the normalized resistance curve, using the formula

$$T_C = T_C^{50\%} \pm \frac{T_C^{90\%} - T_C^{10\%}}{2} \quad (7.1)$$

where  $T_C^{x\%}$  represents the temperature at which the resistance reaches  $x\%$  of its normal value. Applying Eq. (7.1) to the data shown in figure 7.9, we obtain a critical temperature of  $T_C = 16.2 \pm 1.0$  K with the onset of the transition at  $T_C^{onset} = 20.0$  K which aligns perfectly with values reported in literature [5, 133]. Here the superconducting onset transition temperature  $T_C^{onset}$  is defined as the intersection of the linear extrapolations of the normal state resistance with the tangent along the transition part of the curve. For future comparisons we explicitly pointed out also the  $T_C^{10\%,90\%}$  values. Indeed, we found  $T_C^{10\%} = 15.1$  K and  $T_C^{90\%} = 17.1$  K.

A more precise determination of  $T_C$  can be obtained by analyzing the first derivative of the resistance as a function of temperature. The latter exhibit a peak, which can be fitted through a Gaussian or a Lorentz function, providing the critical temperature value. Following this approach, we find  $T_C = 16.2 \pm 0.7$  K which is consistent with the previous computation (shown in figure 7.9).

However, we also noticed that prolonged exposure to the atmosphere has a detrimental effect on the material. In an uncontrolled environment, the resistance behavior tends to slightly change, particularly on the tail of the transition, becoming less definite.

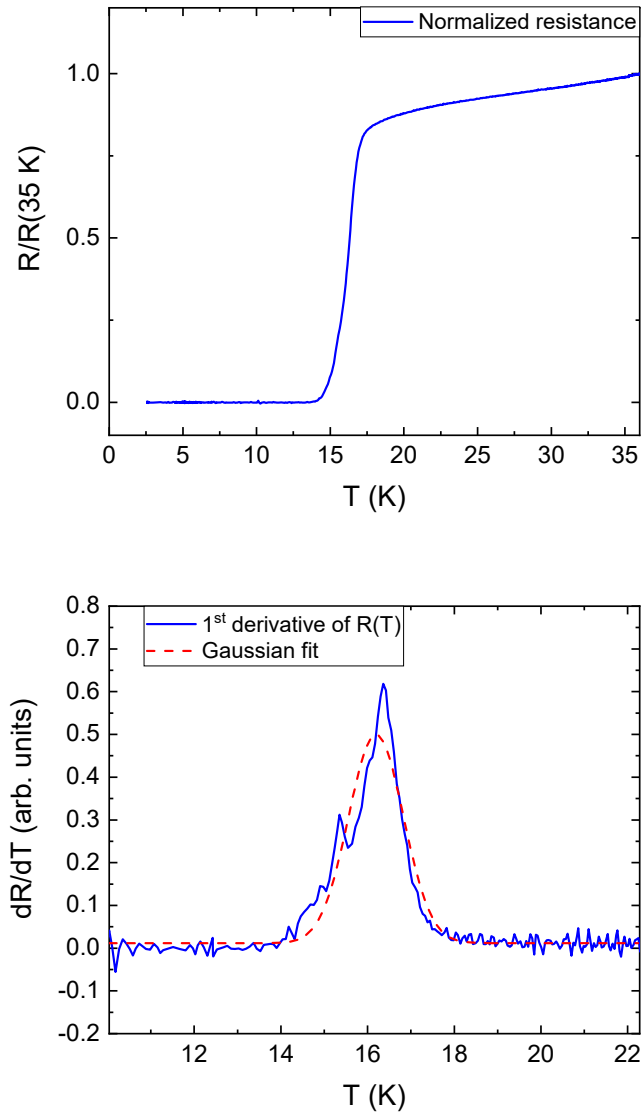


**Figure 7.9:** *The upmost figure shows the behavior of the normalized resistance as a function of the absolute temperature. The bottom panel shows the first derivative of the normalized resistance and the corresponding gaussian fit.*

#### 7.1.4 Point contact Andreev reflection spectroscopy

Figure 7.10 illustrates the temperature dependence of the differential conductance curve in the  $ab$ -plane of the  $Fe(Se,Te)$  film. The measurement is performed using the point-contact technique (see Chapter 4) where the contact exhibits a

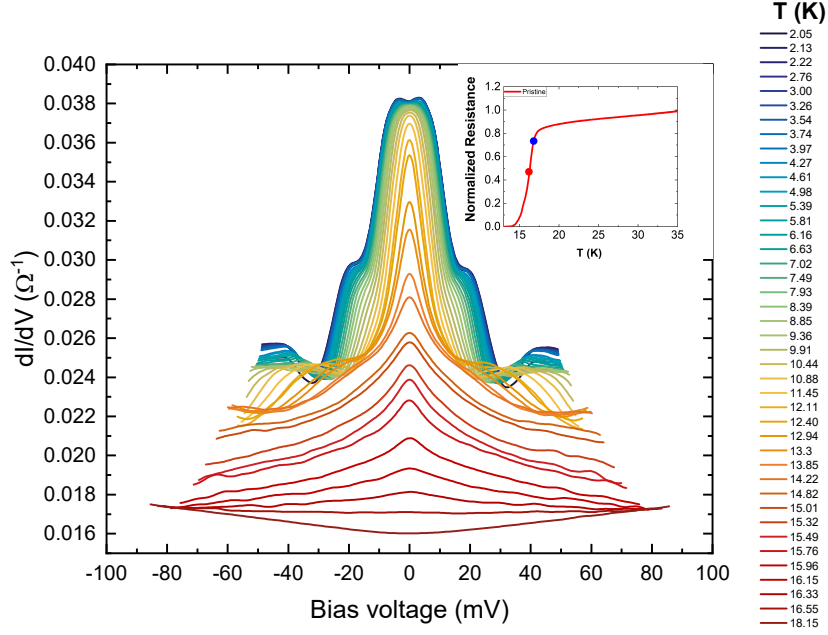


**Figure 7.10:** The figure shows the differential conductance curves on varying the temperature. The inset illustrates the resistivity measure as function of temperature. The blue dot represents the local critical temperature ( $T_C^A$ ) and the red dot signal the  $T^{50\%}$  of the sample.

normal resistance of  $R_N \simeq 33 \Omega$ . The low-temperature curves in figure 7.10 do not show any anomalies—such as zero-bias anomalies, downward bending of the high-energy tails, or low energy dips (i.e. for energies around  $\pm 10$  meV)—that could indicate contact defects or failures, which would violate the conditions for energy-resolved spectroscopy, as discussed in section (4.1). Instead, we observe characteristic conductance peaks: two symmetric maxima typical of Andreev reflection spectroscopy, located at approximately  $\pm 5$  meV. Additionally, secondary structures appear at around  $\pm 10$  meV. Based on their characteristics, these can be interpreted as signatures of electron-boson coupling within the N-S junction of the point contact. At approximately  $\pm 20$  meV, the curve displays shoulders due to critical current dips, which locally drive the contact region back into the normal state. This effect becomes increasingly dominant as the temperature rises. Furthermore, the shape of the two symmetric maxima gradually flattens with increasing temperature, eventually giving way to a single zero-bias peak. Around  $T \approx 5$  K, these structures disappear entirely, coinciding with the suppression of the Andreev reflection phenomenon due to thermal smearing and the reduction of the superconducting gap amplitude.

At  $T \approx 13$  K the conductance curves no longer exhibit any structure apart from the zero-bias peak and become completely smooth across the entire energy range. This occurs because the critical current becomes the dominant contribution within the contact. Once the temperature reaches  $T = 17.03$  K, the conductance curves remain unchanged, marking the transition from the superconducting to the normal state. The local critical temperature measured from these curves is  $T_C^A = 16.79 \pm 0.24$  K, a bit higher compared to literature values [13]. It is computed as the mean value between the last superconductive conductance curve and the first one related to the normal state. The critical temperature value, indeed, is consistent with the value found through transport measurement (see fig. 7.9).

The downward shift of the conductance curves is a typical feature of thin films. This shift is caused by the increasing dominance of spreading resistance ( $R_S$ ), which forms between the point-contact and the voltage electrode (see section 4.1). While this contribution is negligible at sufficiently low temperatures, it becomes significant in temperature regions where the  $R(T)$  is steeper, i.e during the superconducting transition. In these regions, the increase in  $R_S$  is large enough to cause bending of the conductance spectra. This observation highlights two key points:

- Only low-temperature curves can be used for spectroscopic purposes, as they fall within a temperature range where spreading resistance is negligible.
- The normal-state curve, in its current form, cannot be used for conductance normalization due to the downward shift.

To address this issue, as commonly done for Fe-based samples, a normalization step is required. Specifically, we normalize dividing by the normal-state after a shift of the curve on the vertical conductance and the subsequent rescaling of the bias scale. Once the necessary normalizations are applied, physically meaningful quantities can be extracted through fitting procedures, following the BTK model discussed in section 4.3.1.

To analyze the additional structures observed in the conductance curves, we need to implement the 2-band BTK model (discussed in chapter 4). In this case, we assume that the relevant spectroscopic energy range lies between  $\pm 20$  meV. Therefore, any features outside this range are attributed to the contribution of a critical current dip. Finally, based on these observations, we chose to normalize the conductance curve by shifting the normal state up to the shoulders located at  $\pm 20$  meV.

Indeed, figure 7.13 shows the temperature dependence of the normalized conductance curves up to  $T = 11.45$  K, illustrating the main spectroscopic features of the sample. We choose to stop the analysis at this temperature because for higher values the spectroscopic features disappear because of the critical current dip that dominates the contact.

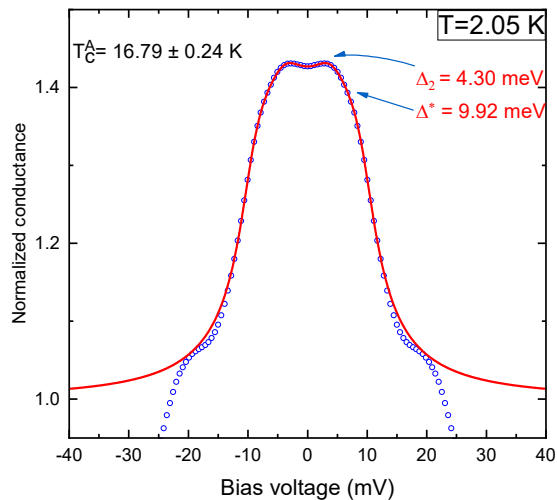


**Figure 7.11:** Here we show the theoretical curve (blue circles) and the normalized fit curve (red line) at the lowest temperature, i.e.  $T = 2.05$  K. We also report the values of the superconducting gaps.

Figure 7.11 shows the fitted curve (at  $T = 2.05$ ) obtained using the BTK model with two gaps. This model yields, indeed, two gap values  $\Delta_2 = 4.30$  meV and  $\Delta^* = 9.92$  meV, derived from the parameters listed in table 7.2. However,  $\Delta^*$  is not a true superconducting gap. We will demonstrate that the observed structures at 10 meV are signatures of strong electron-boson coupling, characterized by its resonance energy  $\Omega_b$  [13, 14].

$\Gamma_2$ (meV)	$Z_2$ (meV)	$\Gamma^*$ (meV)	$Z^*$ (meV)	$w_2$
2.5	0.294	2.44	0.127	0.25

**Table 7.2:** In this table are listed the values of parameters that we use to fit the conductance curve showed in figure 7.11.  $\Gamma$  refers to the broadening parameter while  $Z$  is associated to the barrier parameter of the fitting. In the end,  $w_2$  represents the weight assigned to the first band

However, for a two-band system, we expect two superconducting gaps. The smaller gap is usually characterized by a gap ratio lower than the value predicted by BCS theory, i.e.,  $2\Delta/k_B T_C < 3.53$ , while the second gap ratio exceeds the theoretical BCS value.

In fact, while the first gap ( $\Delta_2$ ) is associated with a gap ratio  $2\Delta_2/k_b T_C \simeq 5.8$ , the second one leads to  $2\Delta^*/k_b T_C = 14.39$  which is completely unreasonable for a

superconducting gap.

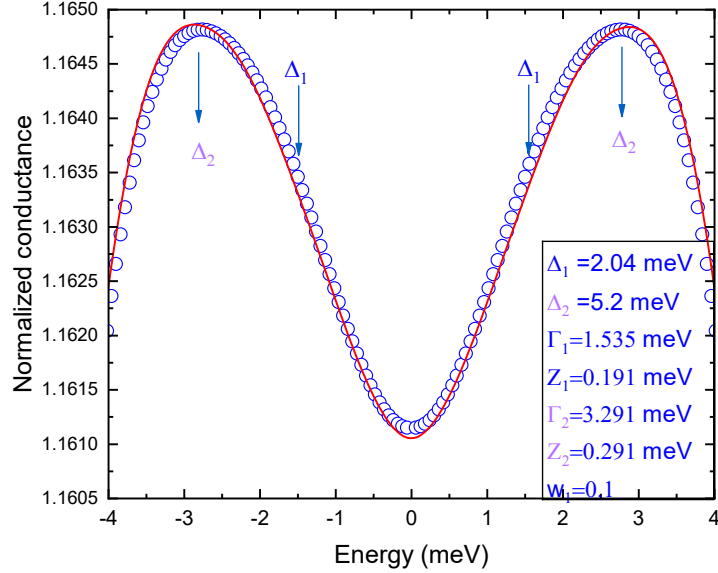


**Figure 7.12:** The panel shows the fitting (red solid line) of the normalized conductance curve (blue circles), focusing on the upper part. We show that, actually there exist two gaps in that energy range. The parameter are listed on the right together with the values of the order parameter.

Indeed, in the upper part of the curve, there are two gaps at lower energy, one of which is very difficult to observe on large scale. Therefore, by focusing on the relevant energy range, we can fit the experimental curve using once again the two-band BTK model, obtaining  $\Delta_1 = 2.04$  meV and  $\Delta_2 = 5.2$  meV as shown in figure 7.12, which aligns with literature [13].

Still, even though  $\Delta^*$  is not a true superconducting gap, the best theoretical curve is the one based on a two-gap fit where  $\Delta^*$  plays the role of the superconducting gap, as shown in figure 7.13.

In particular, the up and bottom images in figure 7.14 show the behavior of the parameters used for fitting the conductance curves as a function of temperature. We can observe that the broadening parameter remains relatively constant. The barrier parameter  $Z^*$  remains quite constant while  $Z_2$  decreases due to the fact that  $\Delta_2$  is, as we will explain later, associated to the largest superconducting gap, i.e. it closes faster than the smallest one.

The evolution of the superconducting parameter  $\Delta_2(T)$ , closely follows the

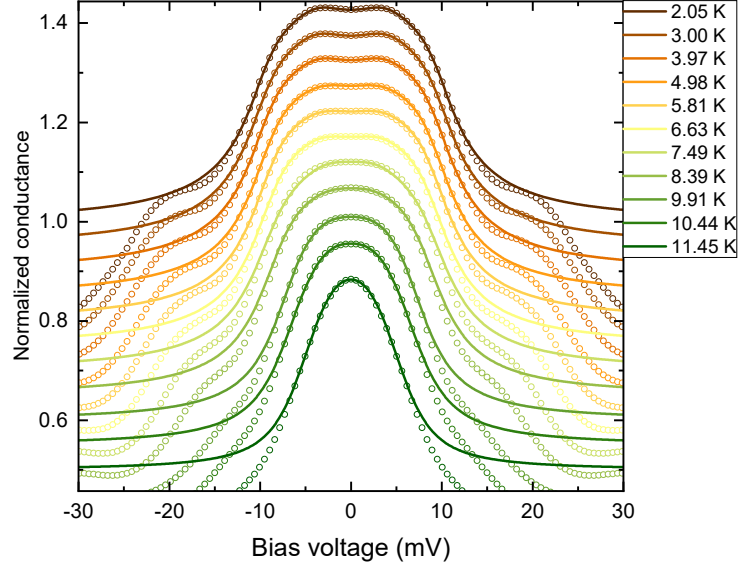


**Figure 7.13:** The picture illustrates the temperature dependence of the normalized conductance curves for each selected value of temperature.

theoretical trend predicted by BCS theory, which defines:

$$\Delta(T) = \Delta_0 \tanh \left( 1.74 \sqrt{\frac{T}{T_C} - 1} \right) \quad (7.2)$$

where  $\Delta_0$  is the gap value at zero temperature (we actually used the lowest temperature gap). On the other hand,  $\Delta^*$ , exhibits a significantly different behavior compared to the theoretical curve, not only because it is not a true superconducting gap but also due to the increasing influence of the critical current as the temperature rises (fig. 7.14).

Now, we aim to demonstrate that the gap, previously denoted as  $\Delta^*$ , is actually associated with a strong electron-boson interaction (EBI). Indeed, these structures are observable not only in the tunnel regime but also in the Andreev reflection one. They give rise to an energy peak in the spectra which we denote as  $E_P (= \Delta^*)$ , defined as:

$$E_P = \Omega_b + \Delta_{max} \quad (7.3)$$

where  $\Omega_b$  represents the bosonic resonance energy and  $\Delta_{max}$  refers to the maximum gap value at a given temperature [13, 14]. The peak value can be

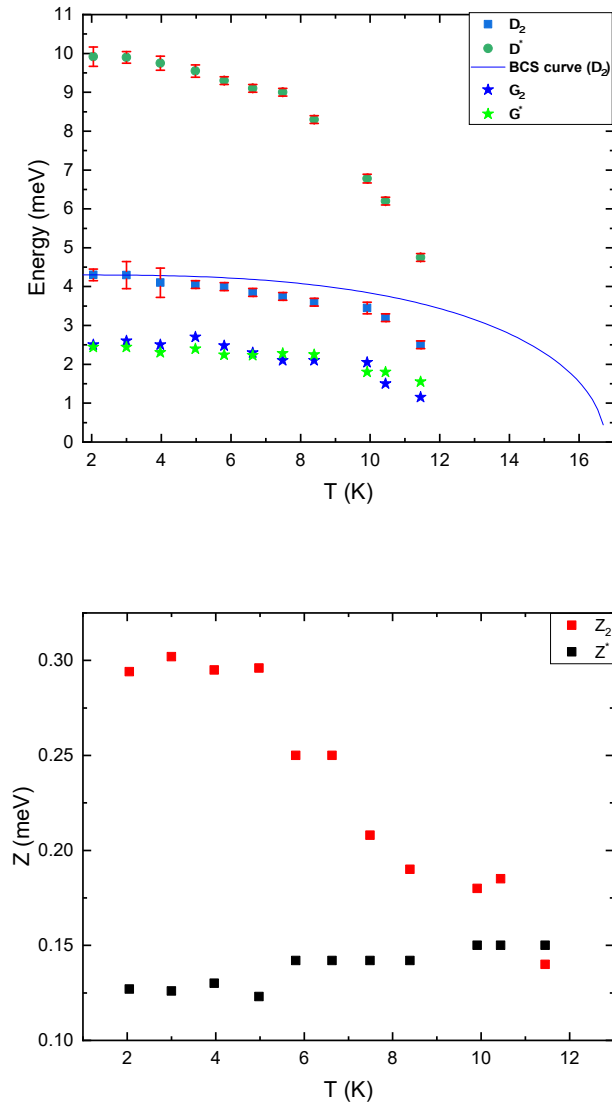


**Figure 7.14:** The upmost figure shows the temperature dependence of the superconducting gaps values (blue squares and green circles) along with the behavior of the gamma parameters (blue and green stars). In particular, we compare the temperature behavior of the superconducting gaps with the theoretical trend set by BCS theory (solid blue line). The bottom figure shows the temperature dependence of the barrier parameters.

determined from the experimental conductance curve. In fact, by differentiating

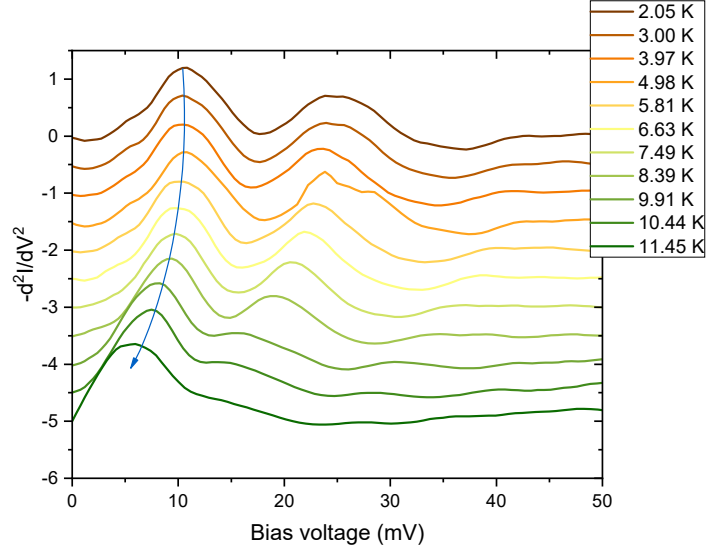


**Figure 7.15:** The figure shows the behavior of the  $-d^2I/dV^2$  with respect to the bias voltage for different values of temperature (the same of the one listed in figure 7.13). Note how the energy peak actually decreases when temperature increases. The curves are shifted by a constant offset for clarity.

them and changing the sign we obtain the behavior of  $-d^2I/dV^2$  as a function of the bias voltage  $V$ , as shown in figure 7.15.

Since the curves exhibit symmetry, with respect  $V = 0$  V, we consider only the positive bias values. Therefore, the second peak is most likely associated with the dips of the critical current, which affect the junction, disturbing the point-contact signal.

To analyze the energy value of the peak, we fit them to Lorentzian function, which effectively captures the peak in the spectra. This method allows us to determine the energy peaks for each temperature value, through which we can characterize the temperature dependence of the bosonic resonance energy. We observe that as the temperature increases, the  $E_P$  value starts to decrease, mainly due to the increasing influence of the critical current, which makes the contact more resistive. Nevertheless, by inverting Eq. (7.3), we can obtain  $\Omega_b$  for each analyzed temperature value.

Figure 7.16 shows the temperature dependence of the bosonic resonance energy. In particular, here we compare the trend of the energy peaks with that of  $\Delta^*$  values. It is evident that their values can be easily confused, suggesting that the so-called 'gap' ( $\Delta^*$ ) values are not related to a superconducting gap but rather originate from the energetic contribution of the EBI.

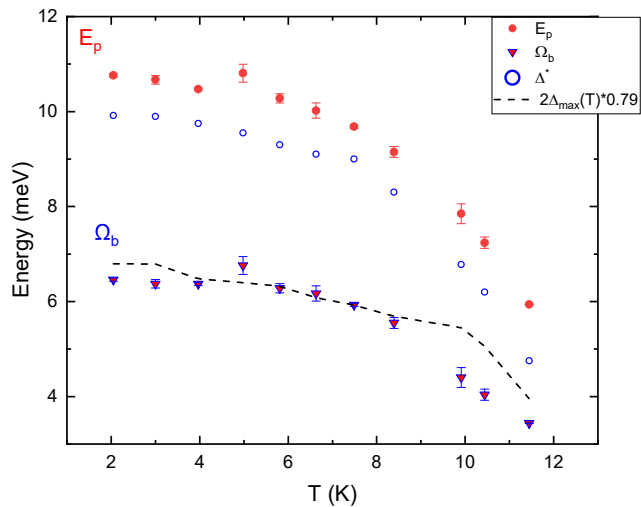


**Figure 7.16:** The panel shows the behavior of  $E_P$  and  $\Omega_b$  as a function of temperature. We compare the first to the behavior of  $\Delta^*$  and the second one to the right-hand side of equation (7.4).

The behavior of the bosonic resonance energy as a function of temperature is closely linked to that of the superconducting gap. Specifically, they obey the relation:

$$\Omega_b = 2\Delta_{max}(T) \times 0.79 \quad (7.4)$$

The trends of both sides of the equation are also shown in figure 7.16. We observe that their values are almost congruent, confirming our hypothesis: the 'gap' value of  $\Delta^*$  is not associated with a true superconducting gap. Instead, its energetic contribution arises from the strong electron-boson interaction, which induces a peak in the conductance curve, to which Andreev reflection is sensitive. This phenomenon allows, indeed, for both quantification and observation of the EBI [13, 14] due to spin fluctuations.

Figure 7.17 illustrates the temperature dependence of the differential conductance curves, where the point-contact is positioned along the  $c$ -axis of the sample. In this case, the normal-state resistance is  $R_N \simeq 56 \Omega$ . Unlike the behavior observed in figure 7.10, the low-temperature curves here exhibit a completely different shape.

Specifically, they appear more tunnel-like in the central region, where a minimum is observed precisely at zero bias, highlighting the superconducting gap. However, similar to the point-contact study on the  $ab$ -plane, the conductance curves are not flat outside the central region. Instead, they feature peaks at  $\sim \pm 10$  meV, along

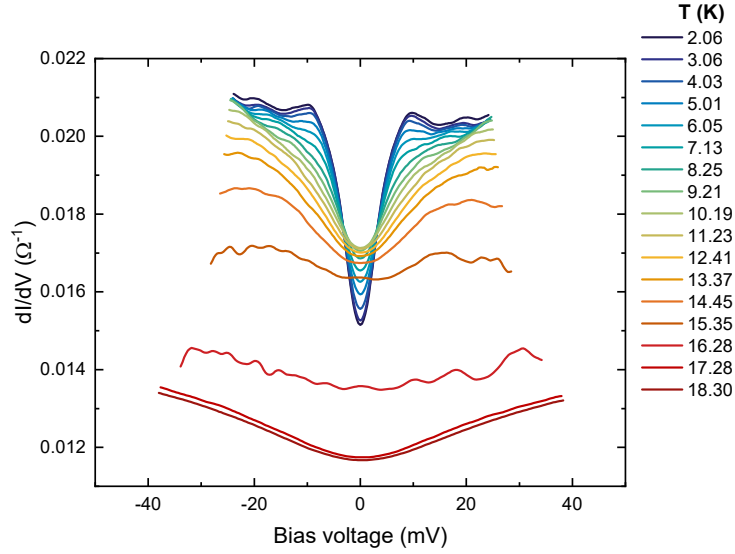


**Figure 7.17:** The image shows the differential conductance curves for different values of temperature for a point-contact made along the  $c$ -axis of the sample.

with two less pronounced symmetric structures at  $\sim \pm 20$  meV, located at exactly the same energy as in the previous case. By visual inspection, in this case, we can easily see that the material actually displays two superconducting gaps, according to what we found previously.

By analyzing the temperature evolution of the curves, we observe that the minimum progressively broadens and increases in value while remaining localized at zero bias. At  $T = 14.45$  K, the minimum disappears entirely and the corresponding conductance curve becomes noticeably less smooth. At its tails, the dominant effects of the critical current entering the junction become evident. The local critical temperature is determined as stated before and provide a value equal to  $T_C^A = 16.8 \pm 0.5$  K.

To analyze the behavior of the superconducting order parameter in  $Fe(Se, Te)$  thin film, we employ the two-band BTK model once again. This approach allows us to generate theoretical curves that closely replicate the experimental trend of the conductance as a function of energy.

Figure 7.18 shows the normalized conductance curve along with the corresponding fit, constructed using the parameters listed in Table 7.3. The theoretical curve yields two gap values:  $\Delta_2 = 2.38k_bT_C$  and  $\Delta^* = 6.02k_bT_C$ . Once again, the second gap appears larger than typical values. In fact, it is comparable to the one obtained in the previous analysis (see figure 7.11) and, thus, related to the EBI. Therefore, as in the case of the previous analysis, the fit of the conductance curves is more

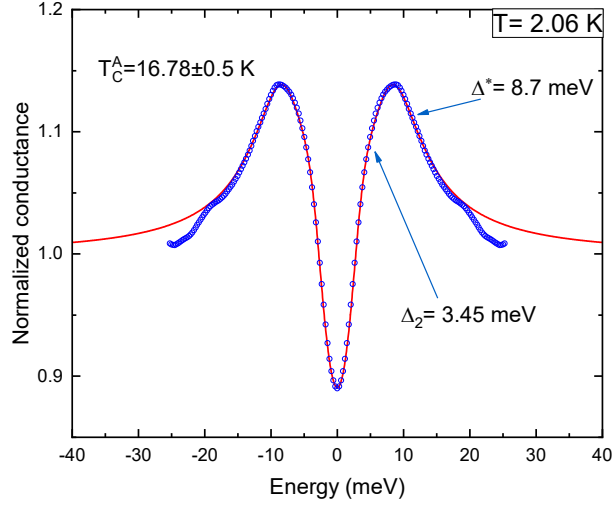


**Figure 7.18:** The panel shows the normalized conductance curve and its theoretical curve for  $T = 2.06$  K.

$\Gamma_2$ (meV)	$Z_2$ (meV)	$\Gamma^*$ (meV)	$Z^*$ (meV)	$w_2$
2.25	0.5	3.64	0.55	0.45

**Table 7.3:** In this table are listed the values of parameters that we use to fit the conductance curve showed in figure 7.18.  $\Gamma$  refers to the broadening parameter while  $Z$  is associated to the barrier parameter of the fitting. In the end,  $w_1$  represents the weight assigned to the first band

reproducible if we consider  $\Delta^*$  as a superconducting gap. The results are shown in figure 7.19. Here we can also observe the effect of the critical current that enters the contact becoming dominant. As the temperature increases, the order parameter value decreases, leading to a gap ratio of  $\Delta_2 = 1.66k_bT_C$  (at  $T \simeq 10$  K). Additionally, the critical current dip progressively suppresses the shoulders of the normalized conductance, located at approximately 10 meV.

Therefore, observing Figure 7.20, the behavior of  $\Delta^*$  as a function of temperature differs from the theoretical trend predicted by BCS theory. Instead, we note that the behavior of the real order parameter ( $\Delta_2$ ) as a function of temperature is in good agreement with the theoretical curve. The fitting process at higher temperatures than 10 K becomes meaningless, as the effect of the critical current dominates in the contact. Consequently, this dominant contribution rapidly suppresses the shoulders of the conductance curve, which are well observable at low temperatures.

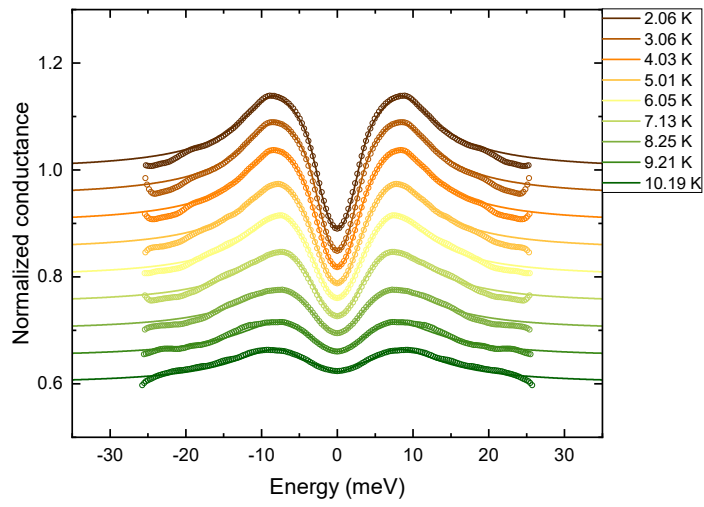


**Figure 7.19:** The temperature dependence of the normalized conductance curve is plotted here, where the effect of the critical current becomes increasingly significant as the temperature rises.

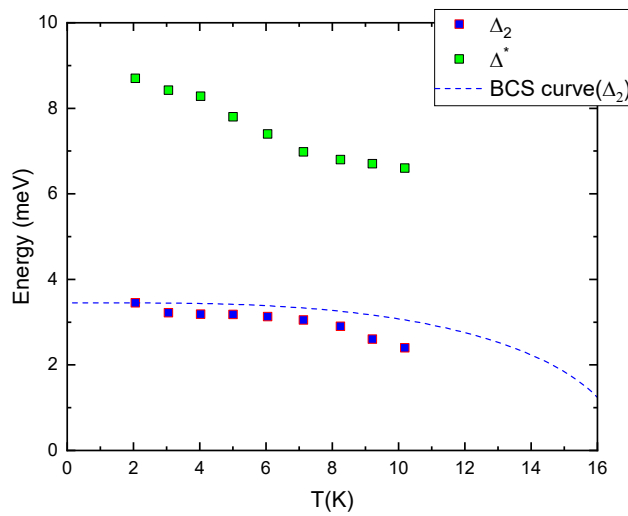


**Figure 7.20:** The figure illustrates the behavior of the order parameters as a function of temperature.

In addition, we observe that, unlike the previous analysis, some parameters change significantly. This is clearly visible in Figure 7.21, where the barrier parameter  $Z_2$  decreases to one-fourth of its initial value. This result is reasonable since, as the temperature increases, the depth of the conductance curve at zero bias continues to decrease, indicating that the tunneling character becomes less dominant. This behavior is well represented by the barrier parameter value, which simultaneously decreases with temperature.

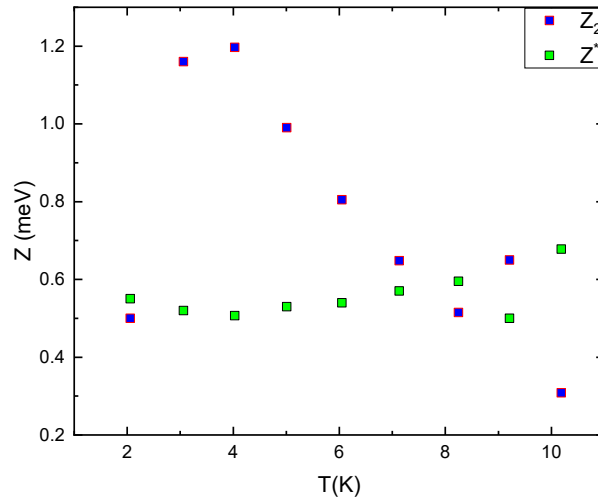


**Figure 7.21:** The plot shows the trend followed by the barrier parameter as a function of temperature.

## 7.2 Protonated samples measurements

### 7.2.1 AFM measurements

We also performed AFM measurements on  $Fe(Se_{0.5}Te_{0.5})$  after the intercalation process to investigate surface modifications. For this purpose, we selected an already damaged sample to gather information about the thickness of the  $Fe(Se,Te)$  thin film.

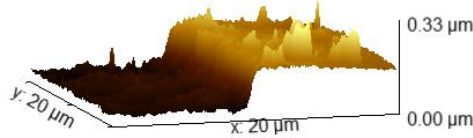


**Figure 7.22:** 3D height profile of  $Fe(Se_{0.5},Te_{0.5})$ , some peaks in the image coincides with impurities located on the surface of the sample.

To determine the thickness, we identified regions where the DES had chemically etched the surface (see figure 7.23), exposing the underlying substrate. By measuring the height difference relative to the substrate level, we obtained a thickness of  $t \simeq 152 \pm 13$  nm (see figure 7.22).

Although the surface appears clear and seemingly undamaged, the intercalation process has, in fact, led to a thinning of the sample, resulting in a thickness reduction of approximately  $\sim 50$  nm. This indicates the aggressiveness of the intercalation process, particularly due to the properties of this specific DES (as discussed in Chapter 6).

Therefore, the surface topology also changes due to the etching process. As seen in figure 7.24, the grains are no longer visible. This chemical process also affects the roughness parameter, which is higher compared to the pristine sample. Specifically, the root mean square roughness is found to be  $R_q \simeq 8.5$  nm, indicating that the DES has eroded entire portions of the thin film.

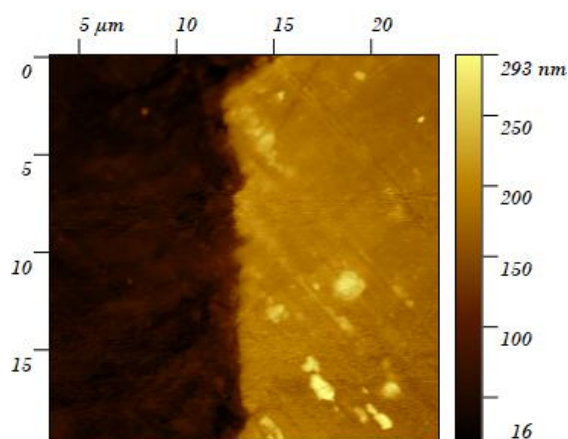


**Figure 7.23:** 2D representative AFM topography map of  $Fe(Se_{0.5}Te_{0.5})$  thin film. In the right corner there are some lighter regions which corresponds to some impurities.

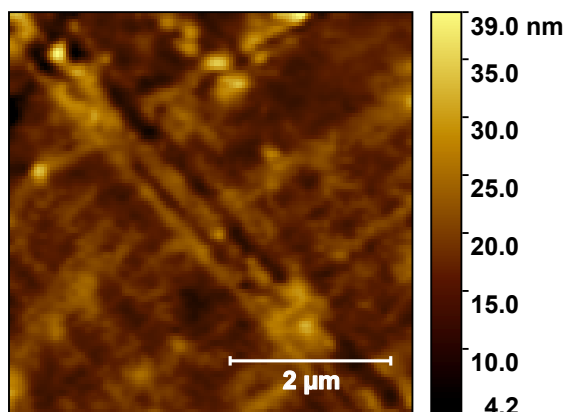


**Figure 7.24:** Zoom on the surface of the sample highlighting the topology of  $Fe(Se,Te)$  after the protonation process.

## 7.2.2 Transport measurements

Trying to control the transport properties of a material has always been one of the key objectives of scientist and researchers working in solid-state physics.

In recent years, among the various methods studied, the ionic gating technique has emerged. Its goal is to control the charge transport in different materials through the application of a gate voltage to the sample and also try to alter the properties of the materials, as discussed in chapter 5. In our case, the setup for the protonation procedure consists of a platinum electrode, a deep eutectic solvent (DES) connecting the electrode to  $Fe(Se,Te)$  sample, exactly as described in chapter 6. Figure 7.25,

indeed, shows the mounting used for the intercalation process.

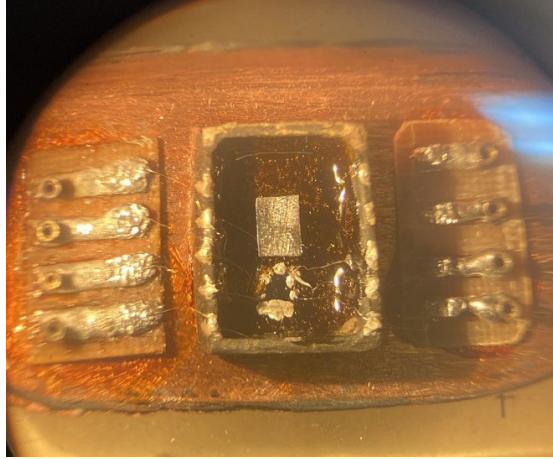


**Figure 7.25:** *Example of sample mounting used for the ions intercalation process.*

Although the physics behind the gating procedure is clear and rigorous, not all materials should be treated the same way. Specifically, depending on the sample under study, it is necessary to determine the maximum gate voltage that can be applied and whether to use a single-shot procedure or a gate ramp-one. This, in fact, represented a first challenge for us, as the risk of applying a too high gate voltage could potentially damage not only the intrinsic transport properties of the material but also the surface of the film itself.

Additionally, after analyzing the transport characteristics of the sample and measuring the resistance as a function of temperature, our goal is to understand whether the material is susceptible to protonation. In other words, we aim to observe whether and for how long the sample retains  $H^+$  ions after the removal of the corresponding gate voltage. This also determines whether spectroscopic measurements can be performed through PCARS. The idea of repeating the spectroscopic analysis arises from the fact that once  $H^+$  ions are intercalated through the application of the gate bias, they directly modify the material, potentially changing its intrinsic properties. It is likely that the latter exhibits different characteristics, such as altered superconducting gap values. Additionally, new structures may emerge in the differential conductance curves, or they may become more pronounced, possibly revealing phenomena and signatures related to topological superconductivity. Based on a methodology previously used for similar samples, we approached the problem using a gate voltage ramp with a rate of 1 mV/s, where the initial target voltage was  $V_G = 3$  V.

This threshold is set because the electrochemical window of the DES is significantly different from the target voltage. This allows us to safely exclude undesired chemical processes. Once the target voltage is reached, the sample is left under a

static gate voltage of the same value for approximately 1 hour and 30 minutes.

However, analyzing the previously presented AFM measurements, we observe that the process is not entirely safe for the sample's surface. Upon extraction, visual inspection revealed significant damage. During the voltage ramp and the subsequent waiting period, the electrolyte on the sample began to aggressively etch the surface, leading to the formation of bubbles. As a result, regions where the substrate of the sample was clearly visible appeared, signaling areas where the film had been 'consumed' by the liquid. Also for this reasons,  $V_G = +3\text{ V}$  marks a gate voltage threshold that should not be exceeded without causing irreversible damage to the material under study. The lower bound of our study range is set to  $V_G = +1.5\text{ V}$ , the gate bias value at which ionic dissociation of the DES occurs.

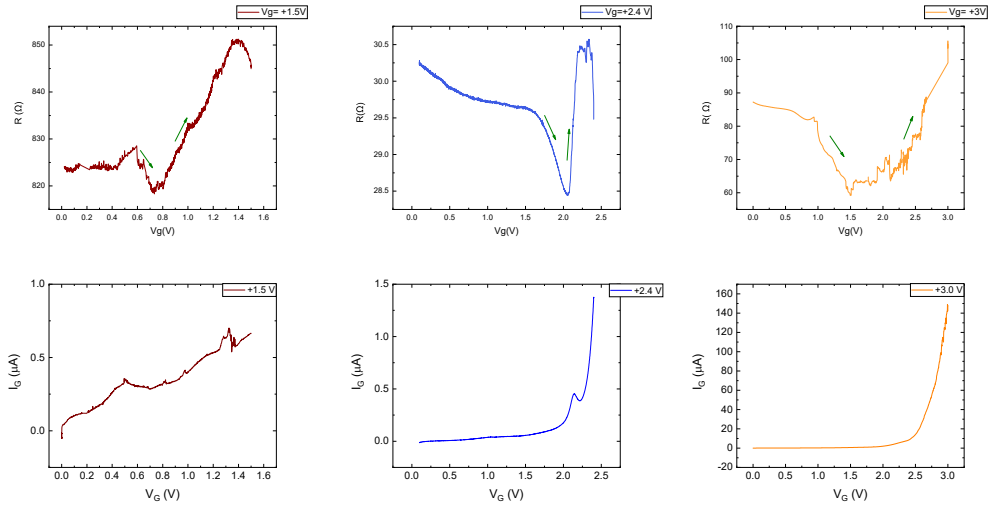


**Figure 7.26:** The top three panels show the resistivity curve as a function of the gate voltage for three different values of  $V_G$ . The bottom images illustrate the gate current as a function of the bias gate voltage.

The idea is to map the range between the two extremes with increments of  $+0.3\text{ V}$ . Figure 7.26 shows the evolution of resistance during the voltage ramp for different  $V_G$  values. Despite approaching different values due to sample variations and contacts conditions, we can highlight some common features. Initially, the resistance value decreases smoothly and relatively sharply. This decrease is typically followed by an increase in resistance, which then remains nearly constant during the waiting time when a static bias is applied. These features are also observed in the case of  $V_G = +3\text{ V}$ . The points where the resistance decreases indicate the moment when  $H^+$  ions begin to intercalate into the material due to the strong electric field. This is also confirmed by an increase (also smooth) in the gate current flowing through the structure (fig 7.26).

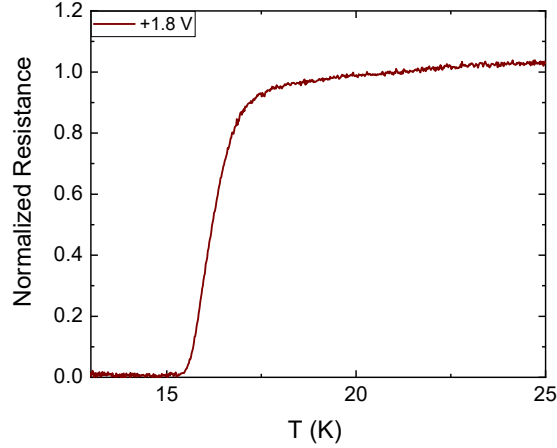


**Figure 7.27:** Normalized resistance (with  $R(22\text{ K})$ ) plotted as a function of temperature for a sample under  $V_G = 1.8\text{ V}$ .

However, after the protonation procedure discussed earlier, no significant changes in the  $R(T)$  curves are observed until a gate voltage of  $V_G = +2.4\text{ V}$ . The resistance curves are almost identical to the pristine curve. Indeed, the critical temperature marking the transition is around  $T_C \simeq 16\text{ K}$  compatible with the pristine measurement.

This suggests that the applied voltage, along with the waiting time under the static field, did not have a crucial effect on the sample. Specifically, the amount of intercalated ions within the material is insufficient to alter its transport properties. As an example we show in figure 7.27 the normalized resistance as a function of temperature for  $V_G = 1.8\text{ V}$ .

However small differences in the superconducting transition temperature are observed for  $V_G = 2.4\text{ V}$ . Under these conditions, the critical temperature is found to be  $T_C = 16.5 \pm 0.6\text{ K}$  using Eq. (7.1), while the derivative technique provides  $T_C = 16.4 \pm 0.3\text{ K}$  which are compatible one to the other (fig. 7.28).

The subsequent critical temperature shift can be determined using the respective  $T^{50}$  values. This provide  $\Delta T_C = 0.3\text{ K}$ . However, the difference is too small to ensure that the intercalation has been successful. Indeed, some differences can be noticed, first in the onset, where the intercalated sample exhibits a  $T_C^{onset} \simeq 18.4\text{ K}$ , and second in the tail of the transition, which falls earlier ( $T > 15\text{ K}$ ) compared to the pristine sample as we can see in figure 7.28.

Throughout the process, we monitored the behavior of the electrolyte. During the gate ramp, it exhibited occasional small bubbles, which were not particularly aggressive for the  $Fe(Se, Te)$  film. In fact, at the end of the measure, the surface

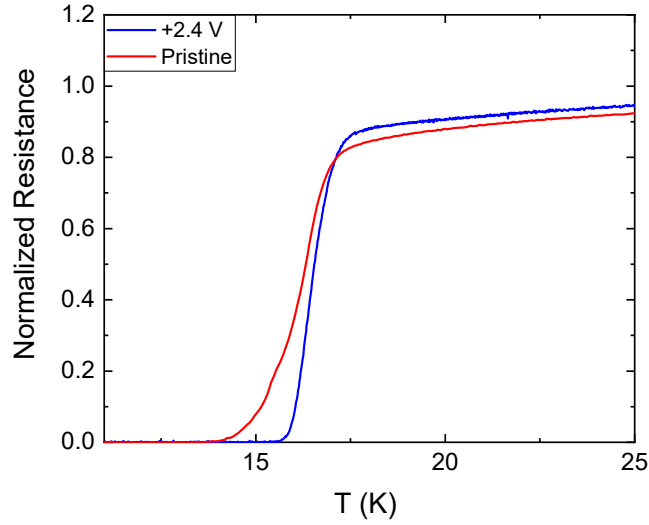


**Figure 7.28:** Normalized resistance as a function of temperature for the pristine and protonated case at  $V_G = +2.4$  V. Both graphs are normalized with the resistance value at  $T = 35$  K.

remained perfect and undamaged.

For  $V_G = +2.7$  V (black curve in figure 7.29), a critical temperature shift is observed with  $T_C = 20.8 \pm 2.65$  K, signaling a more pronounced change. Not only is there a change in the transition temperature, but the actual transition also behaves quite differently. As observed in figure 7.29, the transition is not as sharp as in the previous case but presents a much smoother curvature.

Despite the significant  $T_C$  shift, which in the case of  $V_G = +2.7$  V amounts to  $\Delta T_C = 4.6$  K, the  $Fe(Se, Te)$  sample is considerably damaged. As a result, much of the film is etched by the action of the ionic liquid subjected to the strong electric field.

Figure 7.29 shows also the normalized resistance as a function of temperature after applying a 3 V bias (orange curve). The transition is not uniform but occurs in two distinct stages, which we identify through two onset values  $T_C^{1, onset} \simeq 29.9$  K and  $T_C^{2, onset} \simeq 19$  K signaling a bi-phasic phase transition. Then, as in the other cases we evaluated the critical temperature using Eq (7.1), which yields to  $T_C = 19.8 \pm 5.0$  K. Thus, the critical temperature shift can be computed leading to  $\Delta T_C = 3.6$  K. Again, once extracted, as expected the film exhibits considerable damage, again due to chemical etching of the DES on the surface.

To mitigate this issue (sample damaging), we continuously monitored the entire process, from the gate ramp to the insertion of the descendant into the cryocooler.

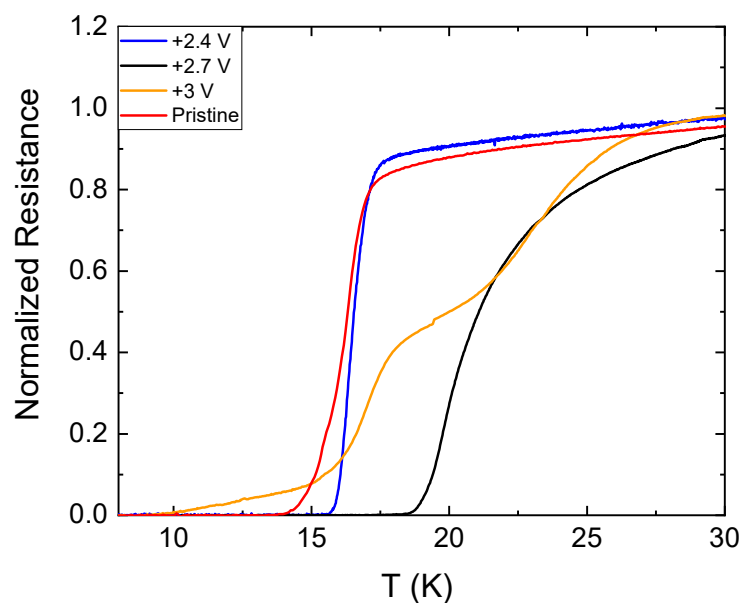


**Figure 7.29:** *The panel shows the resistance curves for different values of gate voltage compared to the pristine sample plotted as a function of temperature. We note that all the samples were characterized by a similar geometry.*

By doing so, we observed in real time the effects of the ionic liquid on the film, along with the variations in resistivity and gate current. The simultaneous observation of these three parameters allowed us to determine whether the process was becoming either hazardous for the sample or ineffective.

Notably, the damage that can be inflicted on the sample is linked to two key experimental indicators:

- A sharp increase in sample resistance, reaching values significantly higher than the initial one;
- The previously mentioned formation of bubbles.

Therefore, we observed that the formation of bubbles in the liquid during the protonation process serves as an indication that the process is proceeding successfully. In particular, some bubbles tend to localize around the current electrodes. On the other hand, some others appear near the exposed part of the film. These latter ones specifically signal a potential success of the ionic intercalation. However, this alone is not sufficient, as the quantity of bubbles produced also indicates the efficiency of the protonation process. This characteristic appears to

be proportional to the applied gate voltage. Therefore, we affirm that it's not possible to separate the bubbles formation (symptom of the surface etching) from an optimal  $H^+$  ions intercalation process using this kind of recipe.

Another important observation concerns the relationship between the amount of electrolyte deposited on the gate-film system and the gate current passing through the sample. During multiple protonation processes, particularly during the waiting time at a static bias  $V_G$ , we notice that removing (or adding) a small quantity of ionic liquid induces an immediate change in the gate current, which decreases (or increases). This suggests that, in addition to the already existing numerous parameters defining optimal protonation conditions, the quantity of electrolyte also plays a crucial role. However, the maximum usable amount is physically constrained by the dimensionality of the *pool* in the cryogenic insert.

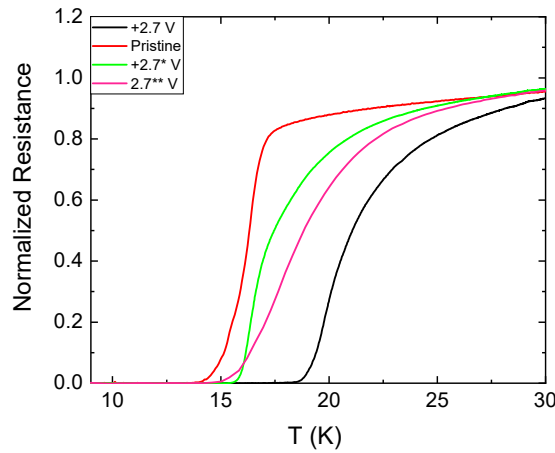


**Figure 7.30:** Comparison between the pristine normalized resistance and that of the protonated sample at  $V_G = +2.7$  V as a function of temperature.

Finally, in an attempt to verify the obtained results, we tried to replicate the critical temperature shift by applying the same procedure to a sample with a quite different geometry. The study of this new sample revealed additional experimental evidences, making the analysis more challenging. Therefore, we also noted the existence of a geometric factor, related to the physical dimension of samples and gate electrode, that plays a fundamental role in determining the actual voltage drop across the sample. This becomes evident in cases where the same applied gate bias does not yield identical results.

In particular, we encountered situations in which the applied gate voltage did not influence the superconducting phase of the sample, even when  $V_G \geq +2.7$  V. As shown in Figure 7.30, we compare the normalized resistance as a function of

temperature for three cases where an applied voltage of  $V_G = 2.7$  V was used. The primary difference between these three cases lies in the geometry of the sample.

In particular, when applying a gate voltage denoted as  $V_G = +2.7^*$  V, we once again observed a shift in the critical temperature of the sample. The superconducting transition, in this case, exhibits an onset at  $T_C^{onset} \simeq 24.3$  K, higher if compared to the pristine value of  $T_C^{onset} \simeq 20.0$  K. The midpoint of the transition occurs at  $T_C = 17.2 \pm 2.5$  K, indicating a critical temperature shift of  $\Delta T_C = 1.0$  K.

In addition, a similar effect was observed in another case where the geometry changed again. We denote this case as  $V_G = 2.7^{**}$  V. Specifically, we found that  $T_C = 18.6 \pm 3.25$  K, which is positioned between the values obtained for  $V_G = 2.7^*$  V and  $V_G = 2.7$  V. Consequently, the critical temperature shift for  $V_G = 2.7^{**}$  V amounts to  $\Delta T_C = 2.4$  K.

However, despite the critical temperature values, the behavior of the transitions of the intercalated samples are compatible one to the other. Indeed, they both exhibit a more pronounced curvature with respect to the pristine one, likely due to the effect of the ions hydrogen intercalation.

Notably, despite using the same gate voltage, the observed critical temperature shift differs from previous cases. This discrepancy is likely due to geometric variations among the samples used in different protonation processes. In particular, the present value of  $\Delta T_C$  is lower than the one obtained in the previous experiment at  $V_G = +2.7$  V.

Therefore, since that the value of the superconducting transition temperatures are quite different for the (apparently) same value of gate voltage, we suggest that the actual bias experienced by the sample might not correspond exactly to the provided voltage. Instead, the sample could be subjected to an effective voltage value  $V_{eff} < V_G$  due to the presence of the geometric factor.

This latter it's strictly related to two reasons:

- Since the system is ruled by capacitive effects, the surface ratio between the two electrodes (gate and sample) is crucial. Indeed, the gate surface have to be much larger then sample one.
- The physical distance between the gate electrode and the sample plays an important role. Indeed, the resistance encountered by the ions is greater as the distance increases. Therefore, a portion of the gate voltage is lost in proportion to the increase in distance.

Thus, based on these assumptions and the experimental evidence, we can safely conclude that  $V_G = 2.7^*$  V corresponds to a bias voltage that falls between 2.4 V and 2.7 V.

Finally, we can resume the experimental findings related to the intercalation procedure in table 7.4, which resumes the effect of the process on the critical temperature values.

$V_G$ (V)	$T_C^{50\%}$ (K)	$T_C^{90\%}$ (K)	$T_C^{10\%}$ (K)	$T_C^{onset}$ (K)	$\Delta T_C$ (K)	$\Delta T_C^{onset}$
0	16.2	17.1	15.1	20.0	0	0
2.4	16.5	17.2	16.1	23.0	0.3	3
2.7*	17.2	21.1	16.1	24.3	1	4.3
2.7**	18.6	22.8	16.3	26.6	2.4	6.6
2.7	20.8	24.6	19.3	27.5	4.6	7.5
3.0	19.8	25.5	15.5	29.9	3.6	9.9

**Table 7.4:** Summary about the effect of the intercalation process on the critical temperature values. Particularly, the last columns exhibits the values of the critical temperature shifts after the protonation. In red the samples damaged after the procedure.

As we can see from Table 7.4, the critical temperature values generally increase with the applied voltage, except for  $V_G = 3.0$  V. This behavior is reasonable, as the transition is influenced by two distinct regions of the sample, each exhibiting a different superconducting critical temperature. However, the intercalation process affects the entire transition.

Both  $T_C^{90\%}$  and  $T_C^{10\%}$  increase with the applied gate bias. Once again, the last row does not follow this trend due to the reasons previously discussed.

In conclusion, the onset of the transition also changes. Specifically,  $T_C^{onset}$  increases for all samples as the gate voltage increases. Notably, we achieved a maximum shift in the onset temperature of  $\Delta T_C^{onset} = 9.9$  K for  $V_G = 3.0$  V.

### 7.2.3 Point contact Andreev reflection spectroscopy

However, upon analyzing the available data, we observed that  $Fe(Se, Te)$  is not capable of retaining the  $H^+$  ions, i.e. after the extraction and cleaning of the sample it degrades to the pristine case. This makes it difficult to perform point-contact measurements, as the intercalated H ions diffuse out of the film in a shorter time scale with respect to that necessary to mount the sample in PCARS configuration. Therefore, the only viable option is to perform the Andreev reflection measurements *in situ*. Generally speaking, the mounting process is quite challenging because the shape of the point contacts, which must be as small as possible to ensure the ballistic regime, undergoes significant stress. In fact, since the ionic liquid tends to be detrimental to the Ag-paste, each contact needs to be covered with G.E. Varnish (as discussed in Chapter 6).

It is well known that during the cooling phase the G.E. Varnish contracts, affecting the stability of the contact. In the case of the PC, as shown in Figure 7.31, this type of stress is critical and can easily interrupt the electrical connection. Moreover,

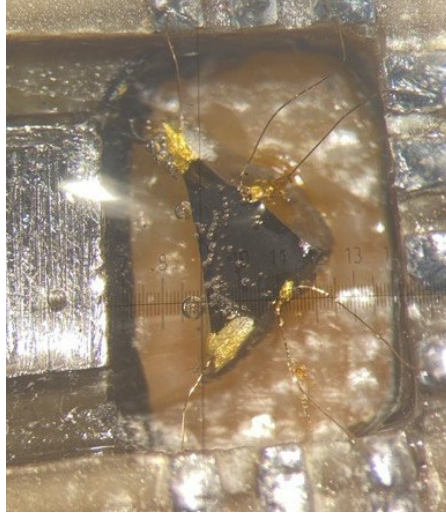


**Figure 7.31:** *This image shows the experimental setup used for in situ PCARS measurement. Here the stycast pool is substituted by a fiberglass pool, which not only plays the same role of the stycast-pool, but overcomes some technical difficulties (for instance the height difference between gate electrode and sample).*

during the protonation process, the contacts are further perturbed by the formation, movement, and bursting of bubbles that originate near the electrodes up to the freezing point of the DES.

Indeed, the spectroscopic measurements become more challenging because the point-contact is immersed in frozen liquid, which applies additional stress to the contact.

Nevertheless, we were able to perform *in situ* PCARS along the boundary of the sample (as shown in figure 7.31 under  $V_G = 2.7$  V).

Figure 7.32 shows the behavior of the differential conductance curve as a function of the bias voltage for different temperature values. We observe some analogies with respect to the one shown in Figure 7.10. In particular, both exhibit symmetric conductance maxima located at  $\sim 5$  meV, along with a local minimum at zero bias. The conductance curves shown in figure 7.32 correspond to a contact with a normal resistance  $R_N \simeq 24 \Omega$ . They present some anomalies, particularly along their tails, which are noticeable even at low temperatures. However, the temperature dependence differs significantly from the pristine case (Figure 7.10). The double-maxima structure disappears rather quickly (around 7 K), signaling the closure of one of the two gaps (the larger one), while the smaller gap remains visible around the zero-bias value.

The heating effect, along with the influence of the critical current dip, is already

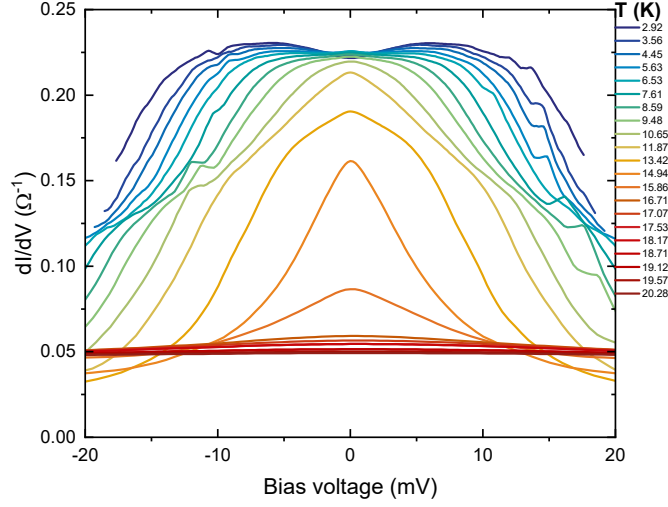


**Figure 7.32:** *Temperature dependence of differential conductance curves as a function of the bias voltage.*

significant even at low temperatures and becomes dominant as  $T$  increases. This is most likely due to the high value of the injected electrical current ( $\sim 4$  mA) required to obtain a sufficiently large energy range for the measured spectra ( $\sim 20$  mV). The local critical temperature, defined as discussed in the previous sections, is  $T_C^A = 19.57 \pm 0.71$  K.

However, the conductance curves are far from being ideal. This makes the fitting process of the curves extremely challenging, as the normalization step is not straightforward. Indeed, we assume that the energy range relevant for spectroscopy analysis is the interval  $[-12; +12]$  meV. Whatever is present outside this range is due to a huge critical current dip entering the contact along with a non-negligible heating contribution which is provided by the huge current value used for the measurements. This current value is necessary because of the low resistance value.

With this idea we shifted the normal state in order to analyze the desired energy range and we applied the 2-band BTK model.

Figure 7.33 exhibits the fit curve related to the differential conductance curve measured at  $T = 2.2$  K. The fit is realized imposing the parameter listed in table 7.5.

Therefore, we obtain two gap values:  $\Delta_1 = 2.2$  meV and  $\Delta_2 = 5.4$  meV. As expected, the superconducting gap values are higher than in the pristine case, which is consistent with the increase of the transition temperature.

Moreover, by analyzing Figure 7.33, we can visually observe the presence of the

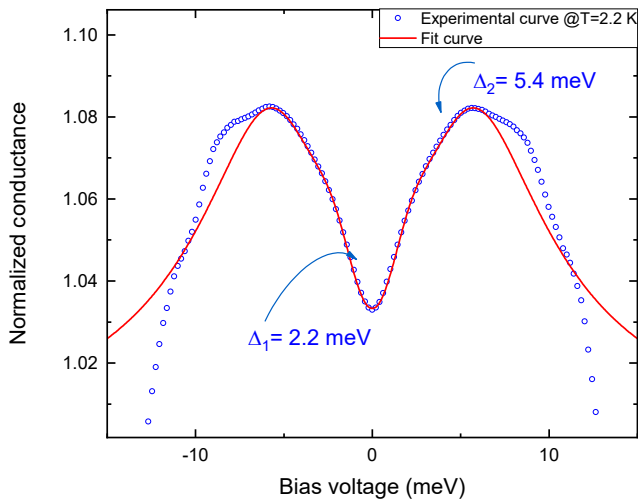


**Figure 7.33:** The panel shows the experimental curve (blue circles) along with the fitted one (red line).

$\Gamma_1$ (meV)	$Z_1$ (meV)	$\Gamma_2$ (meV)	$Z_2$ (meV)	$w_1$
1.78	0.352	3.69	0.55	0.42

**Table 7.5:** In this table are listed the values of parameters that we use to fit the conductance curve showed in figure 7.33.  $\Gamma$  refers to the broadening parameter while  $Z$  is associated to the barrier parameter of the fitting. In the end,  $w_1$  represents the weight assigned to the first band

electron-boson interaction (EBI), previously discussed for the pristine case. This interaction results in energy peaks located around  $\sim \pm 10$  meV. Furthermore, from the analysis of  $-d^2I/dV^2$ , we determine that the energy peak associated with the electron-boson interaction is  $E_P = 9.7$  meV. By inverting Eq. (7.3), we find the bosonic resonance energy to be  $\Omega_b = 4.3$  meV, which is lower than the pristine value.

Clearly more surprising are the conductance curves shown in figure 7.34, where the trend is completely different from the previously observed curves. The PC is characterized by a normal resistance of  $R_N \simeq 30 \Omega$ . At low temperature, it exhibits a zero-bias local maximum along with two local minima at an energy of  $\sim \pm 5$  meV. The curves remain relatively flat, except for two symmetric peaks located at  $\sim 10$  meV, which are likely related to a systematic error in the measurements. Indeed, these peaks are also present, though less pronounced, in the spectra

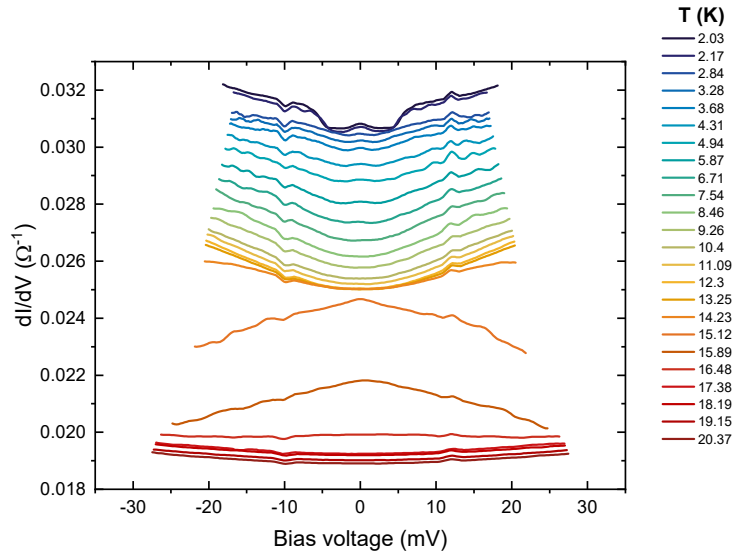


**Figure 7.34:** *Differential conductance curves as a function of bias voltage as the temperature increases.*

shown in figure 7.32.

The central zero-bias maximum disappears at  $T \simeq 9$  K. However, the most intriguing anomaly appears at  $T \simeq 15$  K, where the differential conductance curve undergoes a change in concavity. We suggest that this is due to the effect of the critical current dip, which becomes dominant in the contact. In this case, the critical temperature is found to be  $T_C^A = 19.76 \pm 0.61$  K, in perfect agreement with the previous case. Both critical temperature values are consistent with the resistivity measurements performed on the intercalated sample (see fig. 7.30), where, as expected, the local critical temperature value ( $T_C^A$ ) is found to be higher than the central  $T_C$  value.

Then, based on the same assumptions made in the previous analysis and considering the anomalies in the conductance curve, we implemented the two-band BTK model.

Indeed, as shown in Figure 7.35, we can clearly identify two structures corresponding to the superconducting gap values. These gaps are  $\Delta_1 = 2.9$  meV and  $\Delta_2 = 5.3$  meV, consistent with the values found in the previous conductance curves. As expected for a material with a higher  $T_C$ , the superconducting gap values are greater than those obtained for the pristine case.

Furthermore, we again observe the presence of the electron-boson interaction, which produces an energy peak at  $E_P = 10.1$  meV, leading to a bosonic resonance

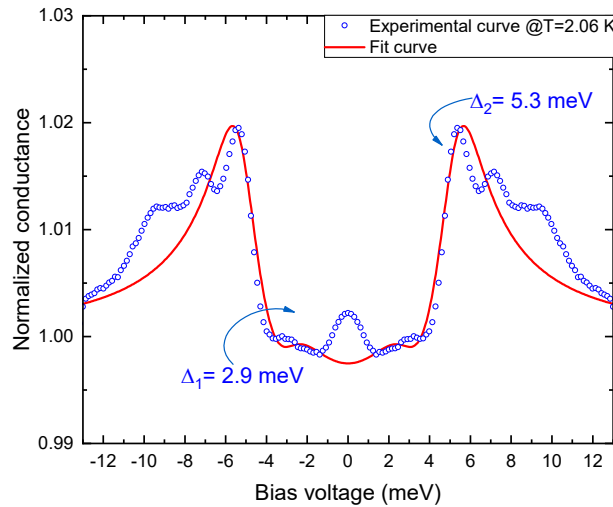


**Figure 7.35:** The panel shows the experimental curve (blue circles) along with the fitted one (red line).

energy of  $\Omega_b = 4.8$  meV, consistent with what we found for the conductance curve shown in figure 7.32.

$\Gamma_1$ (meV)	$Z_1$ (meV)	$\Gamma_2$ (meV)	$Z_2$ (meV)	$w_1$
0.8	0.15	0.9	1.2	0.52

**Table 7.6:** In this table are listed the values of parameters that we use to fit the conductance curve showed in figure 7.35.  $\Gamma$  refers to the broadening parameter while  $Z$  is associated to the barrier parameter of the fitting. In the end,  $w_1$  represents the weight assigned to the first band

The parameters of the fitted curve are shown in Table 7.6.

We note that the value of  $Z_2$  (the barrier parameter of the second band) is quite large compared to the previous case. This is consistent with the fact that the curve exhibits a more tunnel-like behavior.

Moreover, the theoretical curve, which accurately reproduces the main spectroscopic features of the sample, can only be obtained by introducing a new parameter, denoted as  $w_N$ . This parameter represents the percentage of normal contacts forming the point-contact. Specifically, the best fit is achieved with  $w_N = 0.93$ , meaning that 93% of the contacts remain in the normal state.

However, the two-band BTK model does not accurately reproduce the peak at zero bias. We suggest that if the material were topological in its normal state, it

might exhibit a zero-bias peak, potentially related to some specific features, such as scattering with magnetic impurities due to the excess of Fe atoms or related to the presence of zero-energy bound states.

In conclusion, our analysis confirmed our expectations: the gate-driven ion intercalation process effectively modifies the superconducting properties of  $Fe(Se_{0.5}Te_{0.5})$  thin films. Furthermore, we demonstrated that this phase can be investigated *in situ* via PCARS.

First, we observed significant differences in the critical temperature shift, which was higher in the intercalated sample compared to the pristine one. Additionally, based on the success of the protonation technique, we expected an increase in the superconducting gap values relative to the pristine sample. Indeed, the experimental analysis confirms an increase in the superconducting gap values in both cases presented.

However, an open question remains regarding the presence of the zero-bias peak observed in Figure 7.34, which could potentially be related to a boundary state hosted by the sample.

## Chapter 8

# Conclusions and future perspective

The goal of this thesis was to analyze and characterize the superconducting phases of  $Fe(Se_{0.5}Te_{0.5})$  thin films and its evolution with ionic gate-driven hydrogen intercalation. The entire work was carried out in the DISAT laboratories (LaTEST) at Politecnico di Torino. Below, we summarize the main experimental results obtained in this study.

The choice of this study material was motivated by the fact that several studies in the literature propose  $Fe(Se, Te)$  as a potential topological superconductor. This hypothesis is still under debate, but if confirmed, the material would gain significant importance both from a fundamental physics perspective and for technological applications, such as quantum computing (as discussed in Section 1.1), due to its potential to host Majorana bound states (MBS).

Thanks to the availability of high-quality samples provided by Professor Kazumasa Iida (Nihon University, Japan), our goal was to gather information through point-contact Andreev reflection spectroscopy (PCARS), a technique capable of capturing spectroscopic features by analyzing the differential conductance of the material. Indeed, it is well known from the literature that one of the first signatures of the presence of MBS is the appearance of a zero-bias peak in the conductance curve, which can, in principle, be detected using the PCARS technique. With this motivation, we proceeded with the characterization of  $Fe(Se_{0.5}Te_{0.5})$  in both its pristine and protonated forms.

Initially, we characterized the pristine  $Fe(Se, Te)$  sample in detail, focusing on its transport properties, specifically the resistance as a function of temperature. Our study revealed that our  $Fe(Se_{0.5}Te_{0.5})$  films underwent a superconducting phase transition at  $T_C \simeq 16$  K. Subsequently, we investigated the spectroscopic properties of the material using point contact Andreev reflection spectroscopy.

This technique confirmed that  $Fe(Se,Te)$  is a multiband system, characterized by two superconducting gaps,  $\Delta_1 = 2.04$  meV and  $\Delta_2 = 5.2$  meV. Additionally, we demonstrated that the energetic structures observed in the conductance spectra, located at  $\sim \pm 10$  meV, are not associated with an additional gap but rather with strong electron-boson interactions, which give rise to a peak in the energy spectrum. Based on these energetic values, we were the first showing the temperature dependence of the bosonic resonance energy ( $\Omega_b$ ), which aligns quite well with theoretical model.

The second part of this thesis focused on the intercalation process of the  $Fe(Se,Te)$  thin films.

We first achieve a standardization of the protonation procedure which consists in well-defined step: gate ramp at a pace of 1 mV/s and a waiting time, under static gate bias, which amounts to  $1h$  30 *min*. Then, we demonstrated that it is possible to modify the superconducting phase properties through  $H^+$  ion intercalation, leading to a superconducting phase with a higher  $T_C$ . Our objective—achieving an increase in the critical temperature without causing irreversible damage to the sample—was successfully met. Specifically, we showed that by applying a gate bias of  $V_G = +2.7$  V, the critical temperature shift amounted to  $\Delta T_C = 4.3$  K.

Due to the volatility of  $Fe(Se,Te)$ , PCARS measurements on the intercalated sample had to be performed *in situ* that is something which has never been attempted. Nevertheless, we successfully acquired energy spectra, revealing superconducting gap values of  $\Delta_1 = 2.2$  meV and  $\Delta_2 = 5.4$  meV. As expected for a material with higher- $T_C$  the superconducting gap values are actually larger than the pristine ones. In addition, the low-temperature conductance curves also reveal the presence of electron-boson interaction, whose resonance energy ( $\Omega_b$ ) has been evaluated in this case as well and found to be lower than that of the pristine sample at the same temperature.

Moreover, the spectroscopic analysis conducted on the protonated sample reveals an intriguing feature in one of the conductance curves. As discussed in Chapter 7, the tunnel-like conductance curve exhibits a pronounced zero-bias conductance peak (ZBCP). Several factors could explain this observation, such as possible scattering with magnetic impurities, which could be justified by the excess of Fe atoms.

However, we also note that the structure of the ZBCP observed in this study closely resembles those detected and reported in the literature through STM/STS measurements, where they have been attributed to the presence of Majorana bound states and, consequently, to a topological superconducting phase.

Still, even though the results are quite interesting and encouraging, they represent only a preliminary analysis.

To strengthen the validity of the experimental findings, it is essential to expand the statistical significance of the measurements by extending the study to additional samples. Along with the characterization of the superconducting phase—both in

the pristine and protonated states—it is also necessary to conduct measurements down to  $T = 300$  mK. This is because experimental evidence of potential zero-bias peaks, associated with Majorana particles, is typically observable only at very low temperatures.

Furthermore, a magnetic field analysis, both perpendicular and parallel to the  $c$ -axis, should be performed to better characterize the conductance curves.

Another potential improvement for future studies concerns the stabilization of measurements on intercalated  $Fe(Se,Te)$ . A significant challenge encountered in this work was the necessity of using G.E. Varnish to cover the electrodes, which increased the likelihood of breaking electrical connections. A possible solution could be to use Au- or Pt-based pastes instead of Ag paste, as they are more resistant to the electrolyte and could thus provide more stable electrical contacts. Instead, to improve the PCARS measurements, one could use Ag paste with nanometric granulometry, allowing for a more precise analysis of the surface features of the sample.

Additionally, future analyses of the intercalated sample could be performed using a *Hall bar* configuration, allowing for the physical separation of electrodes from the ionic liquid. Thus, improving the accuracy for transport measurements. Therefore, these improvements could help to further clarify and stabilize the high- $T_C$  superconducting phase. Investigating alternative electrolytes that are less aggressive toward the film surface could be another key advancement. Furthermore, a deeper understanding of the role of sample geometry in the intercalation process, along with a precise quantification of the effective gate voltage applied to the sample, would be essential for optimizing the process.

In conclusion, the characterization of the material can be further refined by including samples with different stoichiometries in the study. This would allow us to investigate how they behave under protonation conditions and whether they exhibit conductance features similar to the previously mentioned zero-bias conductance peaks.

# Bibliography

- [1] Boeri Lilia et al. «The 2021 room-temperature superconductivity roadmap». In: *Journal of Physics: Condensed Matter* 34.18 (2022), p. 183002 (cit. on p. 2).
- [2] Erik Piatti et al. «Superconductivity induced by gate-driven hydrogen intercalation in the charge-density-wave compound 1 T-TiSe<sub>2</sub>». In: *Communications Physics* 6.1 (2023), p. 202 (cit. on pp. 2, 66).
- [3] Yi Cui et al. «Ionic-liquid-gating induced protonation and superconductivity in FeSe, FeSe<sub>0.93</sub>S<sub>0.07</sub>, ZrNCl, 1T-TaS<sub>2</sub> and Bi<sub>2</sub>Se<sub>3</sub>». In: *Chinese Physics Letters* 36.7 (2019), p. 077401 (cit. on pp. 2, 63–66).
- [4] T. M. McQueen, A. J. Williams, P. W. Stephens, J. Tao, Y. Zhu, V. Ksenofontov, F. Casper, C. Felser, and R. J. Cava. «Tetragonal-to-Orthorhombic Structural Phase Transition at 90 K in the Superconductor Fe<sub>1.01</sub>Se». In: *Phys. Rev. Lett.* 103 (5 July 2009), p. 057002. DOI: 10.1103/PhysRevLett.103.057002 (cit. on pp. 3, 26).
- [5] Kuo-Wei Yeh et al. «Tellurium substitution effect on superconductivity of the  $\alpha$ -phase iron selenide». In: *Europhysics Letters* 84.3 (2008), p. 37002 (cit. on pp. 3, 29–32, 87).
- [6] Yoshinori Imai, Yuichi Sawada, Fuyuki Nabeshima, and Atsutaka Maeda. «Suppression of phase separation and giant enhancement of superconducting transition temperature in FeSeTe thin films». In: *Proceedings of the National Academy of Sciences* 112.7 (2015), pp. 1937–1940. DOI: 10.1073/pnas.1418994112 (cit. on pp. 3, 29).
- [7] Xianxin Wu, Shengshan Qin, Yi Liang, Heng Fan, and Jiangping Hu. «Topological characters in Fe(Se,Te) thin films». In: *Physical Review B* 93.11 (Mar. 2016). ISSN: 2469-9969. DOI: 10.1103/physrevb.93.115129 (cit. on pp. 3, 33).
- [8] Dongfei et all Wang. «Evidence for Majorana bound states in an iron-based superconductor». In: *Science* 362.6412 (Oct. 2018), pp. 333–335. ISSN: 1095-9203. DOI: 10.1126/science.aao1797 (cit. on pp. 3, 33).

- [9] T. Machida, Y. Sun, S. Pyon, S. Takeda, Y. Kohsaka, T. Hanaguri, T. Sasagawa, and T. Tamegai. «Zero-energy vortex bound state in the superconducting topological surface state of Fe(Se,Te)». In: *Nature Materials* 18.8 (June 2019), pp. 811–815. ISSN: 1476-4660. DOI: 10.1038/s41563-019-0397-1 (cit. on pp. 3, 33).
- [10] Lingyuan et al. Kong. «Half-integer level shift of vortex bound states in an iron-based superconductor». In: *Nature Physics* 15.11 (Aug. 2019), pp. 1181–1187. ISSN: 1745-2481. DOI: 10.1038/s41567-019-0630-5 (cit. on pp. 3, 33).
- [11] K. T. Law, Patrick A. Lee, and T. K. Ng. «Majorana Fermion Induced Resonant Andreev Reflection». In: *Phys. Rev. Lett.* 103 (23 Dec. 2009), p. 237001. DOI: 10.1103/PhysRevLett.103.237001 (cit. on pp. 3, 33).
- [12] M Wimmer, A R Akhmerov, J P Dahlhaus, and C W J Beenakker. «Quantum point contact as a probe of a topological superconductor». In: *New Journal of Physics* 13.5 (May 2011), p. 053016. ISSN: 1367-2630. DOI: 10.1088/1367-2630/13/5/053016 (cit. on pp. 3, 33).
- [13] Dario Daghero, Paola Pecchio, GA Ummarino, F Nabeshima, Y Imai, A Maeda, I Tsukada, S Komiya, and RS Gonnelli. «Point-contact Andreev-reflection spectroscopy in Fe (Te, Se) films: multiband superconductivity and electron-boson coupling». In: *Superconductor Science and Technology* 27.12 (2014), p. 124014 (cit. on pp. 3, 37, 90–93, 96).
- [14] Mauro Tortello, Dario Daghero, GA Ummarino, VA Stepanov, J Jiang, JD Weiss, EE Hellstrom, and RS Gonnelli. «Multigap superconductivity and strong electron-boson coupling in Fe-based superconductors: a point-contact Andreev-reflection study of Ba (Fe 1-x Co x) 2 As 2 single crystals». In: *Physical review letters* 105.23 (2010), p. 237002 (cit. on pp. 3, 91, 93, 96).
- [15] URL: <https://physicsfeed.com/> (cit. on p. 6).
- [16] Dirk van Delft. «History and significance of the discovery of superconductivity by Kamerlingh Onnes in 1911». In: *Physica C: Superconductivity* 479 (2012). Proceedings of VORTEX VII Conference, pp. 30–35. ISSN: 0921-4534. DOI: <https://doi.org/10.1016/j.physc.2012.02.046> (cit. on p. 7).
- [17] J. Bardeen, L. N. Cooper, and J. R. Schrieffer. «Microscopic Theory of Superconductivity». In: *Phys. Rev.* 106 (1 Apr. 1957), pp. 162–164. DOI: 10.1103/PhysRev.106.162 (cit. on pp. 7, 8, 10).
- [18] J. Bardeen, L. N. Cooper, and J. R. Schrieffer. «Theory of Superconductivity». In: *Phys. Rev.* 108 (5 Dec. 1957), pp. 1175–1204. DOI: 10.1103/PhysRev.108.1175 (cit. on pp. 8, 10).

- [19] Pooja Redhu, Sanjeev Kumar, and Abhishek Kumar. «Superconducting proximity effect and spintronics». In: *Materials Today: Proceedings* (2023). ISSN: 2214-7853. DOI: <https://doi.org/10.1016/j.matpr.2022.12.183>. URL: <https://www.sciencedirect.com/science/article/pii/S2214785322075563> (cit. on p. 9).
- [20] M Cyrot. «Ginzburg-Landau theory for superconductors». In: *Reports on Progress in Physics* 36.2 (Feb. 1973), p. 103. DOI: 10.1088/0034-4885/36/2/001 (cit. on p. 9).
- [21] Vitaly L. Ginzburg. «On Superconductivity and Superfluidity (What I Have and Have Not Managed to Do), as well as on the ‘Physical Minimum’ at the Beginning of the 21st Century». In: *ChemPhysChem* 5.7 (), pp. 930–945. DOI: <https://doi.org/10.1002/cphc.200400182> (cit. on p. 9).
- [22] Boher K.W. and Pohl U.W. *Semiconductor Physics*. Springer, 2020 (cit. on p. 11).
- [23] Francesco Pattini. «Growth of oxide thin films for energy devices by Pulsed Electron Deposition». In: (Jan. 2009) (cit. on p. 11).
- [24] A. A. Abrikosov. «On the Magnetic properties of superconductors of the second group». In: *Sov. Phys. JETP* 5 (1957), pp. 1174–1182 (cit. on p. 12).
- [25] A. A. Abrikosov. «The magnetic properties of superconducting alloys». In: *J. Phys. Chem. Solids* 2.3 (1957), pp. 199–208. DOI: 10.1016/0022-3697(57)90083-5 (cit. on p. 12).
- [26] K. Marken. «1 - Fundamental issues in high temperature superconductor (HTS) materials science and engineering». In: *High Temperature Superconductors (HTS) for Energy Applications*. Ed. by Ziad Melhem. Woodhead Publishing Series in Energy. Woodhead Publishing, 2012, pp. 1–31. ISBN: 978-0-85709-012-6. DOI: <https://doi.org/10.1533/9780857095299.1.3> (cit. on p. 12).
- [27] Masatoshi Sato and Yoichi Ando. «Topological superconductors: a review». In: *Reports on Progress in Physics* 80.7 (2017), p. 076501 (cit. on pp. 13, 17).
- [28] Manasi Mandal, Nathan C. Drucker, Phum Siriviboon, Thanh Nguyen, Artittaya Boonkird, Tej Nath Lamichhane, Ryotaro Okabe, Abhijatmedhi Chotrattanapituk, and Mingda Li. «Topological Superconductors from a Materials Perspective». In: *Chemistry of Materials* 35.16 (2023), pp. 6184–6200. DOI: 10.1021/acs.chemmater.3c00713 (cit. on p. 14).

- [29] B. Andrei Bernevig, Taylor L. Hughes, and Shou-Cheng Zhang. «Quantum Spin Hall Effect and Topological Phase Transition in HgTe Quantum Wells». In: *Science* 314.5806 (2006), pp. 1757–1761. DOI: 10.1126/science.1133734 (cit. on p. 14).
- [30] Markus König, Steffen Wiedmann, Christoph Brüne, Andreas Roth, Hartmut Buhmann, Laurens W. Molenkamp, Xiao-Liang Qi, and Shou-Cheng Zhang. «Quantum Spin Hall Insulator State in HgTe Quantum Wells». In: *Science* 318.5851 (2007), pp. 766–770. DOI: 10.1126/science.1148047 (cit. on p. 14).
- [31] Cui-Zu Chang and Mingda Li. «Quantum anomalous Hall effect in time-reversal-symmetry breaking topological insulators». In: *Journal of Physics: Condensed Matter* 28.12 (2016), p. 123002 (cit. on p. 14).
- [32] Cui-Zu Chang et al. «Experimental Observation of the Quantum Anomalous Hall Effect in a Magnetic Topological Insulator». In: *Science* 340.6129 (2013), pp. 167–170. DOI: 10.1126/science.1234414 (cit. on p. 14).
- [33] Qiong Ma et al. «Observation of the nonlinear Hall effect under time-reversal-symmetric conditions». In: *Nature* 565.7739 (2019), pp. 337–342 (cit. on p. 14).
- [34] Inti Sodemann and Liang Fu. «Quantum Nonlinear Hall Effect Induced by Berry Curvature Dipole in Time-Reversal Invariant Materials». In: *Phys. Rev. Lett.* 115 (21 Nov. 2015), p. 216806. DOI: 10.1103/PhysRevLett.115.216806 (cit. on p. 14).
- [35] Brian Skinner and Liang Fu. «Large, nonsaturating thermopower in a quantizing magnetic field». In: *Science Advances* 4.5 (2018), eaat2621. DOI: 10.1126/sciadv.aat2621 (cit. on p. 14).
- [36] Fei Han et al. «Quantized thermoelectric Hall effect induces giant power factor in a topological semimetal». In: *Nature communications* 11.1 (2020), p. 6167 (cit. on p. 14).
- [37] Huixia Luo, Peifeng Yu, Guowei Li, and Kai Yan. «Topological quantum materials for energy conversion and storage». In: *Nature Reviews Physics* 4.9 (2022), pp. 611–624 (cit. on p. 14).
- [38] Ettore Majorana. «Teoria simmetrica dell’elettrone e del positrone». In: *Il Nuovo Cimento (1924-1942)* 14.4 (1937), pp. 171–184 (cit. on p. 15).
- [39] Frank Wilczek. «Majorana returns». In: *Nature Physics* 5.9 (2009), pp. 614–618 (cit. on p. 16).
- [40] MM Sharma, Prince Sharma, NK Karn, and VPS Awana. «Comprehensive review on topological superconducting materials and interfaces». In: *Superconductor Science and Technology* 35.8 (2022), p. 083003 (cit. on p. 16).

- 
- [41] K. T. Law, Patrick A. Lee, and T. K. Ng. «Majorana Fermion Induced Resonant Andreev Reflection». In: *Phys. Rev. Lett.* 103 (23 Dec. 2009), p. 237001. DOI: 10.1103/PhysRevLett.103.237001 (cit. on p. 16).
- [42] Yukio Tanaka, Takehito Yokoyama, and Naoto Nagaosa. «Manipulation of the Majorana Fermion, Andreev Reflection, and Josephson Current on Topological Insulators». In: *Phys. Rev. Lett.* 103 (10 Sept. 2009), p. 107002. DOI: 10.1103/PhysRevLett.103.107002 (cit. on p. 16).
- [43] Karsten Flensberg. «Tunneling characteristics of a chain of Majorana bound states». In: *Phys. Rev. B* 82 (18 Nov. 2010), p. 180516. DOI: 10.1103/PhysRevB.82.180516. URL: <https://link.aps.org/doi/10.1103/PhysRevB.82.180516> (cit. on p. 16).
- [44] Goutam Sheet, S. Mukhopadhyay, and P. Raychaudhuri. «Role of critical current on the point-contact Andreev reflection spectra between a normal metal and a superconductor». In: *Phys. Rev. B* 69 (13 Apr. 2004), p. 134507. DOI: 10.1103/PhysRevB.69.134507 (cit. on p. 16).
- [45] Joel A. Appelbaum. «Exchange Model of Zero-Bias Tunneling Anomalies». In: *Phys. Rev.* 154 (3 Feb. 1967), pp. 633–643. DOI: 10.1103/PhysRev.154.633 (cit. on p. 16).
- [46] Carlo Beenakker and Leo Kouwenhoven. «A road to reality with topological superconductors». In: *Nature Physics* 12.7 (2016), pp. 618–621 (cit. on p. 17).
- [47] Liang Jiang, David Pekker, Jason Alicea, Gil Refael, Yuval Oreg, and Felix von Oppen. «Unconventional Josephson Signatures of Majorana Bound States». In: *Phys. Rev. Lett.* 107 (23 Nov. 2011), p. 236401. DOI: 10.1103/PhysRevLett.107.236401 (cit. on p. 17).
- [48] Katsuya Shimizu, Tomohiro Kimura, Shigeyuki Furomoto, Keiki Takeda, Kazuyoshi Kontani, Yoshichika Onuki, and Kiichi Amaya. «Superconductivity in the Non-magnetic State of Iron under Pressure». In: *Nature* 412 (Aug. 2001). DOI: 10.1038/35085536 (cit. on p. 17).
- [49] Hideo Hosono, Eiji Takayama-Muromachi Keiichi Tanabe, Shoji Yamanaka Hiroshi Kageyama, Hiroaki Kumakur, Hidenori Hiramatsu Minoru Nohara, and Satoru Fujitsu. «Exploration of new superconductors and functional materials, and fabrication of superconducting tapes and wires of iron pnictides». In: *Science and Technology of Advanced Materials* 16.3 (2015), p. 033503. DOI: 10.1088/1468-6996/16/3/033503 (cit. on pp. 18, 19).
- [50] Silvia Haindl. «Introduction to Fe-Based Superconductors». In: *Iron-Based Superconducting Thin Films*. Cham: Springer International Publishing, 2021, pp. 1–25. ISBN: 978-3-030-75132-6. DOI: 10.1007/978-3-030-75132-6\_1 (cit. on p. 19).

- [51] Lance M N Konzen and Athena S Sefat. «Lattice parameters guide superconductivity in iron-arsenides». In: *Journal of Physics: Condensed Matter* 29.8 (Jan. 2017), p. 083001. DOI: 10.1088/1361-648X/aa4e03 (cit. on pp. 19, 24).
- [52] Hideo Hosono, Akiyasu Yamamoto, Hidenori Hiramatsu, and Yanwei Ma. «Recent advances in iron-based superconductors toward applications». In: *Materials Today* 21.3 (Apr. 2018), pp. 278–302. ISSN: 1369-7021. DOI: 10.1016/j.mattod.2017.09.006 (cit. on p. 20).
- [53] Hideo Hosono and Kazuhiko Kuroki. «Iron-based superconductors: Current status of materials and pairing mechanism». In: *Physica C: Superconductivity and its Applications* 514 (2015). Superconducting Materials: Conventional, Unconventional and Undetermined, pp. 399–422. ISSN: 0921-4534. DOI: <https://doi.org/10.1016/j.physc.2015.02.020> (cit. on p. 20).
- [54] Charles Kittel. *Introduction to Solid State Physics*. 8th ed. Wiley, 2004. ISBN: 9780471415268 (cit. on p. 21).
- [55] Dario Daghero. «Experimental study of unconventional gap features in novel superconductors». PhD thesis. Politecnico di Torino, 2002 (cit. on pp. 21, 43, 47).
- [56] Junhua Zhang. «Theory of spin-fluctuation induced superconductivity in iron-based superconductors». MA thesis. Iowa State University Ames, Iowa, 2011 (cit. on p. 21).
- [57] H. Suhl, B. T. Matthias, and L. R. Walker. «Bardeen-Cooper-Schrieffer Theory of Superconductivity in the Case of Overlapping Bands». In: *Phys. Rev. Lett.* 3 (12 Dec. 1959), pp. 552–554. DOI: 10.1103/PhysRevLett.3.552 (cit. on pp. 22, 23).
- [58] M. D. Johannes and I. I. Mazin. «Fermi surface nesting and the origin of charge density waves in metals». In: *Phys. Rev. B* 77 (16 Apr. 2008), p. 165135. DOI: 10.1103/PhysRevB.77.165135 (cit. on p. 23).
- [59] Kamihara Y. et al. «Iron-Based Layered Superconductor: LaOFeP». In: *Journal of the American Chemical Society* 128 (31 Aug. 2006). DOI: 10.1021/ja063355c (cit. on p. 25).
- [60] Kamihara Y. et al. «Iron-Based Layered Superconductor: LaOFeP». In: *J. Am. Chem. Soc.* 130 (11 Mar. 2008). DOI: 10.1021/ja800073m (cit. on p. 25).
- [61] Hai-Hu Wen and Shiliang Li. «Materials and Novel Superconductivity in Iron Pnictide Superconductors». In: *Annual Review of Condensed Matter Physics* 2. Volume 2, 2011 (2011), pp. 121–140. ISSN: 1947-5462. DOI: <https://doi.org/10.1146/annurev-conmatphys-062910-140518> (cit. on p. 25).

- [62] Eric Thewalt et al. «Imaging Anomalous Nematic Order and Strain in Optimally Doped  $\text{BaFe}_2(\text{As}, \text{P})_2$ ». In: *Phys. Rev. Lett.* 121 (2 July 2018), p. 027001. DOI: 10.1103/PhysRevLett.121.027001 (cit. on p. 25).
- [63] T. Shibauchi, A. Carrington, and Y. Matsuda. «A Quantum Critical Point Lying Beneath the Superconducting Dome in Iron Pnictides». In: *Annual Review of Condensed Matter Physics* 5. Volume 5, 2014 (2014), pp. 113–135. ISSN: 1947-5462. DOI: <https://doi.org/10.1146/annurev-conmatphys-031113-133921> (cit. on p. 25).
- [64] I. Mazin. «Superconductivity gets an iron boost». In: *Nature* 464 (Mar. 2010), pp. 183–6. DOI: 10.1038/nature08914 (cit. on p. 25).
- [65] P J Hirschfeld, M M Korshunov, and I I Mazin. «Gap symmetry and structure of Fe-based superconductors». In: *Reports on Progress in Physics* 74.12 (Oct. 2011), p. 124508. DOI: 10.1088/0034-4885/74/12/124508 (cit. on p. 25).
- [66] Andrey Chubukov. «Pairing Mechanism in Fe-Based Superconductors». In: *Annual Review of Condensed Matter Physics* 3. Volume 3, 2012 (2012), pp. 57–92. ISSN: 1947-5462. DOI: <https://doi.org/10.1146/annurev-conmatphys-020911-125055> (cit. on p. 25).
- [67] Francesca Breccia. «Studio sperimentale del gap di energia in superconduttori non convenzionali a base di ferro». MA thesis. Politecnico di Torino, Torino, 2024 (cit. on p. 26).
- [68] Fong-Chi Hsu et al. «Superconductivity in the PbO-type structure -FeSe». In: *Proceedings of the National Academy of Sciences* 105.38 (2008), pp. 14262–14264. DOI: 10.1073/pnas.0807325105 (cit. on pp. 26, 27).
- [69] S Medvedev et al. «Superconductivity at 36 K in beta-Fe<sub>1-x</sub>Se with the compression of the interlayer separation under pressure». In: *arXiv preprint arXiv:0903.2143* (2009) (cit. on p. 27).
- [70] Qing-Yan Wang et al. «Interface-induced high-temperature superconductivity in single unit-cell FeSe films on SrTiO<sub>3</sub>». In: *Chinese Physics Letters* 29.3 (2012), p. 037402. DOI: 10.1088/0256-307X/29/3/037402 (cit. on p. 26).
- [71] Pascal Reiss, Matthew D Watson, Timur K Kim, Amir A Haghighirad, DN Woodruff, Mara Bruma, SJ Clarke, and Amalia I Coldea. «Suppression of electronic correlations by chemical pressure from FeSe to FeS». In: *Physical Review B* 96.12 (2017), p. 121103 (cit. on p. 26).
- [72] P. Wiecki, K. Rana, A. E. Böhmer, Y. Lee, S. L. Bud'ko, P. C. Canfield, and Y. Furukawa. «Persistent correlation between superconductivity and antiferromagnetic fluctuations near a nematic quantum critical point in  $\text{FeSe}_{1-x}\text{S}_x$ ». In: *Phys. Rev. B* 98 (2 July 2018), p. 020507. DOI: 10.1103/PhysRevB.98.020507 (cit. on p. 26).

- [73] Yuki Sato et al. «Abrupt change of the superconducting gap structure at the nematic critical point in FeSeS». In: *Proceedings of the National Academy of Sciences* 115.6 (2018), pp. 1227–1231. DOI: 10.1073/pnas.1717331115 (cit. on p. 26).
- [74] K. Nakayama, Y. Miyata, G. N. Phan, T. Sato, Y. Tanabe, T. Urata, K. Tanigaki, and T. Takahashi. «Reconstruction of Band Structure Induced by Electronic Nematicity in an FeSe Superconductor». In: *Phys. Rev. Lett.* 113 (23 Dec. 2014), p. 237001. DOI: 10.1103/PhysRevLett.113.237001 (cit. on p. 28).
- [75] J. Maletz et al. «Unusual band renormalization in the simplest iron-based superconductor FeSe<sub>1-x</sub>». In: *Phys. Rev. B* 89 (22 June 2014), p. 220506. DOI: 10.1103/PhysRevB.89.220506 (cit. on p. 28).
- [76] T. Shimojima et al. «Lifting of xz/yz orbital degeneracy at the structural transition in detwinned FeSe». In: *Phys. Rev. B* 90 (12 Sept. 2014), p. 121111. DOI: 10.1103/PhysRevB.90.121111 (cit. on p. 28).
- [77] Taichi Terashima et al. «Anomalous Fermi surface in FeSe seen by Shubnikov-de Haas oscillation measurements». In: *Phys. Rev. B* 90 (14 Oct. 2014), p. 144517. DOI: 10.1103/PhysRevB.90.144517 (cit. on p. 28).
- [78] Alain Audouard, Fabienne Duc, Loic Drigo, Pierre Toulemonde, Sandra Karlsson, Pierre Strobel, and André Sulpice. «Quantum oscillations and upper critical magnetic field of the iron-based superconductor FeSe». In: *Europhysics Letters* 109.2 (2015), p. 27003 (cit. on p. 28).
- [79] Shigeru Kasahara et al. «Field-induced superconducting phase of FeSe in the BCS-BEC cross-over». In: *Proceedings of the National Academy of Sciences* 111.46 (2014), pp. 16309–16313 (cit. on p. 28).
- [80] Alaska Subedi, Lijun Zhang, D. J. Singh, and M. H. Du. «Density functional study of FeS, FeSe, and FeTe: Electronic structure, magnetism, phonons, and superconductivity». In: *Phys. Rev. B* 78 (13 Oct. 2008), p. 134514. DOI: 10.1103/PhysRevB.78.134514 (cit. on p. 28).
- [81] G. F. Chen, Z. G. Chen, J. Dong, W. Z. Hu, G. Li, X. D. Zhang, P. Zheng, J. L. Luo, and N. L. Wang. «Electronic properties of single-crystalline Fe<sub>1.05</sub>Te and Fe<sub>1.03</sub>Se<sub>0.30</sub>Te<sub>0.70</sub>». In: *Phys. Rev. B* 79 (14 Apr. 2009), p. 140509. DOI: 10.1103/PhysRevB.79.140509 (cit. on p. 28).
- [82] Chiheng Dong, Hangdong Wang, Zujuan Li, Jian Chen, H. Q. Yuan, and Minghu Fang. «Revised phase diagram for the FeTe<sub>1-x</sub>Se<sub>x</sub> system with fewer excess Fe atoms». In: *Phys. Rev. B* 84 (22 Dec. 2011), p. 224506. DOI: 10.1103/PhysRevB.84.224506 (cit. on p. 28).

- [83] Y. Han, W. Y. Li, L. X. Cao, X. Y. Wang, B. Xu, B. R. Zhao, Y. Q. Guo, and J. L. Yang. «Superconductivity in Iron Telluride Thin Films under Tensile Stress». In: *Phys. Rev. Lett.* 104 (1 Jan. 2010), p. 017003. DOI: 10.1103/PhysRevLett.104.017003 (cit. on p. 28).
- [84] Y. Xia, D. Qian, L. Wray, D. Hsieh, G. F. Chen, J. L. Luo, N. L. Wang, and M. Z. Hasan. «Fermi Surface Topology and Low-Lying Quasiparticle Dynamics of Parent  $\text{Fe}_{1+x}\text{Te/Se}$  Superconductor». In: *Phys. Rev. Lett.* 103 (3 July 2009), p. 037002. DOI: 10.1103/PhysRevLett.103.037002 (cit. on p. 29).
- [85] Y. Zhang et al. «Strong correlations and spin-density-wave phase induced by a massive spectral weight redistribution in  $\alpha\text{-Fe}_{1.06}\text{Te}$ ». In: *Phys. Rev. B* 82 (16 Oct. 2010), p. 165113. DOI: 10.1103/PhysRevB.82.165113 (cit. on p. 29).
- [86] Xu Liu et al. «Electronic structure and superconductivity of FeSe-related superconductors». In: *Journal of Physics: Condensed Matter* 27.18 (). ISSN: 1361-648X. DOI: 10.1088/0953-8984/27/18/183201 (cit. on p. 29).
- [87] Z. K. Liu et al. «Measurement of Coherent Polarons in the Strongly Coupled Antiferromagnetically Ordered Iron-Chalcogenide  $\text{Fe}_{1.02}\text{Te}$  using Angle-Resolved Photoemission Spectroscopy». In: *Phys. Rev. Lett.* 110 (3 Jan. 2013), p. 037003. DOI: 10.1103/PhysRevLett.110.037003 (cit. on p. 29).
- [88] Dongfei Wang et al. «Evidence for Majorana bound states in an iron-based superconductor». In: *Science* 362.6412 (Oct. 2018), pp. 333–335. ISSN: 1095-9203. DOI: 10.1126/science.aao1797 (cit. on pp. 30, 67).
- [89] Peng Zhang et al. «Observation of topological superconductivity on the surface of an iron-based superconductor». In: *Science* 360.6385 (Apr. 2018), pp. 182–186. ISSN: 1095-9203. DOI: 10.1126/science.aan4596 (cit. on pp. 30, 34, 35).
- [90] Geng Li, Shiyu Zhu, Dongfei Wang, Yeliang Wang, and Hong-Jun Gao. «Recent progress of scanning tunneling microscopy/spectroscopy study of Majorana bound states in the  $\text{FeTeSe}$  superconductor». In: *Superconductor Science and Technology* 34.7 (2021), p. 073001 (cit. on pp. 30, 67).
- [91] Lijun Zhang, D. J. Singh, and M. H. Du. «Density functional study of excess Fe in  $\text{Fe}_{1+x}\text{Te}$ : Magnetism and doping». In: *Phys. Rev. B* 79 (1 Jan. 2009), p. 012506. DOI: 10.1103/PhysRevB.79.012506 (cit. on p. 30).
- [92] Alistair R Lennie, Simon AT Redfern, Paul F Schofield, and David J Vaughan. «Synthesis and Rietveld crystal structure refinement of mackinawite, tetragonal  $\text{FeS}$ ». In: *Mineralogical Magazine* 59.397 (1995), pp. 677–683 (cit. on p. 30).

- [93] Chetan Nayak, Steven H. Simon, Ady Stern, Michael Freedman, and Sankar Das Sarma. «Non-Abelian anyons and topological quantum computation». In: *Rev. Mod. Phys.* 80 (3 Sept. 2008), pp. 1083–1159. DOI: 10.1103/RevModPhys.80.1083 (cit. on p. 33).
- [94] Shiyu et al. Zhu. «Nearly quantized conductance plateau of vortex zero mode in an iron-based superconductor». In: *Science* 367.6474 (Jan. 2020), pp. 189–192. ISSN: 1095-9203. DOI: 10.1126/science.aax0274 (cit. on p. 34).
- [95] G. A. Ummarino, M. Tortello, D. Daghero, and R. S. Gonnelli. «Three-band s+- Eliashberg theory and the superconducting gaps of iron pnictides». In: *Physical Review B* 80.17 (2009). ISSN: 1550-235X. DOI: 10.1103/physrevb.80.172503 (cit. on pp. 36, 38).
- [96] Zi-Jian Yao, Jian-Xin Li, and ZD Wang. «Spin fluctuations, interband coupling and unconventional pairing in iron-based superconductors». In: *New Journal of Physics* 11.2 (2009), p. 025009 (cit. on p. 36).
- [97] Mark D Lumsden and Andrew D Christianson. «Magnetism in Fe-based superconductors». In: *Journal of Physics: Condensed Matter* 22.20 (2010), p. 203203 (cit. on p. 36).
- [98] Mauro Tortello, Dario Daghero, et al. «The Superconducting Order Parameter in High-Tc Superconductors—A Point-Contact Spectroscopy Viewpoint». In: *SUPERCONDUCTORS—NEW DEVELOPMENTS* (2015), p. 149 (cit. on p. 36).
- [99] B. Muschler, W. Prestel, R. Hackl, T. P. Devereaux, J. G. Analytis, Jiun-Haw Chu, and I. R. Fisher. «Band- and momentum-dependent electron dynamics in superconducting  $\text{Ba}(\text{Fe}_{1-x}\text{Co}_x)_2\text{As}_2$  as seen via electronic Raman scattering». In: *Phys. Rev. B* 80 (18 Nov. 2009), p. 180510. DOI: 10.1103/PhysRevB.80.180510 (cit. on p. 36).
- [100] T. E. Feuchtwang and E.L. Wolf. «Principles of electron tunneling spectroscopy». In: *Materials Research Bulletin* 21 (1986), p. 503 (cit. on p. 36).
- [101] M. Tortello, D. Daghero, G. A. Ummarino, V. A. Stepanov, J. Jiang, J. D. Weiss, E. E. Hellstrom, and R. S. Gonnelli. «Multigap Superconductivity and Strong Electron-Boson Coupling in Fe-Based Superconductors: A Point-Contact Andreev-Reflection Study of  $\text{Ba}(\text{Fe}_{1-x}\text{Co}_x)_2\text{As}_2$  Single Crystals». In: *Phys. Rev. Lett.* 105 (23 Dec. 2010), p. 237002. DOI: 10.1103/PhysRevLett.105.237002 (cit. on pp. 36, 37).
- [102] Lilia Boeri, Matteo Calandra, Igor I Mazin, Oleg V Dolgov, and Francesco Mauri. «Effects of magnetism and doping on the electron-phonon coupling in  $\text{BaFe}_2\text{As}_2$ ». In: *Physical Review B—Condensed Matter and Materials Physics* 82.2 (2010), p. 020506 (cit. on p. 37).

- [103] Junhua Zhang, Rastko Sknepnek, Rafael M Fernandes, and Jörg Schmalian. «Orbital coupling and superconductivity in the iron pnictides». In: *Physical Review B—Condensed Matter and Materials Physics* 79.22 (2009), p. 220502 (cit. on p. 37).
- [104] Paola Pecchio. «Experimental study of iron-based superconductors: advanced characterization and fundamental properties.» PhD thesis. politecnico di Torino, 2015 (cit. on p. 37).
- [105] Dario Daghero and RS Gonnelli. «Probing multiband superconductivity by point-contact spectroscopy». In: *Superconductor Science and Technology* 23.4 (2010), p. 043001 (cit. on pp. 39–47, 49–52, 54–57).
- [106] Branislav Nikolić and Philip B Allen. «Electron transport through a circular constriction». In: *Physical Review B* 60.6 (1999), p. 3963 (cit. on p. 41).
- [107] Aloysius Gerardus Maria Jansen, AP Van Gelder, and P Wyder. «Point-contact spectroscopy in metals». In: *Journal of Physics C: Solid State Physics* 13.33 (1980), p. 6073 (cit. on p. 42).
- [108] G Deutscher and R Maynard. «From the Andreev reflection to the Sharvin contact conductance». In: *The Gap Symmetry and Fluctuations in High-Tc Superconductors*. Springer, 2002, pp. 503–510 (cit. on p. 43).
- [109] GE Blonder, m M Tinkham, and TM Klapwijk. «Transition from metallic to tunneling regimes in superconducting microconstrictions: Excess current, charge imbalance, and supercurrent conversion». In: *Physical Review B* 25.7 (1982), p. 4515 (cit. on p. 48).
- [110] Satoshi Kashiwaya, Yukio Tanaka, Masao Koyanagi, and Koji Kajimura. «Theory for tunneling spectroscopy of anisotropic superconductors». In: *Physical Review B* 53.5 (1996), p. 2667 (cit. on pp. 52, 53).
- [111] Erik Piatti. «Ionic gating in metallic superconductors: A brief review». In: *Nano Express* 2.2 (2021), p. 024003 (cit. on p. 58).
- [112] I Strzalkowski. «The Physics of Semiconductors with Applications to Optoelectronics Devices». In: *European Journal of Physics* 20.5 (1999), pp. 351–352 (cit. on pp. 58, 59).
- [113] E. Piatti et al. «Control of bulk superconductivity in a BCS superconductor by surface charge doping via electrochemical gating». In: *Phys. Rev. B* 95 (14 Apr. 2017), p. 140501. DOI: 10.1103/PhysRevB.95.140501 (cit. on p. 58).
- [114] Kazunori Ueno, Hidekazu Shimotani, Hongtao Yuan, Jianting Ye, Masashi Kawasaki, and Yoshihiro Iwasa. «Field-induced superconductivity in electric double layer transistors». In: *Journal of the Physical Society of Japan* 83.3 (2014), p. 032001 (cit. on pp. 59, 60).

- [115] D. Daghero, F. Paolucci, A. Sola, M. Tortello, G. A. Ummarino, M. Agosto, R. S. Gonnelli, Jijeesh R. Nair, and C. Gerbaldi. «Large Conductance Modulation of Gold Thin Films by Huge Charge Injection via Electrochemical Gating». In: *Phys. Rev. Lett.* 108 (6 Feb. 2012), p. 066807. DOI: 10.1103/PhysRevLett.108.066807 (cit. on p. 60).
- [116] K Ueno, S Nakamura, H Shimotani, A Ohtomo, N Kimura, T Nojima, H Aoki, Y Iwasa, and M Kawasaki. «Electric-field-induced superconductivity in an insulator». In: *Nature materials* 7.11 (2008), pp. 855–858 (cit. on p. 60).
- [117] Rüdiger Kötz and MJEAC Carlen. «Principles and applications of electrochemical capacitors». In: *Electrochimica acta* 45.15-16 (2000), pp. 2483–2498 (cit. on p. 60).
- [118] JT Ye, S Inoue, K Kobayashi, Y Kasahara, HT Yuan, H Shimotani, and Y Iwasa. «Liquid-gated interface superconductivity on an atomically flat film». In: *Nature materials* 9.2 (2010), pp. 125–128 (cit. on p. 61).
- [119] Michael Freemantle. *An introduction to ionic liquids*. Royal Society of chemistry, 2010 (cit. on p. 60).
- [120] Takuya Fujimoto and Kunio Awaga. «Electric-double-layer field-effect transistors with ionic liquids». In: *Physical Chemistry Chemical Physics* 15.23 (2013), pp. 8983–9006 (cit. on pp. 60, 61).
- [121] Zengji Yue. «Ionic gating for ion intercalation». In: *Nature Reviews Physics* 3.5 (2021), pp. 306–306 (cit. on p. 62).
- [122] Nianpeng Lu et al. «Electric-field control of tri-state phase transformation with a selective dual-ion switch». In: *Nature* 546.7656 (2017), pp. 124–128 (cit. on pp. 62, 63).
- [123] Zengji Yue. «Ionic gating for ion intercalation». In: *Nature Reviews Physics* 3.5 (2021), pp. 306–306 (cit. on p. 63).
- [124] Yi Cui et al. «Protonation induced high-T<sub>c</sub> phases in iron-based superconductors evidenced by NMR and magnetization measurements». In: *Science Bulletin* 63.1 (2018), pp. 11–16 (cit. on pp. 64, 66).
- [125] Yan Meng, Wei Wei, Xiangzhuo Xing, Xiaolei Yi, Nan Zhou, Yufeng Zhang, Wenhui Liu, Yue Sun, and Zhixiang Shi. «Significant enhancement of critical current density in H<sup>+</sup>-intercalated FeSe single crystal». In: *Superconductor Science and Technology* 35.7 (2022), p. 075012 (cit. on pp. 64–66).
- [126] Yan Meng et al. «Protonation-induced discrete superconducting phases in bulk FeSe single crystals». In: *Physical Review B* 105.13 (2022), p. 134506 (cit. on pp. 64–66).

- [127] MZ Shi, NZ Wang, B Lei, C Shang, FB Meng, LK Ma, FX Zhang, DZ Kuang, and XH Chen. «Organic-ion-intercalated FeSe-based superconductors». In: *Physical Review Materials* 2.7 (2018), p. 074801 (cit. on p. 65).
- [128] MZ Shi et al. «FeSe-based superconductors with a superconducting transition temperature of 50 K». In: *New Journal of Physics* 20.12 (2018), p. 123007 (cit. on p. 65).
- [129] Jinhua Wang, Qing Li, Wei Xie, Guanyu Chen, Xiyu Zhu, and Hai-Hu Wen. «Superconductivity at 44.4 K achieved by intercalating EMIM+ into FeSe». In: *Chinese Physics B* 30.10 (2021), p. 107402 (cit. on p. 66).
- [130] Tadashige Nishikawa and Shunichi Fujimura. «"Beamex ER", new cross-linked polymeric insulated heat-and flame-resistant wires». In: *FAPIG (Tokyo);(Japan)* 89 (1978) (cit. on p. 70).
- [131] Gaia Gavello et al. «Facile synthesis of palladium hydride via ionic gate-driven protonation using a deep eutectic solvent». In: *Journal of Molecular Liquids* 420 (2025), p. 126826 (cit. on p. 72).
- [132] Gonnelli R.S. *Lecture notes in Advanced Experimental Physics*. Mar. 2022 (cit. on p. 78).
- [133] MH Fang, HM Pham, B Qian, TJ Liu, EK Vehstedt, Y Liu, L Spinu, and ZQ Mao. «Superconductivity close to magnetic instability in Fe (Se 1- x Te x) 0.82». In: *Physical Review B—Condensed Matter and Materials Physics* 78.22 (2008), p. 224503 (cit. on p. 87).